

Design and Development of Confocal Microscopic Techniques and Studies on Passive Permeability of Nuclear Membranes

THESIS

Submitted in partial fulfillment
of the requirements for the degree of
DOCTOR OF PHILOSOPHY

by

ARUNKARTHICK S

Under the Supervision of
Prof. P. Nandakumar

and

Co-supervision of
Prof. Meenal Kowshik



BITS Pilani
Pilani | Dubai | Goa | Hyderabad

BIRLA INSTITUTE OF TECHNOLOGY AND SCIENCE, PILANI

2015

BIRLA INSTITUTE OF TECHNOLOGY AND SCIENCE, PILANI

CERTIFICATE

This is to certify that the thesis entitled "Design and Development of Confocal Microscopic Techniques and Studies on Passive Permeability of Nuclear Membranes" and submitted by Arunkarthick S ID No. 2010PHXF024G for award of Ph.D. of the institute embodies original work done by him under our supervision.

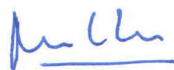


Signature of the Supervisor:

Name in capital block letters: **Prof. P. NANDAKUMAR**

Designation: Associate Professor

Date: 15/05/15



Signature of the Co-supervisor:

Name in capital block letters: **Prof. MEENAL KOWSHIK**

Designation: Associate Professor

Date: 15/05/15

DECLARATION

I **Arunkarthick S** hereby declare that this thesis entitled “**Design and Development of Confocal Microscopic Techniques and Studies on Passive Permeability of Nuclear Membranes**” submitted by me under the guidance and supervision of **Prof. P. Nandakumar** and **Prof. Meenal Kowshik** is a bonafide research work. I also declare that it has not been submitted previously in part or in full to this University or any other University or Institution for the award of any degree.

Signature of the Student: S. Arunkarthick ..

Name: **ARUNKARTHICK S**

Reg. No.: **2010PHXF024G**

Date: 15/5/15

Dedicated to

My Parents
Mr. Samudram - Mrs. Valliammal

&

My Wife
Mrs. Jeyajothi

ACKNOWLEDGEMENTS

First of all, I would like to express my sincere gratitude towards my research advisor and mentor, **Prof. P. Nandakumar** for his persistence and thoughtful guidance for me to stand as an independent researcher. I am grateful to him not only for his able guidance but also for encouraging me throughout my work. His constructive comments and suggestions have played a key role in formulating my attitude and aptitude towards research. His great experimental skill and up-to-date knowledge on all aspects has been a real help to me.

I am equally thankful to my co-supervisor **Prof. Meenal Kowshik** for her valuable support and inspiration. She has always helped me with timely and fruitful discussions. The efforts taken by her in cell culture and preparation of biological samples used in this thesis are worth mention. Her professional approach to research is highly sought after.

I am also grateful to **Dr. Toby Joseph** and **Prof. Radhika Vathsan** for their service as my doctoral advisory committee members. I deeply thank both of them for their motivation and useful discussions.

Dr. Geetha K. Varier has always been there for me with her pleasant smile and constant encouragement. She has always been with me in my ups and downs, both in professional and personal front. I can remember, only with wonder, her remarkable patience and self-motivation. The fruitful discussions with her on various aspects of science, arts and language are a great asset to my knowledge. I also very much enjoyed the motherly affection from her, who always showed a keen interest in my research and personal activities.

The work presented here would not have been possible without the assistance of many people. Throughout my Ph.D. research career, my colleague **Mr. M. M. Bijeesh** helped a lot in alignment of optics for setting up microscopy. I thank him very much for being with me.

I also express my gratitude towards (late) **Prof. Suresh Ramaswamy** (Former Dean) and (late) **Prof. Sanjeev K. Agarwal** (Former Director) whose motivation and memory directed me in my research work.

I would like to express gratitude towards my funding agencies **Department of Biotechnology** (Project Ref No. BT/PR11237/MED/32/66/2008), **Council of Scientific and Industrial Research**, (SRF Sanction No. 09/919(0018)/2013EmRI) Government of India and **Birla Institute of Technology and Science** for their support.

My special thanks to **Prof. B. N. Jain**, Vice-Chancellor, BITS Pilani, **Prof. Sasikumar Punnekkat**, Director, **Prof. Ashwin Srinivasan**, Deputy Director, **Prof. K. E. Raman**, Former Director, **Prof. S. K. Verma**, Dean, ARD, **Prof. Prasanta Kumar Das**, Associate Dean, ARD, **Prof. Sunil Bhand**, Dean, SRCD, **Prof. S. D. Manjare**, Former Faculty In-charge, RCEDD and **Prof. D. M. Kulkarni**, Dean, Administration BITS, Pilani - K K Birla Goa Campus, for providing the necessary facilities and environment to conduct my research work at this beautiful campus.

The effort taken by all the Faculty members of Department is also equally important in retaining my enthusiasm and attitude towards research. Departmental Research Committee (DRC) is also appreciated for keeping a timely check of the progress of my research work. My special thanks to **Prof. Gaurav Dar**, Head of the Department, **Dr. T. K. Jha**, DRC Convenor and other DRC members. I am particularly thankful to **Dr. E. S. Kannan** for being a good friend rather than a faculty at a distance. I deeply express my gratitude to him for his motivation and useful discussions. Timely advice and help from **Dr. Ram Shankar Patel** and **Dr. Teny John** is worth mention. I would like to extend my gratitude to **Prof. Utpal Roy**, **Dr. Anasuya Ganguly** and **Dr. Angsuman Sarkar** for their technical suggestions and help in cell culture related work. I thank **Prof. Sutapa Roy Ramanan** and **Prof. N. N. Ghosh** for extending their lab facilities.

I am deeply thankful to the research scholars especially **Mr. A. Venkatesan**, **Mr. J. Selvaganapathy**, **Mrs. Dhavala Suri**, **Ms. R. Aswini** and lab staffs **Ms. Meenakshi** and **Mr. Arun** for their constant support. I thank the faculties **Mr. CBK Moorthy**, **Mr. Surendran**, **Dr. Amalin Prince**, **Mr. Ramkumar** and **Dr. Jegatha** for their motivations and suggestions.

Throughout my research career, my colleagues **Dr. C. Siva Raman**, **Dr. R. Prasath**, **Dr. Bhanudas**, **Dr. Vilas**, **Dr. Amit Rajput** and **Dr. Zubeda**, helped me a lot in understanding the various aspects of instruments as well as handling the instruments. I always enjoyed the brother/sister cum friend relationship with them. I also enjoyed the wonderful moments with my juniors **Mr. Jayakumar**, **Mr. Gnana Bharathi** and **Mr. Sriram**. The fruitful discussions with my friends **Mr. S. A. Anton Kumanan** and **Mr. T. Arun** helped me a lot in understanding the various aspects of research in science and technology. I also thank my M.Tech. Biotechnology classmates **Dr. Karpanai Selvan**, **Mr. C. Arun**, **Dr. S. Senthil Kumar**, **Dr. Sobana Priya** and **Mr. B. Senthil Kumar** who helped me in various situations to get cells, biological samples and in analysis and characterization techniques.

I am lucky to have a group of juniors at BITS who are of high caliber and have a great sense of humor. I thank all my juniors **Mrs. Shakhi, Ms. Chithira, Ms. Akhila, Mrs. Malati, Mr. Mihir, Ms. Debashree, Mr. Tuhin** and **Mr. Atanu** for all the love that they showed towards me. The help rendered by **Ms. Ramya, Ms. Kshipra, Ms. Archana, Ms. Bhakti, Mr. Kabilan, Dr. Gowdaman, Ms. Shruthi, Ms. Nupur, Ms. Ketaki, Mrs. Jigini** and **Ms. Geethanjali** is incomparable, especially during preparing biomolecules and the cell culture studies, which played a key role in my research. The help rendered by BE students **Mr. Aravind, Mr. Nishith, Mr. Anand, Mr. Albert** and **Mr. Sobhit** in the development of imaging software using MATLAB and LabVIEW played an integral part in completing my thesis. I am grateful for various B.E., M.E. and M.Sc. batches that I have encountered during my research career, for all their love and support. I also thank the technicians **Mrs. Princy, Mr. Digambar, Mrs. Kamna** and **Mr. Mahadeo** for their help and co-operation.

I also enjoyed the wonderful moments in Goa with **Mr. Balasubramaniam** and family for their helpful discussions and for providing me a friendly environment during my stay in Goa with my family. I thank them for their good character and kindness.

I would like to express my sincere gratitude to my loving parents **Mr. Samudram** and **Mrs. Valliammal** and dearest brothers **Dr. S. Raja** and **Mr. S. Ramesh**, the greatest gift that god has given me on this earth, for their constant support, encouragement and prayers. I also wish to thank my in-laws **Mr. Chithiraikani, Mrs. Mariammal, Mr. Sivaraman** and **Dr. Jeyanthi** for their help and co-operation throughout my research work. I am sure that I would not have been able to achieve anything without their support, help and prayers.

Last but not the least; it is beyond words to express my gratitude to my wife **Mrs. Jeyajothi**, for all the care and love that she has shown towards me. Her appreciation and support even in my small achievements, has always been a source of motivation for me. I thank her for being with me in all crests and troughs of my life. The help and support, both intellectually and personally, given by her during the preparation of all my manuscripts and thesis is unique.

Above all, my gratitude towards the power that controls everything, without his blessings and mercy we cannot accomplish anything in this world. Thank **God**.

ARUNKARTHICK S
arunkarthick.biotech@gmail.com

TABLE OF CONTENTS

S. No.	TITLE	PAGE
	CERTIFICATE	ii
	DECLARATION	iii
	ACKNOWLEDGEMENTS	v
	TABLE OF CONTENTS	viii
	LIST OF FIGURES	xii
	LIST OF TABLES	xvi
	LIST OF SYMBOLS AND ABBREVIATIONS	xvii
	ABSTRACT	xxi
	CHAPTER 1: INTRODUCTION	1
1.1.	NUCLEAR TRANSPORT	2
1.1.1.	Nucleus	4
1.1.2.	Nuclear Envelope	5
1.1.3.	Nuclear Pore Complex	5
1.1.4.	Structure of Nuclear Pore Complex	6
1.1.5.	Active and Passive Modes of Nuclear Transport	8
1.1.6.	DNA Import into Nucleus	9
1.2.	OPTICAL MICROSCOPIC TECHNIQUES	10
1.2.1.	Confocal Microscopy	11
1.2.2.	Photothermal Microscopy	14
1.3.	OBJECTIVES	16
1.4.	OUTLAY OF THE THESIS	17
	CHAPTER 2: DESIGN AND CONSTRUCTION OF A CONFOCAL LASER SCANNING MICROSCOPE FOR BIOMOLECULAR IMAGING	18
2.1.	INTRODUCTION	18
2.2.	CONFOCAL FLUORESCENCE MICROSCOPY	19
2.3.	MATERIALS	20
2.3.1.	Details of Components Used in CLSM Construction	20
2.3.2.	Standard Microparticles and Biological Test Slides	22

2.4. EXPERIMENTAL METHODS	23
2.4.1. Confocal Laser Scanning Microscope Setup	23
2.4.2. Data Acquisition and Image Acquisition Software	25
2.4.3. Optical Alignment of the CLSM	28
2.4.4. Standardization of CLSM	29
2.4.5. Optical Sectioning Capability	30
2.5. RESULTS AND DISCUSSIONS	31
2.5.1. Resolution Test Targets	31
2.5.2. Standard Microparticles	32
2.5.3. Optical Sectioning Capability	34
2.5.4. Fluocell Test Slide	36
CHAPTER 3: TIME LAPSE CONFOCAL FLUORESCENCE IMAGING OF NUCLEAR TRANSPORT	38
3.1. INTRODUCTION	38
3.2. MATERIALS	39
3.2.1. Adherent Cell Lines	39
3.2.2. Cell Culture Materials	39
3.2.3. Reagents Used in Nuclear Transport Studies	42
3.2.4. Major Instruments Used	43
3.3. EXPERIMENTAL METHODS	44
3.3.1. Adherent Cell Line Culture	44
3.3.2. Cell Doubling Time Measurement	45
3.3.3. Imaging Chamber Preparation	45
3.3.4. Transport Buffer	46
3.3.5. FITC-Dextran Preparation	46
3.3.6. Digitonin Permeabilization	46
3.3.7. Dialysis of Rabbit Reticulocyte Lysate	47
3.3.8. Import Mixture Preparation	47
3.3.9. Nuclear Transport Studies	48
3.3.10. Confocal Imaging of Nuclear Transport	50
3.3.11. Model of Nuclear Transport Kinetics	51

3.3.12. Estimation of Rate of Nuclear Transport	53
3.4. RESULTS AND DISCUSSIONS	53
3.4.1. Cell Growth and Monitoring	53
3.4.2. Digitonin Permeabilization Optimization	56
3.4.3. Confocal Time Lapse Imaging	58
CHAPTER 4: PASSIVE PERMEABILITY AND EFFECTIVE PORE SIZE OF HELA CELL NUCLEAR MEMBRANES	60
4.1. INTRODUCTION	60
4.2. MATERIALS AND EXPERIMENTAL METHODS	62
4.3. RESULTS	63
4.4. DISCUSSIONS	72
CHAPTER 5: INFLUENCE OF RABBIT RETICULOCYTE LYSATE ON THE NUCLEAR TRANSPORT KINETICS OF DEXTRAN AND DNA	75
5.1. INTRODUCTION	75
5.2. MATERIALS	76
5.2.1. Materials Used in PCR Reaction	76
5.2.2. Reagents Used in DNA Preparation	78
5.3. EXPERIMENTAL METHODS	79
5.3.1. Preparation of DNA for Nuclear Transport Studies	79
5.3.2. PCR Reaction	80
5.3.3. Agarose Gel Analysis	81
5.3.4. Purification of DNA Fragments	81
5.3.5. Fluorescent Dye Labeling of DNA	82
5.3.6. Preparation of Cells for Nuclear Transport	82
5.4. RESULTS	82
5.4.1. RRL Dependence of Dextran Transport	82
5.4.2. PCR Products	88
5.4.3. DNA Transport through Nuclear Membranes	88
5.5. DISCUSSIONS	94

CHAPTER 6: FAST DETECTION AND IMAGING OF GOLD NANOPARTICLES USING LASER SCANNING PHOTOTHERMAL MICROSCOPY	98
6.1. INTRODUCTION	98
6.2. PHOTOTHERMAL IMAGING	99
6.3. MATERIALS	101
6.4. EXPERIMENTAL METHODS	103
6.4.1. Construction of Laser Scanning Photothermal Microscope	103
6.4.2. Sample Preparations for Imaging	105
6.4.3. Photothermal Imaging of Gold Nanoparticles in Live Cell	105
6.5. RESULTS AND DISCUSSION	106
6.5.1. Photothermal Imaging of 5 nm Gold Nanoparticles	106
6.5.2. Photothermal Image of 10 nm and 5 nm Gold Nanoparticles in Same Sample	108
6.5.3. Laser Power Dependence on Photothermal Signal	109
6.5.4. Modulation Frequency Dependence	109
6.5.5. Size Dependence of the Photothermal Signal	110
6.5.6. Potential in Live Cell Imaging	113
CHAPTER 7: SUMMARY AND CONCLUSIONS	120
REFERENCES	124
PUBLICATIONS AND PRESENTATIONS	137
BIODATA OF CANDIDATE	140
BIODATA OF SUPERVISOR	141
BIODATA OF CO-SUPERVISOR	142
GLOSSORY	143

LIST OF FIGURES

FIGURE	TITLE	PAGE
1.1.	Structure of Eukaryotic Cell Nucleus	4
1.2.	Structure of Nuclear Pore Complex	7
1.3.	Working Procedure and a Schematic Diagram of a Confocal Microscope	13
1.4.	Schematic Diagram of a Photothermal Microscope	15
2.1.	Experimental Setup of the Confocal Laser Scanning Microscope	24
2.2.	Contents of the Settings Tab in Front Panel of the LabVIEW Program	26
2.3.	Contents of the Output Tab in Front Panel of the LabVIEW Program	26
2.4.	500 × 500 Pixel Confocal Image of USAF 1951 Test Target	31
2.5.	Confocal Image of Polystyrene Beads Having a Mean Size of 100 nm and Lateral and Axial Line Intensity Profile of a Single 100 nm Polystyrene Bead	33
2.6.	Confocal Images of 100 nm Polystyrene Beads	34
2.7.	Optical Sections of the 5 μm Silica Gel Beads	35
2.8.	Cross Sectional Images of a Dye Labeled Pollen Grain Shows the Optical Sectioning Capability of CLSM and 3D Reconstructed Image	36
2.9.	Confocal Image of Actin Filaments in FluoCells Prepared Slide Contains Muntjac Skin Fibroblast Cells Stained with an Alexa Fluor 488 Phalloidin	37
3.1.	Flow Chart of Nuclear Transport Experiment Procedure	49
3.2.	Experimental Layout of the Confocal Laser Scanning Microscope Used in Time Lapse Imaging of Nuclear Transport	51

3.3.	Inverted Microscope Images of HeLa Cells Imaged using 10X and 60X Objective	54
3.4.	Inverted Microscope Images of A549 Cells Imaged using 10X, 20X and 60X Objective	55
3.5.	Confocal Images of A549 cells with 70 kDa FITC Labeled Dextran Molecules Added to Cells which are Permeabilized with Different Concentrations of Digitonin	57
3.6.	Time Lapse Confocal Images of A549 Cells after the Addition of 10 kDa FITC Labeled Dextran Molecules to Digitonin Permeabilized Cells	58
4.1.	Time Lapse Confocal Images of HeLa Cell Nucleus after the Addition of 4 kDa FITC Labeled Dextran Molecules	64
4.2.	Time Lapse Confocal Images of HeLa Cell Nucleus after the Addition of 10 kDa FITC Labeled Dextran Molecules	64
4.3.	Time Lapse Images of HeLa Cell Nucleus after the Addition of FITC Labeled Dextran Molecules of MW 20 kDa	65
4.4.	Time Lapse Images of HeLa Cell Nucleus after the Addition of FITC Labeled Dextran Molecules of MW 40 kDa	65
4.5.	Time Lapse Confocal Images of HeLa Cell Nucleus after the Addition of FITC Labeled Dextran Molecules of MW 70 kDa	66
4.6.	Image of the Cell Nucleus at 100 seconds after the Addition of Import Mixture Containing Different Sizes of Dextrans	66
4.7.	Percentage of Dextran Molecules Entered the Cell Nucleus after 100 seconds	67

4.8.	Nucleo-Cytoplasmic Flux and Nuclear Import Rate Constants of Dextrans Having Four Different Molecular Mass	68
4.9.	Estimation of Passive Pore Radius from Diffusion Rates	71
5.1.	Time Lapse Confocal Images of A549 Cell Nucleus after the Addition of FITC Labeled Dextran Molecules of MW 10 kDa with Four Different RRL Concentrations	84
5.2.	Time Lapse Confocal Images of A549 Cell Nucleus after the Addition of FITC Labeled Dextran Molecules of MW 20 kDa with Four Different RRL Concentrations	85
5.3.	Nucleo Cytoplasmic Flux of Dextran Molecules of 10 kDa and 20 kDa with Four Different Concentrations of RRL	86
5.4.	The Average Transport Rate Constant Values are shown with Spread of the Rates Gained with 10 kDa and 20 kDa Dextran Molecules	87
5.5.	Gel Documentation Image of Agarose Gel with PCR Products	88
5.6.	Confocal Time Lapse Images of A549 Cell Nucleus after the Addition of 113 bp and 304 bp of DNA with and without RRL	90
5.7.	Confocal Time Lapse Images of A549 Cell Nucleus after the Addition of 480 bp, 750 bp and 1000 bp of DNA with and without RRL	91
5.8.	Normalized Nuclear Fluorescence versus Time for the Transport of Different Sizes of DNA Fragments with the Presence and Absence of RRL	92

5.9.	Effect of DNA Size on Nuclear Accumulation in Cells with and without RRL for the Sizes of 113 bp, 310 bp, 480 bp and 750 bp	93
6.1.	Optical Layout of Laser Scanning Photothermal Microscope Setup	104
6.2.	Photothermal Image of 5 nm Gold Nanoparticles Coated on Glass Cover Slip and its Laser Power Dependence	107
6.3.	Photothermal Image of a Sample Containing Two Sizes of Gold Nanoparticles Having Average Diameters of 10 nm and 5 nm	108
6.4.	Dependence of Pump Modulation Frequency on SNR of the Photothermal Image	110
6.5.	Photothermal Image and its Intensity Distribution Histograms for Gold Nanoparticles Having Average Particle Sizes of 5 nm, 10 nm, 20 nm and 40 nm	111
6.6.	Log-Log Plot of Photothermal Signal Intensity vs. Particle Size	112
6.7.	Time Lapse Images of 5 nm Gold Nanoparticles in Live A549 Cells	114
6.9.	Time Lapse Images of 10 nm Gold Nanoparticles in Live A549 Cells	115
6.10.	Time Lapse Images of 20 nm Gold Nanoparticles in Live A549 Cells	116
6.11.	Twelve 2-D Sections of the Nucleus Taken Approximately 3 Hours after the Addition of Import Mixture Containing 5 nm Gold Nanoparticles	117
6.12.	Twelve 2-D Sections of the Nucleus Taken Approximately 4 Hours after the Addition of Import Mixture Containing 20 nm Gold Nanoparticles	118

LIST OF TABLES

TABLE	TITLE	PAGE
2.1.	Components Used in the Construction of CLSM along with Cost	27
4.1.	Rate Constants of Transport and Permeability Coefficients of HeLa Cell Nuclear Membrane for Dextran Molecules	69
4.2.	Equivalent Radius of the Diffusion Channel in the Nuclear Pore Complex	71
5.1.	PCR Primer Sequences and PCR Product Length	79
5.2.	Rate Constants for 10 kDa and 20 kDa FITC Labeled Dextrans Transport through Nuclear Membrane of A549 Cells with Different Concentrations of RRL	87
5.3.	Percentage Increase in Rate Constant of Transport of Different Sizes of DNA Fragments through A549 Cell Nuclear Membranes	93

LIST OF SYMBOLS AND ABBREVIATIONS

2D	-	Two Dimensional
3D	-	Three Dimensional
AFM	-	Atomic Force Microscopy
ATP	-	Adenosine Triphosphate
bp	-	Base Pair
BSA	-	Bovine Serum Albumin
CLSM	-	Confocal Laser Scanning Microscope
DMEM	-	Dulbecco's Modified Eagles Medium
DMSO	-	di-methyl Sulphoxide
DNA	-	Deoxy Ribonucleic Acid
dNTP	-	Deoxy Nucleotide Triphosphate
DOF	-	Depth of Field
DPC	-	Differential Phase Contrast
DTT	-	Dithiothreitol
EDTA	-	Ethylene Diamine Tetra Acetic acid
ER	-	Endoplasmic Reticulum
F	-	Phenylalanine
FBS	-	Fetal Bovine Serum
FG repeats	-	Phenylalanine-Glycine repeats
FITC	-	Fluorescein Isothiocyanate
FWHM	-	Full Width Half Maximum
GDP	-	Guanosine Diphosphate
GFP	-	Green Fluorescent Protein
GTP	-	Guanosine Triphosphate
h	-	Hour
H ₂ O	-	Water
H ₂ SO ₄	-	Sulphuric Acid
HCl	-	Hydrochloric Acid
HIV-1	-	Human Immunodeficiency Virus-1

kb	-	Kilobase
kDa	-	Kilo Dalton
LSPTM	-	Laser Scanning Photothermal Microscopy
M	-	Molarity
MDa	-	Mega Dalton
MgCl ₂	-	Magnesium Chloride
mL	-	milli Liter
mg	-	milligram
mg/L	-	milligram per Liter
mM	-	milli Molar
mm	-	millimeter
NA	-	Numerical Aperture
NaCl	-	Sodium Chloride
NE	-	Nuclear Envelope
NES	-	Nuclear Export Signal
NLS	-	Nuclear Localization Signal
nm	-	nanometer
NPC	-	Nuclear Pore Complex
NTR	-	Nuclear Transport Receptor
Nups	-	Nucleoporins
PBS	-	Phosphate Buffered Saline
PCR	-	Polymerase Chain Reaction
pDNA	-	Plasmid DNA
pH	-	Negative Logarithm of Hydrogen Ion Concentration
PSF	-	Point Spread Function
PT	-	Photothermal
PTM	-	Photothermal Microscopy
R	-	Optical Resolution
RNA	-	Ribonucleic Acid
rpm	-	Revolutions per Minute
s	-	Second

SD	-	Standard Deviation
SNR	-	Signal to Noise Ratio
SV-40	-	Simian Virus 40
TCHD	-	Trans-Cyclohexane-1,2-Diol
TRITC	-	Tetramethyl Rhodamine Isothiocyanate
UV	-	Ultraviolet
U/ μ L	-	Unit/microliter
v/v	-	Volume by Volume
WGA	-	Wheat Germ Agglutinin
w/v	-	Weight by Volume
xg	-	Times Gravity
Z	-	Optical Thickness
$^{\circ}$ C	-	Degree Celsius
μ L	-	micro Liter
μ m	-	micrometer
μ M	-	micro Molar
λ	-	Wavelength
η	-	Refractive Index of Medium
θ	-	Optical Scanning Angle
λ_{em}	-	Emission Wavelength
λ_{ex}	-	Excitation Wavelength

In this thesis I would like to use the term ‘We’ instead of ‘I’ because during a PhD thesis work one is usually supported by other persons, in particular the supervisors and lab members. However, the experiments described in this thesis and the writing were essentially done by myself.

ABSTRACT

Studies on biomolecular transport through nuclear membranes are of interest from a fundamental physics perspective as well as from the point of view of biological applications. The nuclear pore complexes (NPCs) in the nuclear membrane are the only known passage way for macromolecules to enter into and exit from the nucleus. The NPCs prevent any foreign DNA from entering the nucleus and regulate the transport of desired molecules in an organized and orderly fashion. Though it is well known that they play a central role in the regulation of cell functions, there is still no clear agreement on the structure and pore size of the NPCs. Moreover the mechanisms involved and the environment dependent role of the NPCs in the regulation of nuclear transport is not yet thoroughly probed. A proper understanding of the transport phenomena will help in developing methodologies which will be of interest to biomedical research, especially related to gene therapy.

Optical microscopic techniques play an important role in biomedical research. In this research work we first developed a confocal laser scanning microscope (CLSM) for studying biomolecular transport through nuclear membranes. Even though confocal fluorescence microscopes are commercially available, most of them are not flexible to be used in laboratory environment where different types of experiments are to be carried out. When compared to commercial microscopes, the CLSM designed in the laboratory is cost effective and versatile, and the same microscope can be used in different geometries such as photothermal microscopy and nonlinear microscopy. An inverted microscope, X-Y galvanometric mirror scanner, data acquisition card (DAQ), an Argon ion laser or HeNe laser and optics available in the laboratory are used in the construction of CLSM. Reflectance or fluorescence signal is coupled to a photo detector through an optical fiber which acts as the confocal aperture. For scanning, data acquisition and image reconstruction, we use a DAQ card and a home written LabVIEW program. Calibration of CLSM is done with a standard resolution test target and polystyrene microparticles of different known diameters. The microscope is successfully employed in time lapse imaging of the nucleus for monitoring the nuclear import of biomolecules.

Passive biomolecular transport through nuclear pore complexes is studied using the in-house constructed microscope so as to determine the permeability of the nuclear membrane. Studies are carried out in digitonin permeabilized cells using FITC labelled dextran molecules, a

model drug system for studying nuclear transport. Digitonin permeabilized cells have leaky plasma membranes but intact nuclei. Time lapse confocal imaging scheme is employed to quantify the nuclear import of dextrans. We specifically examined the kinetics of transport of dextrans of 4, 10, 20, 40 and 70 kDa through the nuclear membrane of live A549 and HeLa cells and determined the diffusion rate constants. When diffusion is the major process by which molecules are transported through the membranes, the permeability of the molecule depends on its size. Analyzing the permeability of the nuclear membrane for different sizes under transient conditions, we estimate the effective pore radius of HeLa cell nuclear membrane to be in the range of 4.9 – 5.7 nm.

The ability to send a desired molecule into the nucleus is a crucial first step in non-viral gene delivery and the success of gene therapy experiments will depend on strategies that can enhance the nuclear uptake of DNA. Normally the cell nucleus is not receptive to foreign DNA and the efficiency of such gene delivery is very poor. In this work we studied the kinetics of passive transport of DNA fragments having different number of base pairs through the nuclear membrane. Rate constant of nuclear transport is determined for the different fragments and it is found that DNA base pairs of up to 750 bp are able to diffuse passively into the nucleus.

Several factors can positively or negatively affect the efficiency of transport of DNA through the NPCs. In search for environmental factors that can positively influence nuclear transport, we looked at the effect of Rabbit Reticulocyte Lysate (RRL) on the nuclear uptake of dextran and DNA. We analyzed this effect on dextran uptake by determining the transport rate of dextran molecules having the same molecular weight using a transport mixture having RRL of varying concentrations. It is found that in digitonin permeabilized cells under transient condition, the rate of transport of biomolecules depends critically on the concentration of RRL. We were able to enhance the rate of nuclear transport of 10 kDa and 20 kDa dextran by a factor of 2 or more by changing the concentration of RRL in the import mixture. In order to find the effect of RRL on DNA transport we compared the size dependent nuclear internalization of fluorescently labeled DNA in the presence and absence of RRL. Results show that there is around 50% increase in transport rates in presence of RRL for 113 bp DNA. This study shows that the nuclear uptake of DNA can be increased by making use of appropriate transport agents in gene therapy related experiments.

One of the major challenges we faced in this study, which is common to all confocal fluorescence microscopy experiments that require long observation times, is the photobleaching of dye labels. Photo stable labels and alternative imaging techniques will help in improving the applicability of optical microscopy in different experimental situation. In this work we also report on the development of a laser scanning photothermal microscope that can detect and image single gold nanoparticle of size as small as 5 nm with microsecond integration times and long observation times without photobleaching. We present time lapse images on the nuclear uptake of gold nanoparticles in digitonin permeabilized cells and demonstrate the capability of the microscope in biological imaging. The laser scanning method developed here allows for fast image acquisition at 80 μ s pixel dwell time so that a 500×500 pixel image is acquired in 20 seconds. Photothermal imaging at fast time scales can have potential applications in variety of fields including tracking of biomolecular movement in a live cell.

CHAPTER ONE**INTRODUCTION**

The nuclear and cytoplasmic materials in eukaryotic cells are separated by a double layered membrane known as nuclear envelope. The nucleoplasm and genetic materials within the nucleus are protected by the nuclear membrane. It plays a vital role in the localization of gene activation and cell cycle regulation. The nuclear membrane is punctuated by holes, known as nuclear pore complexes (NPCs), which act as the sole gateway for the import of nuclear proteins into, and export of RNA and ribosomal sub-particles from the nucleus. NPCs allow passive diffusion of ions and small molecules, whereas RNA's, nuclear proteins and ribonucleoproteins larger than ~ 9 nm are selectively and actively transported by an energy-dependent and signal-mediated mechanism. Though it is well known that they play a central role in the regulation of cell functions, there is no clear agreement among researchers on the structure and size of the NPCs across different cells. Also the mechanisms involved and the environment dependent role of NPCs in regulation of nuclear transport is not still well understood. A proper understanding of the transport phenomena will help in developing methodologies which will be of interest to biomedical research, especially related to gene therapy.

Optical microscopic techniques play a vital role in the study of biological cells, membranes and tissues. Among different microscopic techniques available, confocal fluorescence microscopy is the most important and effective technique employed in the examination of the NPCs. The present thesis report on the development of a flexible and low cost confocal fluorescence microscope and describes the investigations carried out on the kinetics of biomolecular transport through the NPCs using this microscope. From the kinetic analysis of the passive nuclear transport of molecules of different Stokes radius we determine the permeability of the nuclear membrane and estimate the size of the nuclear pores. We also report on the development of a laser scanning photothermal microscope that is able to detect and image gold nanoparticles at fast time scales. Gold nanoparticles are highly photostable and biocompatible and could be used as labels in bioimaging.

In order to set a right perspective of the field, in this introductory chapter we briefly discuss nuclear transport phenomena and microscopic techniques employed to study them. Section 1 gives introduction about the nucleus, nuclear membrane, nuclear pore complex and literature on nuclear transport studies of different biomolecules. Section 2 explains about optical microscopic techniques used in our studies on biomolecular transport through nuclear membranes.

1.1. NUCLEAR TRANSPORT

The organization of eukaryotic cells includes different compartments. This compartmentalization provides additional facilities for regulation, but spatially restricts cellular processes. However, many processes, the fundamental process of gene expression (transcription in the nucleoplasm and translation in the cytoplasm) for instance require the exchange of macromolecules between compartments. This exchange of molecules between cytoplasm and nucleus are achieved through the NPCs. Nucleus and cytoplasm is connected through the NPCs that are embedded in the nuclear membrane. The NPCs allow passive diffusion of small molecules like ions but restricts the passage of macromolecules larger than 40 – 60 kDa which have to be actively transported.

In the early 1950s, Coons *et al.*, used fluorescent antibody technique to inject three external proteins into rats and determined the intracellular delivery of the injected proteins (Coons *et al.*, 1951). Their investigation resulted in an interesting finding. The injected proteins had entered the nuclei of different tissues. Most often they appeared in the nucleus in higher concentration than in the cytoplasm. Approximately at the same time, Holtfreter reported permeation of hemoglobin (molecular weight, MW ~ 64 kDa) into isolated amphibian oocyte nuclei suspended in a hemoglobin solution (Holtfreter, 1954). This experiment gave an indication that materials of a considerable MW could move into the nucleus. Thus, existence of channels between nucleus and cytoplasm is certain.

In 1962, Feldherr reported that polyvinyl pyrrolidone coated gold particles of diameter ≤ 10 nm can penetrate into the nuclear membrane (Feldherr, 1962). These particles are also reported to be found at greater concentration inside the nucleus than outside. The author

proposed that this movement takes place through specialized channels, named nuclear pores. The initial detailed observations regarding the structure of the nuclear pore complex are concerned with its physical size. These experiments utilized high resolution electron microscopy. Feldherr noted that nuclear pores measured about 64 nm in longitudinal section in *Amoeba proteus* (Feldherr, 1965). He afterward reported the nuclear pore complex of the multinucleated amoeba *Chaos chaos* to be approximately 61.5 nm (Feldherr, 1966). Another group noted that they are approximately 100 nm in bull cell nucleus (Wooding & O'Donnell, 1971). All this microscopic studies are carried out on fixed live cells.

NPCs received much more attention from researchers during the late 1970s and the 1980s due to advancement in technology which made sophisticated techniques available. The technical expertise in the field brought proteins in the NPCs into lime light in this era. The first list of nuclear pore complex proteins evolved, albeit at a modest pace. In the late 1980s, nuclear pore complex researchers began to decipher not only the structure, but also the mechanisms of transportation through the NPCs as well as the import and export factors involved in translocation (Steer *et al.*, 1980, Richardson & Maddy, 1980). Eventually the protein import mechanism of the NPC and the role of nuclear localization signals (NLS), which directs the proteins to the NPC became clear (Rout *et al.*, 2000, Bagley *et al.*, 2000, Kiseleva *et al.*, 2000). Also, studies of RNA and RNP export began to yield important evidences, though more slowly than protein import studies. However the details of the mechanism of transport of different types of biomolecules or how the NPCs accommodate such large numbers of translocation, still remain elusive. Regarding the structure of the NPCs, still there is no agreement among researchers, with two different models being discussed. Regarding the size of the NPCs channels, the reports still shows a large variation from about 5 nm to 10 nm.

Moreover, molecules with size higher than the diffusion limit often pass through the NPCs in the active mode because this allows highly efficient and regulated transport (Conti & Izaurralde, 2001, Fried & Kutay, 2003, Gorlich & Kutay, 1999). Soluble transport receptors often mediate the translocation processes. They specifically recognize transport signals within their cargo proteins and facilitate the passage through the NPCs. Active transport allows for accumulation of molecules against their concentration gradient and therefore requires the input of energy.

1.1.1. Nucleus

Nucleus acts as the most important store house of genetic information, the deoxyribonucleic acid (DNA). The nucleus is composed of the four important structures - nuclear membrane, nucleoplasm, chromatin network and nucleolus. Nucleoplasm is present inside the cell nucleus like a viscous liquid, similar to the cytoplasm found outside the nucleus. Nucleus contains most of the cells genetic materials organized as multiple long linear DNA molecules in complex with a range of proteins, such as histones, to form chromosomes. Genes inside these chromosomes are known as the cells nuclear genome. The function of the nucleus is to maintain the integrity of these genes and to direct the activities of the cell by regulating gene expression. DNA, ribonucleic acids and ribonucleo proteins are synthesized in the nucleus. These macromolecules are involving in directing transcriptional and translational activity, which in the end results in protein synthesis and cell proliferation (Spector, 1993, Spector *et al.*, 1993). A schematic of the structure of eukaryotic cell nucleus is shown in figure 1.1.

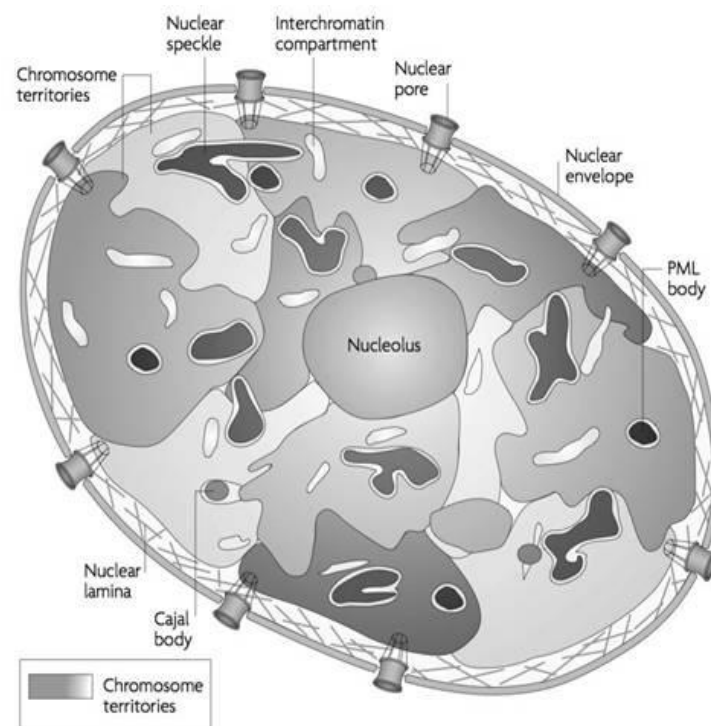


Figure 1.1: Structure of eukaryotic cell nucleus. The nucleus is composed of nuclear membrane, nucleoplasm, nucleolus and chromatin network (Image is obtained from <http://www.sivabio.50webs.com/nucleus.htm>).

1.1.2. Nuclear Envelope

The nucleus is surrounded by a double layered membrane which separates the nucleus from the cytoplasm. The nuclear membrane is a phospholipid bilayer, with its outside surface continuous with the endoplasmic reticulum and its internal surface facing the nucleus. The two layers in the nuclear membrane is separated by a perinuclear space which is about 15 – 30 nm. Each outer and inner layer is about 7 – 8 nm thick. The outer membrane is often continuous with membrane of the golgi complex, endoplasmic reticulum, mitochondria and plasma membrane. The outer membrane is rough due to the presence of ribosomes, while the inner membrane is smooth. The structure of the nuclear membrane is elucidated using transmission electron microscopy (Campbell, N. A. Biology, Third Edition 1993). The nuclear membrane has tiny pores which allow the transport of material between nucleus and cytoplasm. This is the only recognized passageway for macromolecules to enter into and exit from the nucleus. This interphase is an extremely complex macromolecular assembly of abundant protein subunits named as NPCs (Kleinsmith & Kish, 1995, Spector, 1993).

1.1.3. Nuclear Pore Complex

The nuclear pore complex (NPC) is the principal gateway between the nucleus and the cytoplasm. Although the evolutionary origin of the NPC is unknown and its dimension varies between different types of species, there is a great deal of homology among organisms. This homology allows comparisons between NPCs of different species, leading to better understanding of the structure.

The NPC is one of the most important components of the eukaryotic cell. Fault in the formation of nuclear pore complexes, leads to cellular death. The nuclear pore complex regulates the flow of macromolecules between the nucleus and the cytoplasm (Bastos *et al.*, 1995). Early NPC research was limited by insufficient technical capabilities and instrumentation. 1950 onwards instrumentation available was better and gave a leap to the findings, example: electron microscopy. However there is no clear agreement on how exactly the nuclear pore complexes are developed. Similarly, little is known about nuclear pore complex biogenesis. NPC assembly needs the involvement of many cytoplasmic and nuclear proteins. The NPCs are made up of protein subunits called nucleoporins (NUP). This proteins are normally found in cytoplasm in

dissociated stage and they gets associated with nuclear membrane during cell division (Bodoor *et al.*, 1999). The nucleoporins found in these NPCs included NUP58, NUP97, NUP60, NUP153 and NUP200. Sec13 protein in conjunction with NUP84 has been determined to be necessary for normal nuclear pore complex formation (Siniossoglou *et al.*, 1996, Chatel & Fahrenkrog, 2012, Xylourgidis & Fornerod, 2009). gp210, an important NPC protein, has been found to be rich in the cytoplasm of *Drosophila* early in embryogenesis (Berrios *et al.*, 1995). Failure of NPC development is catastrophic and will cause cellular death (Chatel & Fahrenkrog, 2012, Watters & Palmenberg, 2011, Xylourgidis & Fornerod, 2009).

The number of pores present in the nuclear envelope can vary between 2 – 4 pores/ μm^2 (mammalian lymphocytes) to over 60 pores/ μm^2 (mature *Xenopus* oocyte). This provides an estimation of 2000 – 4000 nuclear pore complexes per cell nucleus (Spector, 1993). Individual NPC is thought to have molecular weight of about 120 – 125 MDa in a variety of vertebrate cells (Pante & Aebi, 1996, Bastos *et al.*, 1995). In the past several years, our understanding about the NPC has considerably expanded because of extensive application of *in vitro* systems such as *Xenopus* oocytes and yeast genetic organisms (Simos & Hurt, 1995, Bastos *et al.*, 1995, Meinema *et al.*, 2012, Chatel & Fahrenkrog, 2012). As of today, relatively lesser number of NPC subunits has been found to perform both structural and functional roles. Genetic analysis and cross-species homology between highly conserved proteins in the NPCs supported dissection of nuclear pore complex proteins. This lead a step further towards understanding the structural and functional properties of NPCs. (Doye & Hurt, 1995, Mizuguchi-Hata *et al.*, 2013, Xylourgidis & Fornerod, 2009, Chatel & Fahrenkrog, 2012)

1.1.4. Structure of Nuclear Pore Complex

The reconstruction of the nuclear pore complex structure based on high-resolution electron microscopy data revealed the structural design of NPC. The NPC has eight fold symmetry to the membrane and is irregular to the membrane surface. In a simplified way, the NPC comprises of three substructures: (1) a central core, (2) the cytoplasmic filaments and (3) the nuclear basket.

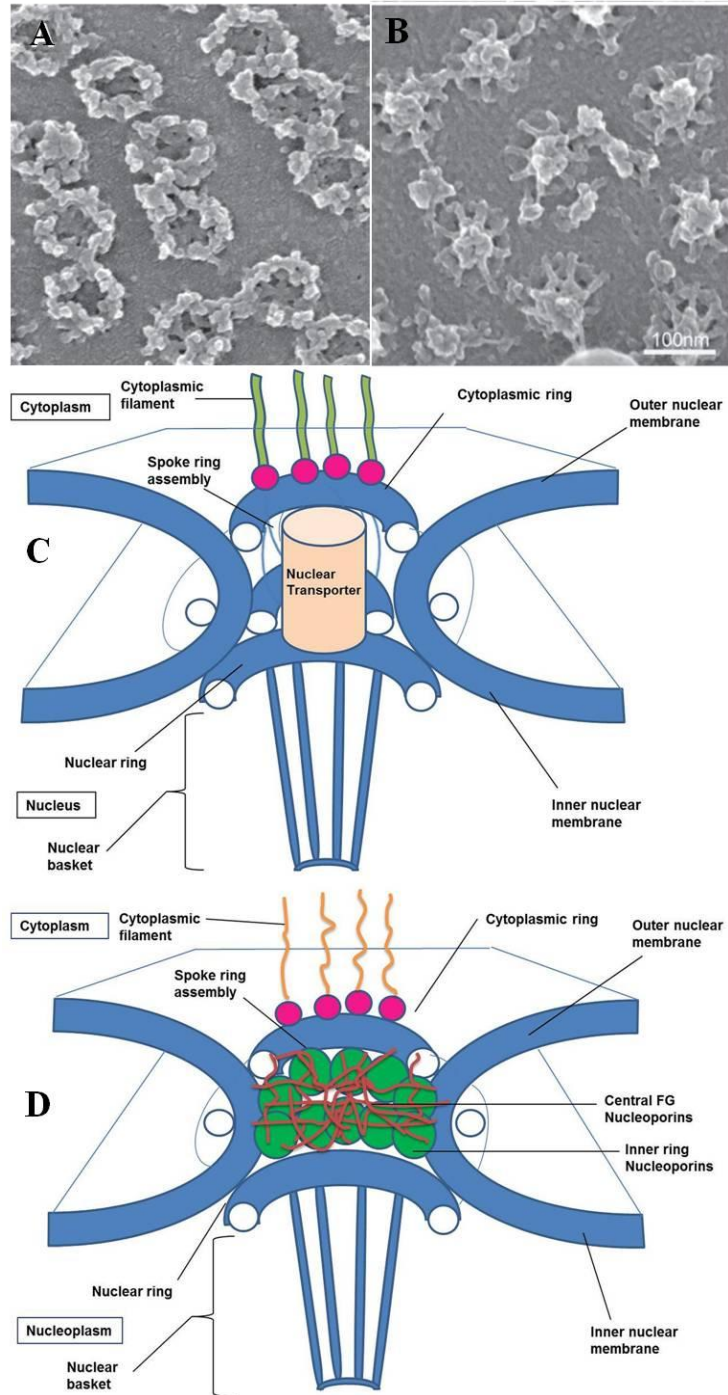


Figure 1.2: Structure of nuclear pore complex. Electron microscopy images of NPCs of the nuclear side (A) and cytoplasmic side (B) of a *Xenopus laevis* oocyte nuclear membrane from Science, 2007: 318, 1412-1416 – Copy right License Number: 3582310015444 (Terry *et al.*, 2007). There are two models of structure of NPC. Schematic drawings of cross-section of the NPC showing major components in single channel model (C) multi-channel model (D).

Electron microscopy studies suggests a three-dimensional model of the NPC exhibiting octagonal symmetry (Terry *et al.*, 2007). The main part of the pore forms a cylindrical structure fixed in the nuclear envelope, which is sandwiched between a nuclear ring and a cytoplasmic ring. These ring structures are anchoring sites for cytoplasmic and nuclear filaments. The latter are not flexible but connected by distal ring, thereby forming nuclear basket. The central channel of the pore is filled with FG repeats which form a meshwork through hydrophobic interactions (Frey *et al.*, 2006) thereby creating the permeability barrier of NPCs. According to the selective phase model (Ribbeck & Gorlich, 2001), transport receptors transiently dissolve the meshwork through interactions with the FG repeats. Schematic drawings in figure 1.2. shows the cross-sections of the nuclear pore complex showing major components in single channel model (C) multi-channel model (D).

1.1.5. Active and Passive modes of Nuclear Transport

The NPC can function as a passive diffusion channel, as an ion channel, or as a macromolecule shuttle channel, transporting materials bidirectional between the cytoplasm and the nucleus. On one hand, the nuclear pore complex contains a passive diffusion channel for transportation of small molecules (< 10 nm, MW < 60 kDa) (Tate & Elborn, 2005, Rout *et al.*, 2000, van der Aa *et al.*, 2006, Johnson *et al.*, 2013, Huang *et al.*, 2010, Katta *et al.*, 2013, Bagley *et al.*, 2000, Adam, 2001). Passive diffusional transport is a movement of biochemicals and other molecular or atomic substances across nuclear envelopes. The passive transport takes place through simple diffusion through the concentration gradient and the rate of diffusion will critically depend on the size on the pores. The size of inactively transported substances may range from that of freely penetrable mono and divalent ions up to ~40 kDa (Mooren *et al.*, 2004, Lee *et al.*, 1998). On the other hand, energy is utilized to facilitate the transport of larger molecules (Kleinsmith & Kish, 1995). The mechanism of active translocation through NPC involves interactions between the soluble carriers and proteins present inside the NPC (Wente & Rout, 2010, Strambio-De-Castillia *et al.*, 2010, Schuldt, 2012, Kapon *et al.*, 2010).

Many cell proteins are too big to pass by passive diffusion through the NPCs; the nuclear membrane allows the nuclear section and the cytoplasm to maintain different complements of proteins. Developed cytosolic ribosomes are about 30 nm in diameter and thus cannot passively

diffuse through the 9 – 10 nm channels; their rejection from the nucleus ensures that protein synthesis is confined to the cytoplasm. Passive transport is independent of GTP hydrolysis and involves diffusion of species lacking specific nucleus localization sequences. To date, much of what is known of the NPC structural design and size comes from elegant electron microscopy studies and, to a minor extent, atomic force microscopy investigations. The previous studies have provided a detailed view of the size estimation of nuclear pore channel in NPC (Peters, 1983b, Peters, 1983a, Peters, 2005, Peters *et al.*, 2002, Mohr *et al.*, 2009). Diffusion size limit for passage of solutes between nucleus and cytoplasm is 10 nm, corresponding to a globular protein of 45 – 68 kDa. However, passive diffusion for few proteins even within this limit is exceedingly slow (Mohr *et al.*, 2009).

Active transport is the movement of molecules across the nuclear envelope against their concentration gradient. Transport of large proteins into nucleus needs nuclear localization signal (NLS). Nuclear import receptors bind NLS and nucleoporins. A typical NLS contains several repeated basic amino acids. Many proteins, steroid hormone receptors, tumor suppressor proteins, endogenous transcription factors, as well as nuclear lamins, contain NLS (Vancurova *et al.*, 1995, Bastos *et al.*, 1995, Macaulay *et al.*, 1995, Simos & Hurt, 1995). These NLS sequences are rich in positively charged amino acids, particularly Lysine and Arginine (Akey, 1995, Chatel & Fahrenkrog, 2012, Dean & Kasamatsu, 1994, Simos & Hurt, 1995). Nuclear export works like nuclear import, but in reverse hnRNP proteins have a nuclear export signal (NES).

1.1.6. DNA Import into Nucleus

One of the macromolecules whose nuclear transport is often over looked and underappreciated is exogenously administered DNA. While extra chromosomal DNA may not be a usual species in the cell, its nuclear localization is integral to the life cycles of many pathogens and necessary for the success of transfections in the laboratory and gene therapy in the clinic. No transcription, integration, replication, maintenance can take place without localization of DNA into the nucleus. Surprisingly, there has been relatively less attention directed towards either discovering or exploiting the mechanisms used by the cell to direct DNA into the nucleus, even though it is important in gene therapy.

Wolff and colleagues demonstrated that linear fragments of labeled double stranded DNA can localize to the nuclei of permeabilized cells in a reaction that is inhibited by agents that block the NPC and by energy depletion (Wolff & Budker, 2005, Zhang *et al.*, 2004). DNA fragments less than 1000 bp in length are able to accumulate in the nucleus, but longer fragments remained left out from the nucleus (Ludtke *et al.*, 1999). Moreover, DNA nuclear import is inhibited by the addition of cytoplasmic extracts (Hagstrom *et al.*, 1997). Hangstrom *et al.*, confirmed that nuclear localization of the labeled DNA is energy dependent and occurred through the nuclear pore, but did not involve the addition of soluble cytosolic protein factors necessary for protein import. This is in dissimilarity to what has been seen for the nuclear import of NLS-containing proteins and snRNAs. Possibly the reason for these differences is that the DNA fragments used are highly conjugated to fluorescent tags. Thus, the properties of the DNA may differ from the native DNA. In contrast to the results with linear fragments of DNA, when the Wolff group used plasmids, they found that nuclear uptake in permeabilized cells depends on cytoplasmic extracts only when the DNA is covalently cross-linked to a number of NLS peptides (Vacik *et al.*, 1999, Wilson *et al.*, 1999). To characterize the mechanisms and size limit of DNA nuclear import in more detail, and to identify the rate of DNA transport involved, we have used permeabilized cell system.

1.2. OPTICAL MICROSCOPIC TECHNIQUES

Microscopes are instruments designed to generate magnified visual or photographic images of very fine objects in micrometer range. Optical microscopic techniques have helped in revealing a better picture of biological functions. In recent years, this microscopic technology has become extensively available and there are an increasing number of biological researches using live cell imaging techniques. Several microscopy techniques have been established which allow researchers to study living cells in better detail. Newer types of imaging using nanoparticles or quantum dots have been developed as they show more photo-stability.

It was difficult to observe living cells before the development of the phase contrast microscope. As living cells are translucent they have to be stained to be observable in conventional light microscopes while the processes of staining cells normally kill the cells. Phase

contrast methods used to detect unstained cells are differential interference contrast (DIC) and Hoffman modulation microscopy (Stephens & Allan, 2003, Parsons & Johnson, 1972, Liang *et al.*, 2000). Phase contrast microscopes do not have the capability to detect particular proteins or other compounds which constitute the complex machinery of a cell. Fluorescent stains have consequently been established to label such compounds, making them visible using fluorescent microscopy techniques (Keller & Pisha, 1947, Jarrett *et al.*, 1956, Keohane & Metcalf, 1958, Holland & Ackermann, 1961, Doxiades & Candreviotis, 1962). The use of fluorescent proteins in modern cell biology with microscopy techniques has provided a remarkable boost on our capability to study dynamic processes in living cells (Johnson & Straight, 2013, Fu & Sztul, 2015). Live cell imaging/optical microscopic techniques are becoming a vital method for cancer biology, developmental biology, cell biology, and many other related biomedical research laboratories.

1.2.1. Confocal Microscopy

Confocal microscopy is a powerful device for producing high resolution images and 3-D reconstructions of a sample. Confocal microscopy presents an imaging system that allows for a high contrast image of a single plane within an optically clear material. This is achieved by blocking the majority of the out of focus light that acts to degrade the quality of the image in conventional microscopy. In confocal system the light source and detector are in optically conjugate focal planes, thus the name confocal.

The concept of the confocal microscope was first introduced by Marvin Minsky in 1957 and was established by Eggar and Petran nearly ten years later (Egger & Petran, 1967). It is not until the late seventies that major breakthroughs occurred due to the development of lasers, electronic computers and image processing. Dutch physicist Fred Brakenhoff established a scanning confocal microscope in 1979 (Brakenhoff *et al.*, 1979), while almost simultaneously, Colin Sheppard contributed to the technique with a theory of image formation (Sheppard & Wilson, 1979). Point light source is usually a laser diverged by the pinhole, sometimes a lens, and focused onto the sample as diffraction limited spot by the objective lens. The pinhole in front of the detector rejects the out of focus scattered light, but allows the in-focus scattered light through. This eliminates the majority of out of focus scattered light from degrading the received

signal (Carlsson *et al.*, 1985, Sheppard & Wilson, 1981). This allows the detector to comprise a single pixel light power detector such as photodiode, photomultiplier tube or an avalanche photodiode. A two-dimensional image can be created by scanning the sample with the focused beam of light. This is achieved by either moving the target with a motorized stage while the focused spot remains stationary (stage scanning), or by implementing optical elements, such as a scanning mirror to move along the target in one axis, and then the other (laser mirror scanning).

Confocal microscopy uses lasers, the most common being a gas laser such as Argon laser. When the laser light is focused on the focal plane significant fluorescence is produced above and below the focal plane as well. This fluorescence, if it makes its way to the photon multiplier tube (PMT), will cause blurring of the final image. A pin hole is introduced between the specimen and the detector to get rid of this out of focus light. Light outside of the focal plane is largely excluded from hitting the PMT. The geometry of the light in the focal plane is such that it passes through the pin hole and is thus detected by the PMT. Thus, the focus plane of illumination is the same as the focal plane of detection. This combination generates a sharp image or optic section of the situation inside the specimen. Figure 1.3 shows the working procedure and a schematic diagram of a confocal microscope.

Different types of confocal microscopes are available depending upon the usage. They are

- Confocal laser scanning microscope
- Spinning disk confocal microscope
- Programmable array microscope
- Deconvoluted microscope
- Multi-photon imaging microscope
- *In vivo* reflectance confocal microscopes

In biological applications particularly, the sample possibly will be fluorescent. Reflected and scattered laser light as well as any fluorescent light from the illuminated spot passes back through the objective lens. A beam splitter splits off portion of light into the detection apparatus. After passing a pinhole, the light intensity is detected by a photodetector transforming the light signal into an electrical one that is recorded by a computer. In our applications a confocal laser

scanning microscope is used to measure the intensity of the emitted fluorescence signal from the cell nucleus during nuclear transport studies and thus to create a digital image from the signal.

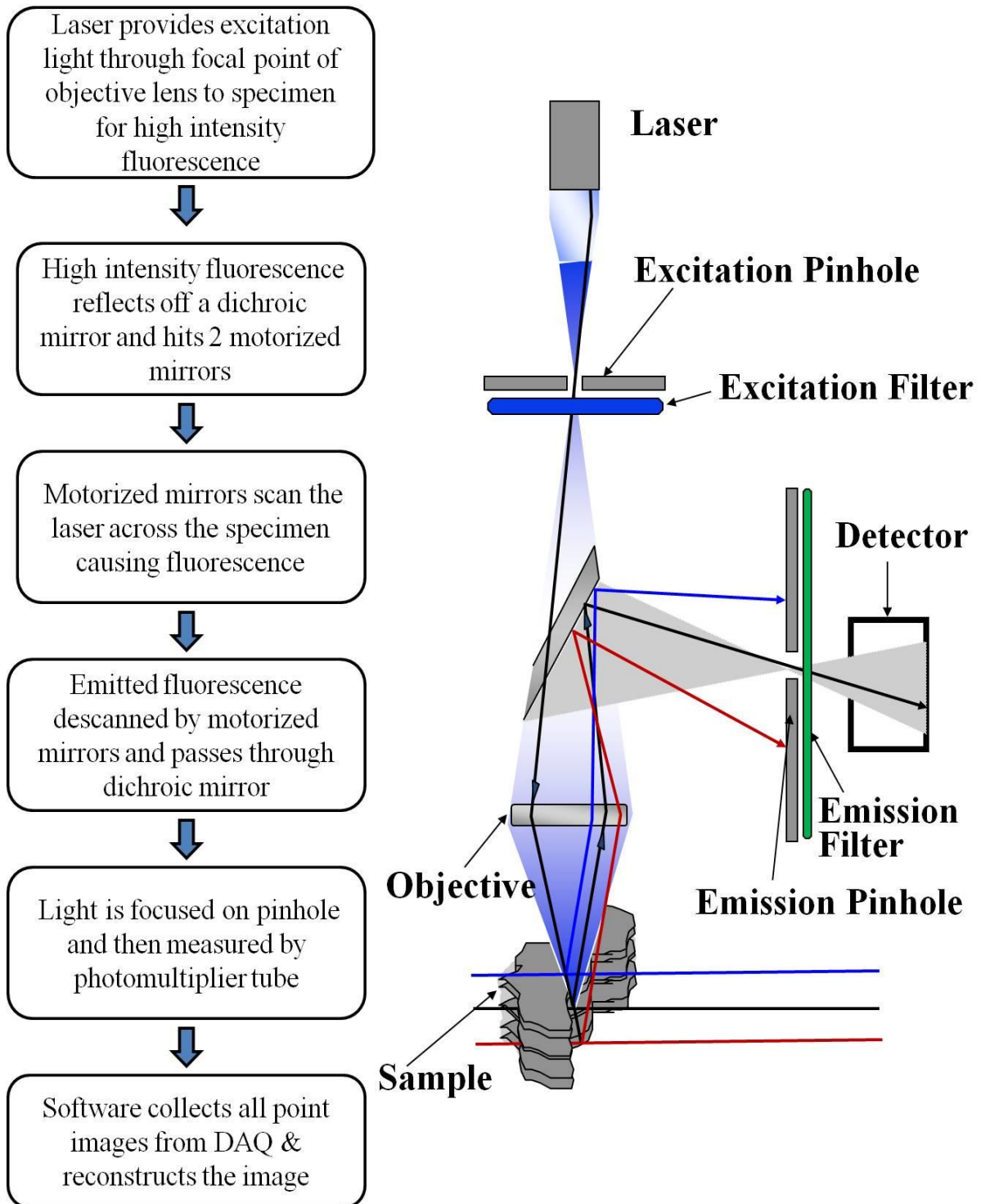


Figure 1.3: Working procedure and a schematic diagram of a confocal microscope.

The important advantages of confocal microscopes are as follows,

- Increased effective resolution
- Reduced blurring of the image from light scattering
- Improved signal to noise ratio
- Clear examination of thick specimens
- Z-axis optical scanning and depth perception in Z-sectioned images

The broad range of applications available to confocal laser scanning microscopy includes a wide variety of studies in neurophysiology and neuroanatomy, as well as morphological studies of cells and tissues. However, majority of the fluorescent stains are phototoxic and photo degradable. This limits their use in monitoring living cells over an extensive time period. Another difficulty faced in biomedical imaging using confocal fluorescence microscopes is the instability of dye labels used, which undergo photo-bleaching under the excitation of laser light. This hinders the observation of transport phenomena for a longer duration of time. So the development of alternative imaging tools making use of photo-stable and versatile probes, such as nanoparticles would help immensely for imaging biomolecules in live cells for an extensive time of experiment.

1.2.2. Photothermal Microscopy

Photothermal microscopy is a technique that is based on detection of non-fluorescent labels. It relies on absorption properties of labels such as gold nanoparticles or semiconductor nano crystals. Photothermal microscopy can be realized on a conventional microscope by making use of a pump-probe detection arrangement. A resonant modulated heating beam is used to change the temperature around a particle of interest and a second probe laser is used to detect this temperature change. High selectivity and sensitivity of photothermal microscopy permits even the detection of single particles by their absorption.

Gold nanoparticles in small percentages are biocompatible and can be used with ease to bind to specific molecular targets. The spatial distribution of these functionalized nanoparticles can be detected with photothermal microscopy and thus the molecule of interest inside a cell can be mapped. Gold nanoparticles inside fixed cells are imaged by Pache *et al.*, using photothermal

optical coherence microscopy (Pache *et al.*, 2005). Polarization interference contrast photothermal microscopy has been successfully employed to visualize membrane proteins using 10 nm gold nanoparticles as labels. Lasne *et al.* are able to track individual 5 nm gold nanoparticles on live cells using photothermal microscopy (Lasne *et al.*, 2006). The tracking scheme is designed based on triangulation from three measurement points to record the trajectories of single membrane protein labeled with gold nanoparticles in live cells. In this setup imaging and tracking are performed by moving the sample over a fixed laser spot by means of a piezo-scanner with an integration time of 5 ms.

These studies show that photothermal microscopy provides a potential alternative tool for biomolecular imaging. The techniques discussed so far in the literature employ stage scanning to record a 2-dimensional image of gold nanoparticles. Stage scanning requires longer time to acquire an image and specimen motion is a challenge. In this work, we have employed a galvanometric mirror scanning technique to overcome this limitation. The ‘laser scanning photothermal microscopy’ allows fast detection and imaging of gold nanoparticles labels in biomedical imaging. The schematic diagram of the photothermal microscope is shown in figure 1.4.

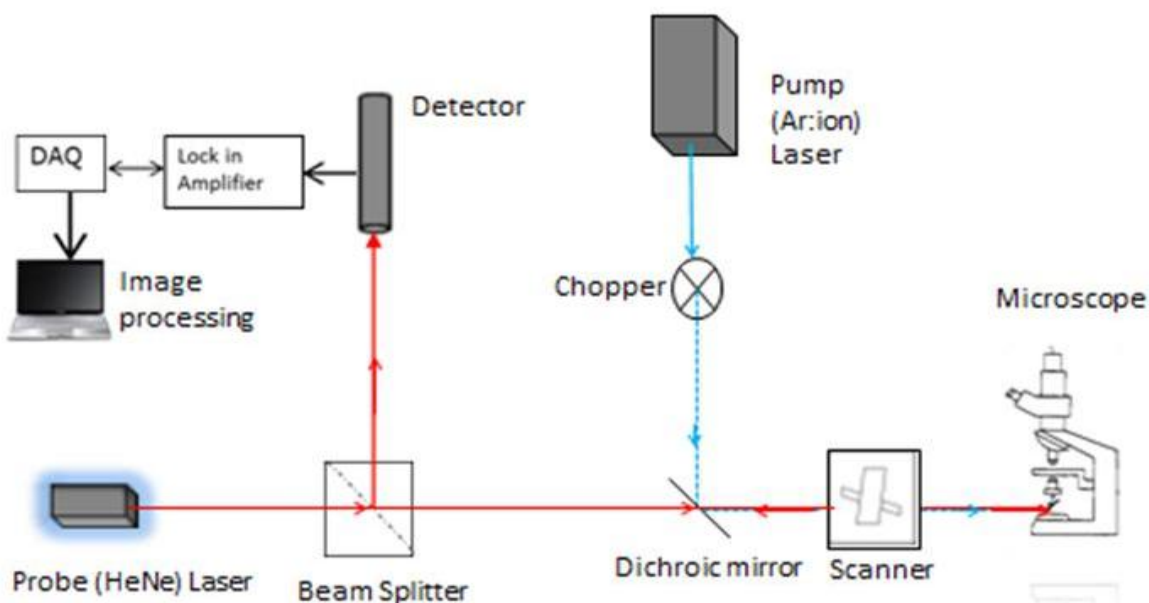


Figure 1.4: Schematic diagram of Photothermal microscope.

1.3. OBJECTIVES

Studies on biomolecular transport through membranes are of interest from a fundamental physics perspective as well as from the point of view of applications. The mechanism of this transport and different parameters that control the transport phenomena are not well understood. A proper understanding of the transport phenomena will help in developing methodologies which will be of interest in biomedical research, especially related to gene therapy. Optical micro-spectroscopic techniques can play a vital role in these studies.

In the current thesis we envisage to,

- Develop a low cost and flexible Confocal Laser Scanning Microscope for biomolecular imaging.
- Study the nuclear internalization of different biomolecules in digitonin permeabilized cell system.
- Investigate kinetics of transport of biomolecules through nuclear membranes to determine the passive permeability limit and effective pore size of nuclear membranes.
- Study the effect of Rabbit Reticulocyte Lysate in biomolecular delivery especially DNA into the nucleus through the nuclear pore complex.
- Develop an alternative imaging technique, based on photothermal detection, with photostable labels.

1.4. OUTLAY OF THE THESIS

The thesis is split into seven chapters. A brief introduction to the area of research work is given in chapter 1. This includes history of nuclear transport, different optical microscopy techniques employed in this imaging studies, results obtained by various authors, and its applications. More detailed literature on corresponding topics is given in each chapter.

Chapter 2 describes the construction of a confocal microscope, details of the materials and methods used in construction of simple confocal laser scanning microscope and its standardization using different standard microparticles and biological test slides. The images of test standards obtained using home built microscope are presented in this chapter.

Chapter 3 discusses the methodology of preparation of cells, optimization of digitonin permeabilization in cells, nuclear import procedure and time lapse imaging scheme using confocal laser scanning microscope.

Chapter 4 presents the nuclear transport studies carried out using FITC labeled dextrans and the results obtained from its kinetic analysis. Passive permeability limit and functional nuclear pore size estimations are reported in this chapter.

Chapter 5 describes the details of preparation of different size of DNA fragments and its labeling and the nuclear transport of these DNA molecules. The effect of Rabbit Reticulocyte Lysate on nuclear transport of different sizes of Dextran and DNA molecules are presented.

Chapter 6 discusses the methods used in construction of laser scanning photothermal microscope that can detect and image gold nanoparticles at fast time scales. Photothermal imaging of gold nanoparticles of different sizes and the photothermal intensity dependence with different parameters are also discussed. The preliminary results obtained on photothermal imaging of gold nanoparticles in living cells are also given in this chapter.

In Chapter 7, the conclusions and future scope of research work is presented along with a summary of results and recommendations for future research.

CHAPTER TWO

DESIGN AND CONSTRUCTION OF A CONFOCAL LASER SCANNING MICROSCOPE FOR BIOMOLECULAR IMAGING

2.1. INTRODUCTION

Confocal fluorescence microscopy is one of the most popular and widely used imaging techniques in Biology. High sensitivity, spatial resolution and optical sectioning capability make it an ideal tool in the study of biological systems such as membranes, tissues and cells (Paddock & Eliceiri, 2014, Stephens & Allan, 2003, Nwaneshiudu *et al.*, 2012, Pawley, 2006, Wilson & Sheppard, 1984). However most of the commercial confocal fluorescence microscope designs are not versatile enough to be employed in different laboratory configurations or as an educational tool for students in an undergraduate laboratory setting. Further commercial confocal microscopes are very expensive and not affordable to many laboratories, especially in India. The lack of flexibility and high cost of commercial systems have prompted us to construct a confocal fluorescence microscope optimized for biomolecular imaging under different configurations.

In this chapter we report on our design of a simple and flexible confocal laser scanning microscope (CLSM) that can be used for research as well as for undergraduate teaching. An inverted microscope, data acquisition card, laser and optics, normally available in an optics laboratory, are used in the construction. An X-Y galvanometric mirror scanner working at 512 Hz and 2 Hz respectively is used to raster scan the sample and to construct images at a maximum rate of 4 frames per second. The design is versatile and can be used in both reflection and fluorescence mode. The same set up can readily be used in other microscopy applications such as photothermal or multiphoton microscopy with minimal modifications.

2.2. CONFOCAL FLUORESCENCE MICROSCOPY

A confocal microscope makes use of a laser as the excitation source so that it can be tightly focused on the sample. Fluorescence from the focal point alone is passed to a photodetector kept at the conjugate focal plane of the objective lens and an aperture of appropriate dimension blocks all out of focus light from reaching the detector. This confocal detection helps in improving the axial resolution of the microscope and results in sharper images. Two dimensional images of the sample slices are acquired point by point either by moving the laser beam over the sample (laser scanning) or by moving the sample (stage scanning) in the X-Y plane. The stage scanning typically requires larger time to acquire an image and is more expensive compared to the laser scanning.

In this work we have used either an Argon ion laser (488 nm) or a green HeNe laser (543 nm) as the excitation source. A silicon photomultiplier (SPM) with a transimpedance pre-amplifier is used as the detector and the fluorescence is coupled to the detector through an optical fiber. The optical fiber also acts as the confocal aperture. The SPM is as sensitive as a normal PMT in the 500 nm region of wavelength and does not require a high voltage power supply. A galvanometric mirror scanner is used to scan the laser beam over the sample and thus to acquire a two dimensional image of the sample. A data acquisition (DAQ) card provides the voltage wave forms for X and Y scan mirrors, acquires the voltage output from the silicon photomultiplier in a synchronized manner, and constructs the image by sequentially digitizing the signal. An Olympus IX-71 inverted microscope equipped with an oil immersion 60X objective of numerical aperture 1.25 is used in the construction of CLSM. A CCTV camera mounted at the right side camera port is used for initial focus adjustments. The left side optical port of the microscope is used as the input port for the excitation laser beam. The scan lens is mounted at the primary image spot, at a distance of 102 mm from the left side optical port. Optical components, along with the microscope are tightly mounted on a vibration free optical bench and the alignment of optical components is achieved with a range of adjustable mounting posts.

2.3. MATERIALS

2.3.1. Details of Components used in CLSM Construction

More details of the main components used for the microscope constructions are given below.

Lasers

We have used a HeNe laser (Model: 25-LGR-393-230, CVI – Melles Griot, USA) with the wavelength of 543 nm or an Argon ion laser (Model: 35-LAP-321-230, CVI – Melles Griot, USA) with the wavelength of 488 nm as an excitation light sources for acquisition of images shown in this chapter.

Galvanometric Mirror Scanner

Galvanometric scanner (Model: 6215H M40, Cambridge Technology Inc., USA), single axis X-Y scanners along with control board is used for the scanning purpose. A 28 V power supply and cooling fans are used for the scanner.

Dichroic Mirror

Dichroic mirrors/beam splitters spectrally separate light by reflecting and transmitting light as a function of wavelength. Reflection and transmission are 50% at the cutoff wavelength. We have used 488 nm long pass dichroic mirror (Model: LWP-45-Rp-488-Tp-633-PW-0525-C, CVI – Melles Griot, USA) during optimization of our microscope. And later on we started using long pass dichroic mirror with cutoff wavelength 503 nm (Model: 86-392, Edmund optics Inc., USA) for biological imaging and nuclear transport studies.

Band Pass Filter

A band pass filter is a device that allows wavelengths of light within a certain range and blocks wavelength outside that range. The green detection channel (for Argon ion laser with 488 nm) held a 550 ± 40 nm band pass filter (Model: F40-550.0-4-25.0M, CVI – Melles Griot, USA) in front of photomultiplier tubes. Band pass filters provide one of the simplest ways to transmit a well-defined wavelength band of light, while rejecting other unwanted radiation.

Optical Fiber

An optical fiber is a flexible, transparent fiber made of extruded silica glass or plastic. It can function as a waveguide, or “light pipe”, to transmit light between the two ends of the fiber. Manufacturers offer single mode patch cables with FC/PC connectors. We used optical fibers with different radius depending upon the focal length of the lens in fiber coupler so as to have the desired axial resolution.

Data Acquisition Card

The NI USB-6251 BNC obtained from National Instruments Corporation, USA is a USB high-performance M Series multifunction data acquisition (DAQ) module optimized for greater precision at fast sampling rates. The NI USB-6251 BNC provides 8 analog input, 2 analog output, 8 DOI, 1 APFI and 2 user defined BNC terminals. It is ideal for applications such as data-logging.

Photodetector

We have used either a photomultiplier tube (PMT) module (H7732-10) from Hamamatzu or a silicon photomultiplier with a transimpedance pre-amplifier (Model: MiniSM-30035-X08, SensL, Ireland) as a photo detector.

The H7732 series photosensor elements comprise of a 28-mm (1-1/8") diameter side-on photomultiplier tube (PMT) and a high voltage power supply. These PMTs have long been used for spectroscopic applications and provide high gain and high sensitivity. H7732-10 model PMT is sensitive over a wide range from UV to near infrared and has particularly high sensitivity in above 600 nm wavelengths.

The SensL MiniSM includes a MicroSM-30035-X08 Silicon Photomultiplier (SPM) with a transimpedance pre-amplifier, a circuit with Peltier cooler driver to enable cooling and an integrated power supply. The SPM detector is mounted on a single stage Peltier cooler and kept in a closed container. This SPM allows better performance over room temperature process as the dark rate is reduced by over an order of magnitude.

LabVIEW

LabVIEW is the short form for Laboratory Virtual Instrument Engineering Workbench. It is a system design platform and development environment for a visual programming language from the company of National Instruments Corporation, USA. National Instruments LabVIEW is commonly used for different purposes like instrument control, data acquisition, and industrial automation on a variety of platforms including Microsoft Windows. In this work a LabVIEW based software is used for interfacing and control of the optical scanner and the acquisition of data from the photomultiplier tube.

Microscope

An inverted Olympus IX71 (Olympus Corporation, Japan) microscope is used in the experiments. Microscope features phase contrast, transmission or reflectance bright field, and epifluorescence options. Microscope includes 10X objective and 60X oil immersion objective. The left side optical port which is near the bench level is used as the input port for the excitation laser as well as exit port for the fluorescence.

Optical Mountings

The integration and alignment of optical components with the microscope is achieved with a range of adjustable mounting posts. Optomechanical components are obtained from Holmarc Opto-Mechatronics Pvt. Ltd., India. All components are mounted on standard post mounts fixed to an optical table with pneumatic isolator (Model: RS 2000 series, Newport, USA).

2.3.2. Standard Microparticles and Biological Test Slides

Standard Microparticles

Polystyrene microparticles are negative charge-stabilized colloidal particles. The microparticles are manufactured by polymerization of styrene under circumstances that induce spontaneous coalescent bead formation. Polybeads are provided as aqueous suspensions. Micro particles based on polystyrene of different size (0.1 μm and 1 μm) are obtained from Sigma Aldrich Pvt. Ltd., Bangalore. Silica gel beads of size 5 μm and 10 μm are obtained from LGC Promochem Pvt. Ltd., Bangalore.

Pollen Grains

Dye labeled pollen grains (Model No. 304264) test slide is obtained from M/s. Carolina Biologicals, USA.

Fluo Cells

FluoCells prepared microscope slide (Model: F-36925, Invitrogen Corporation, USA) contain multilabeled muntjac skin fibroblast cells preparations for observation by fluorescence microscopy. These cells are stained with a mixture of three different fluorescent stains. The prominent filamentous actin in these cells is labeled with the fluorophore Alexa Fluor 488 phalloidin.

2.4. EXPERIMENTAL METHODS

2.4.1. Confocal Laser Scanning Microscope Setup

The overall layout of the optical system used for the construction is shown in figure 2.1. The laser beam is directed to the scanning mirrors (X and Y) by a dichroic mirror (DM). Mirrors M1 and M2 help to align the beam centrally through the scan mirrors and to the inverted microscope. The laser beam reflects off the two scan mirrors and is focused to the conjugate plane of the microscope by the scan lens (SL). The optics of the microscope relay the scanning spot to the specimen which is appropriately fluorescently labeled. The emitted fluorescence returns along the same pathway and is de-scanned by the same scan mirrors and transmitted to the detector through the DM. Mirrors M3 and M4 direct the fluorescence to a focusing lens (FC). This lens focuses the light to an optical fiber mounted on a translation stage, and the optical fiber guides the fluorescence to the silicon photomultiplier. This optical fiber also acts as the pinhole for the confocal system. One can choose the axial resolution and thereby the thickness of the optical slice by using lens of appropriate focal length and fiber core diameter. An additional band pass filter is used to remove the excitation laser leaking through the dichroic mirror. For reflection mode the band pass filter is replaced with a neutral density filter.

The set up can be modified by incorporating a second (probe) beam, such as the 632 nm from HeNe laser or 800 nm from a Ti: Sapphire laser, introduced through the M3 so as to have photothermal or multiphoton imaging capability. Table 2.1 shows the details of the components used in CLSM setup and their costs.

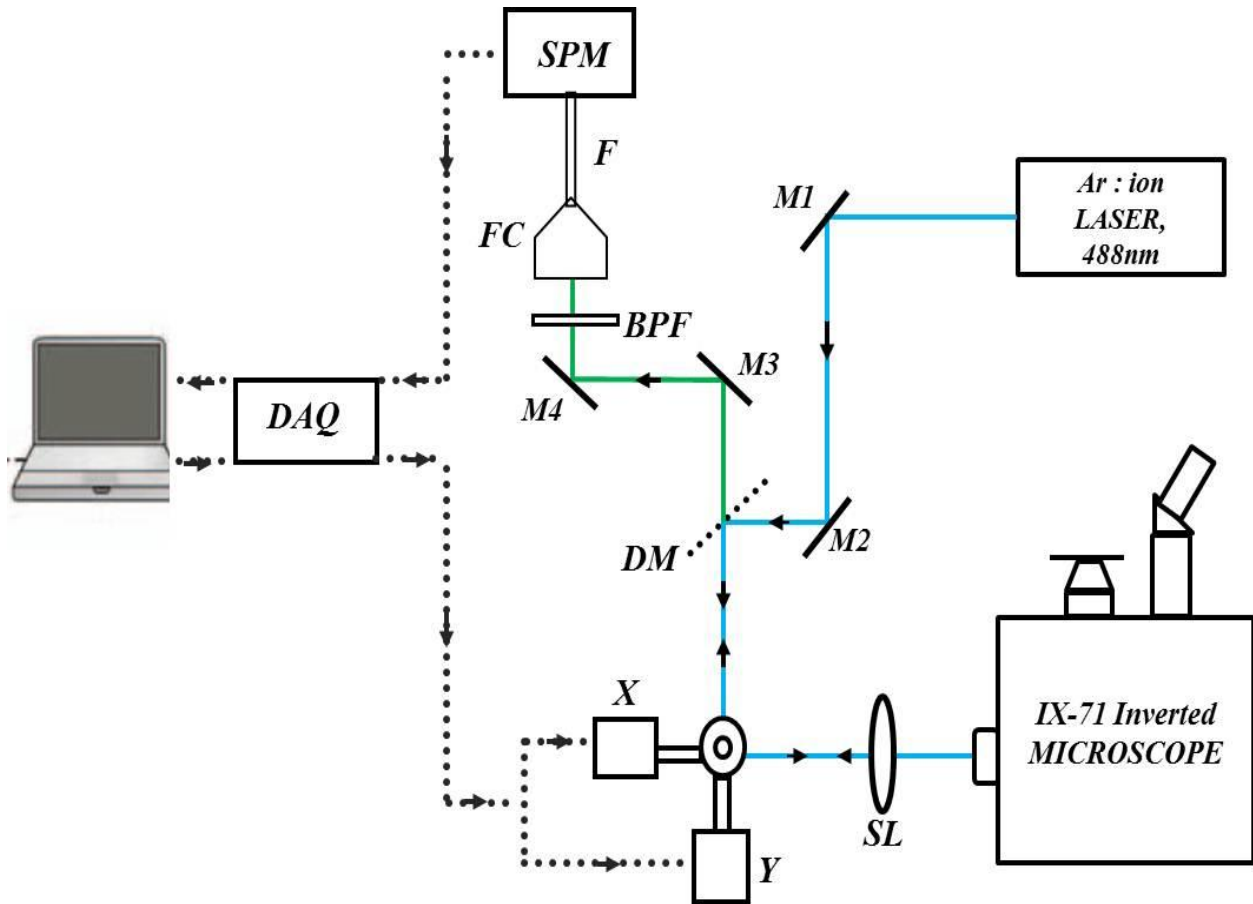


Figure 2.1: Experimental setup of the Confocal Laser Scanning Microscope. SL – Scan Lens, X and Y – Scanning mirrors, DM – Dichroic Mirror, FC – Fiber Coupler, F – Optical Fiber, BPF – Band Pass Filter, SPM – Silicon photomultiplier, M1-M4 – Mirrors and DAQ – Data Acquisition Card.

2.4.2. Data Acquisition and Image Acquisition Software

It is important to develop appropriate imaging software for the successful implementation of confocal microscopy. Many open source softwares are available that can be custom integrated for confocal microscope applications (Koch *et al.*, 2010, Pologruto *et al.*, 2003). We have used a LabVIEW based software program for image acquisition. The software controls the galvanometric mirrors by providing the necessary voltages and acquires the voltage output of the detector. The scanning is achieved by providing a saw-tooth waveform to the scan mirrors. The entire program is divided into 4 modules. Program in module 1 and 2 is responsible for system initialization. Module 3 is used for generation of X-Y scanner voltage and triggered voltage measurement. Module 4 is used for post processing of scanned images such as generation of colour table and saving the scanned image data.

Front End of LabVIEW Program

Figure 2.2 shows the front end of the software employed. Before the program is executed, the following points are checked.

1. Appropriate input and output channels are selected from the pop-up menu.
2. Input terminal configuration is set to “RSE.”
3. Frequency X is not more than the maximum allowed scanner frequency.
4. Appropriate number is entered into the “Avg 2^n ” input box. If 3 is entered then 8 ($2^3=8$) samples are averaged to calculate each pixel.

Once the program is executed the scanned image is displayed in the Intensity graph (figure 2.3). “Generate Color Table” can be used to generate new colour schemes and “Restore Colour Table” can be used to revert back to the default colour scheme. “Output Waveform Chart” will display the voltage given to X and Y scanner. The data can be exported to Matlab software (Mathworks) for further data analysis and image processing. The data is converted to .tiff image files using Matlab program. Figure 2.3 shows output tab of the front panel of the LabVIEW software used for data and image acquisition along with the images of 100 nm polyester beads taken by the microscope.

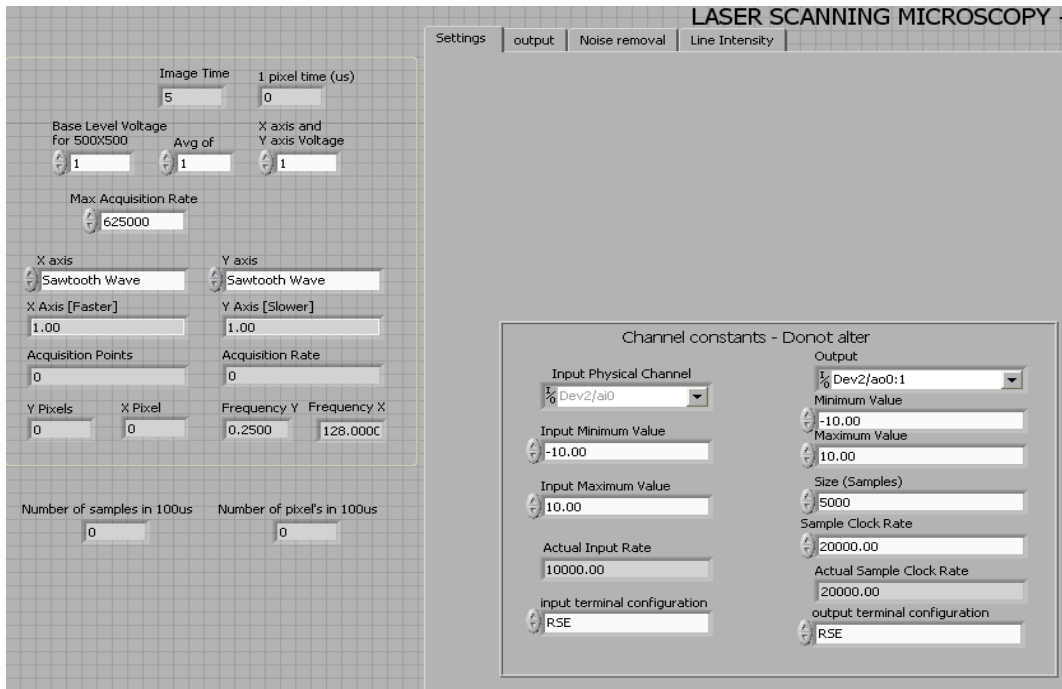


Figure 2.2: Contents of the settings tab in front panel of the LabVIEW program.

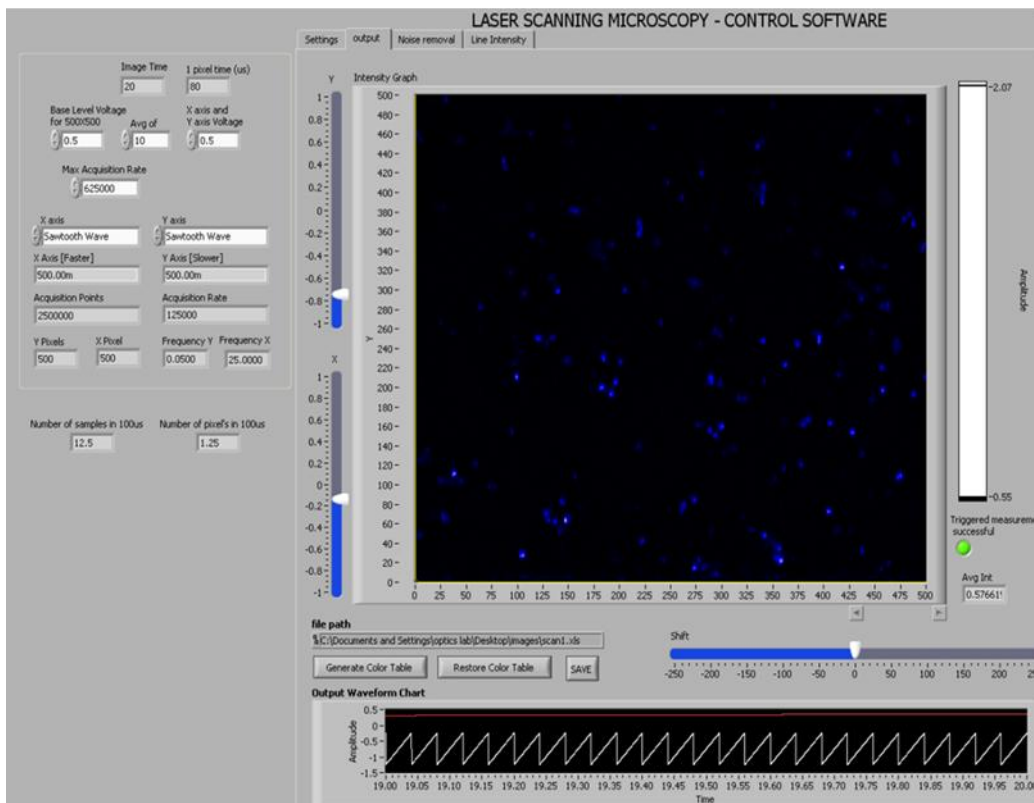


Figure 2.3: Contents of the output tab in front panel of the LabVIEW software used for data acquisition along with the image of polystyrene beads having a mean size of 100 nm.

Table 2.1: Components used in the construction of CLSM along with cost

No.	Item	Model	Make	Cost in INR
1.	Galvanometric scanner with power supply	6215H M40	Cambridge Technology	129153
2.	Microscope	IX71	Olympus Corporation	495044
3.	Data acquisition card	NIDAQ USB-6251	National Instruments	72443
4.	Ar-ion Laser	35-LAP-321-230	CVI - MellesGriot	317390
5.	Silicon Photomultiplier	MiniSM-30035-X08	SensL	102000
6.	Fiber Coupler Unit	LFC1	HolmarcOpto-Mechatronics	10000
7.	Dichroic Mirror	LWP-45-Rp-488	CVI - MellesGriot	33750
8.	Filter	XLP-514.5-25.0M	CVI - MellesGriot	31275
9.	Mirrors (5)	5108	New Focus	15075
10.	Posts (10)	P30	HolmarcOpto-Mechatronics	650
11.	Post Mounts (10)	PH30	HolmarcOpto-Mechatronics	2050
12.	Mirror Mounts (5)	9807:1”	New Focus	23175
13.	Scan Lens	WHN10X-H	Olympus Corporation	7500
14.	Optical Bread board	LL-BB-60*60	HolmarcOpto-Mechatronics	18000
Total Cost				INR 12,57,505

2.4.3. Optical Alignment of the CLSM

It is necessary to develop a routine alignment procedure for the CLSM, especially for a homemade set up where one may need to make frequent changes for conducting experiments in different configurations. In the following we describe a step wise procedure which will aid in easy straightforward re-alignment of the system.

Step 1: First, the microscope is adjusted for uniform Kohler illumination procedure (Ernst Keller & Watkins, 2013). The microscope focus is fixed on any sample (e.g. standard microparticles or a strand of hair kept between the microscope cover slip and glass slide) by looking through the eyepiece using white light and the condenser lens. The scan lens is positioned approximately at a distance of 102 mm from the left side port of the microscope. Looking through the scan lens, its position is fine-tuned to have a clear, focused and centrally positioned view of the sample. This process is enabled by mounting the scan lens on a translation stage.

Step 2: The scan mirror is approximately leveled with the central axis of the eyepiece by adjusting the height of the scan mirror mounts. The X and Y scan mirrors have a height difference of 0.5 cm. The input to the microscope is at 9 cm from the ground. The optics is aligned at 8.5 cm from the table top before the scanner and at 9 cm after the scanner.

Step 3: Objective lens is turned to out of position, and a piece of lens cleaning tissue paper is placed over the open aperture. The laser beam is centered onto the X-scanning mirror using the mirrors M1 and M2. After that by adjusting the scanner, the beam is reflected off normally into the microscope so as to have maximum illumination at the open objective position. Subsequently the beam location is centered on the objective turret with the adjustments on mirrors M1 and M2 and scanner is fixed.

Step 4: The scanner is activated and positioned at zero position and it is again confirmed that the illumination remains centered on the objective turret. A saw-tooth waveform is applied to X, and Y mirror to observe that the beam moves symmetrically on objective turret. Fine iterative adjustments of the scan mirror assembly and mirror M1 and M2 may be needed to achieve this.

Step 5: The objective lens is placed back in its position and focused on a mirror (as a reflective object) placed on the stage. The laser light reflected from the mirror retraces the path and can be

observed on the transmission side of the dichroic mirror. If the mirror is kept at the correct focus of both the microscope objective and the scan lens, then a collimated reflected beam can be observed beyond the dichroic mirror. This beam along its path is traced using the backside of business card and is directed to the mirror M4.

Step 6: The reflected light from mirror M4 is directed to a focusing lens (FC). FC focuses the light to an optical fiber mounted on a translation stage, and the optical fiber guides the signal to the detector. Intensity of the signal reaching the detector is monitored with an oscilloscope and maximized by iteratively adjusting the position of the optical fiber. Once the signal is maximized, the detector is connected to the DAQ card.

Step 7: The mirror is replaced and a sample containing a uniform thin layer of Fluorescein or FITC dye is imaged to confirm even illumination. Standard sized fluorescent polystyrene beads are imaged to study the lateral and axial resolution and to verify image quality. Fine adjustments to the mirror M1 and M2 may be required on a day to day basis to optimize the signal.

2.4.4. Standardization of CLSM

To assess the performance of the CLSM system it is necessary to apply various types of tests to eliminate errors due to instability of light source, inhomogeneity of illumination, reflection and transmission of laser light from optical components into the detecting system, system noise etc (Zucker & Price, 1999).

Initial calibration of the CLSM setup is done with the different standard microparticle samples. We have used standard microparticles of 5 μm and 10 μm sized silica gel beads and 1 μm and 100 nm polystyrene beads for calibration of the microscope setup. The routine standardization procedure involves the measurement of lateral (X-Y) resolution and axial (Z) resolution. Lateral resolution can be found out from sub resolution sized particles. We have used standard micro particles of 0.1 μm polystyrene beads (Sigma Aldrich) for calibration of the microscope. Images of 1, 5 and 10 μm particles are also obtained. The axial (Z) resolution is measured using the 0.1 μm polystyrene beads, which shows the axial capability of our system. 60X, NA 1.25 oil immersion objective is used in the standardization procedure.

The performance of CLSM has to be evaluated by subjectively assessing a biological test slide for image quality. These inspections are vital if one is interested in making quantitative intensity measurements on experimental biological systems. We have used a dye labeled pollen grains test slide to study the biological applicability of the microscope. 1951 USAF Resolution Test Targets, 3" x 3" (Model: R3L3S1N – Negative, Thorlab Inc., USA) is used to calibrate the microscope against the applied galvanometer voltages.

The image size can be calculated using following formula,

$$L = 2 \times f_{ep} \times \tan \theta$$

Where L is the scanning length at the image plane of the objective, f_{ep} is focal length of the scan lens (25×10^{-3} m) and θ is the optical scanning angle. The optical scanning angle is twice that of mechanical scanning angle. Mechanical scanning angle for the scan mirrors is 1° per 1 V. For 1 volt applied to the scanner, the mechanical scanning angle will be 1° and optical scanning angle will be 2° .

The axial (Z) resolution of the confocal laser scanning microscope can be tested using a reflecting mirror. A single reflecting mirror is placed on the microscope stage. Standard microparticles of different sizes also used for the resolution test.

2.4.5. Optical Sectioning Capability

Sectioning of standard microparticles is done with $1\mu\text{m}$ polystyrene beads, $5\mu\text{m}$ and $10\mu\text{m}$ silica gel beads and pollen grains. Beads are doped with Rhodamine B and or Fluorescein by covalent labeling method (Lamprecht *et al.*, 2000). Different Z-sections of the dye doped silica gel beads are taken in the interval of $1\mu\text{m}$. Different Z-sections of the pollen grains are also taken by moving the microscope axial knob manually. Pollen grain optical sections are gathered in 2-micrometer steps perpendicular to the Z-axis.

2.5. RESULTS AND DISCUSSIONS

2.5.1. Resolution Test Targets

1951 USAF Resolution Test Targets, 3" x 3" (Thorlab, R3L3S1N – Negative) is used to calibrate the microscope against the applied galvanometer voltages. This 3" x 3" targets have 10 groups (-2 to +7) with 6 elements per group, offering a maximum resolution of 228.0 line pairs per mm. Figure 2.4 shows the image of USAF 1951 Test target with a triangular pulse of 3 V applied to the galvanometric scanner which has the image size of 129 μm . The measurement is repeated with different voltage values on the scan mirror and the scanning length on the sample per unit voltage is deduced to be 43 μm .

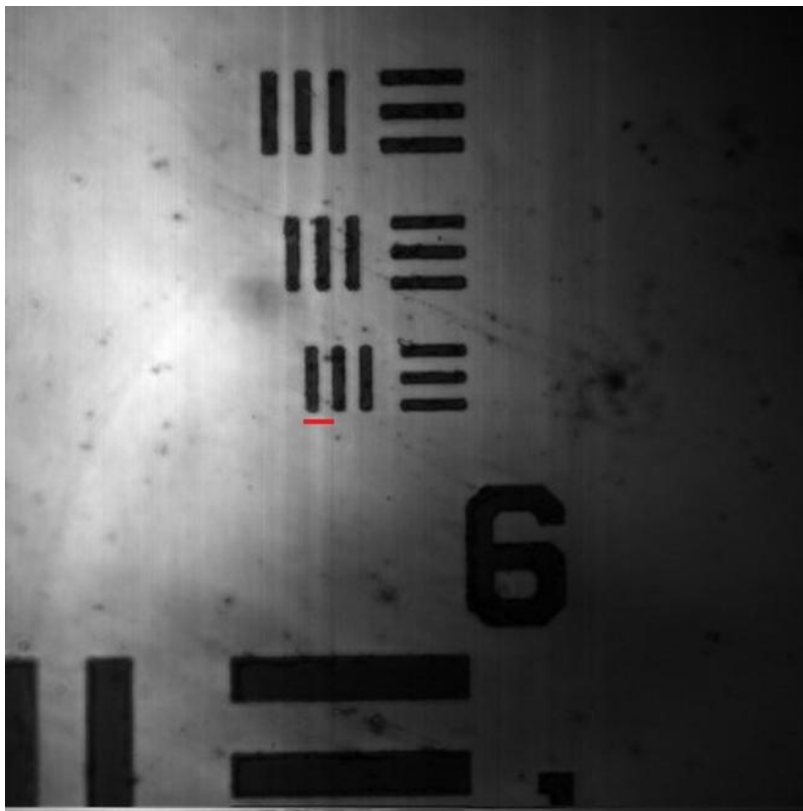


Figure 2.4: 500 \times 500 pixel confocal image of USAF 1951 test target obtained by providing a saw-tooth waveform of 3 V to the scan mirrors. There are 17 pixels between the smallest line pair (red line) corresponding to a specified distance of 1/228 mm. Thus 500 pixels in the image corresponds to 129 μm .

2.5.2. Standard Microparticles

The lateral and axial resolution of the microscope can be determined by studying fluorescent microspheres having a size much less than the resolution of the microscope. We have used 100 nm monodisperse polystyrene beads (Model: 90517-5ML-F, Sigma-Aldrich Chemicals Pvt. Ltd., USA) for determining the resolution. The samples are prepared by labeling diluted polystyrene beads with fluorescein dye. Figure 2.5 (A) shows the images of 100 nm polyester beads taken by the microscope. Figure 2.5 (B) shows the lateral intensity profile of a single polystyrene bead having a size of 100 nm. The profile has a full width at half maximum (FWHM) of 254 nm indicating the lateral resolution of the microscope. In order to determine the axial resolution of the confocal microscope one may acquire and study the cross-sectional images of a 100 nm polybead at discrete intervals. These image stacks, generally referred to as axial point spread functions, may be analyzed to determine the line intensity profile along the z-axis. Currently our microscope does not have automatic z-sectioning capability. Hence we have acquired the axial intensity profile by manually moving the microscope objective using the axial fine motion knob of the microscope. The axial intensity profile shown in figure 2.5 (C) has an FWHM of 880 nm, approximately three times that of the lateral resolution. Figure 2.6 (A) shows the images of 100 nm polyester beads acquired using CLSM. And the raw images are processed using ImageJ open source software and are shown in figure 2.6 (B) and (C). These 500×500 pixel images are acquired with 0.5 V applied to scanning voltage to laser scan mirrors.

An approximate theoretical resolution for confocal microscope as per the Rayleigh criterion can be expressed as (Cole et al., 2011, Xi et al., 2007)

$$\text{Lateral resolution} = \frac{0.61 \lambda_{exc}}{NA}$$

$$\text{Axial resolution} = \frac{0.88 \lambda_{exc}}{(n - \sqrt{n^2 - NA^2})}$$

Here λ_{exc} is the excitation wavelength of the laser, n is the refractive index of the immersion medium and NA is the numerical aperture. Here it is assumed that the pinhole size is equal to the size of the airy disk projected onto the pinhole plane. The airy disc size on the pinhole plane, and hence the pinhole diameter can be calculated using the relation (Xi et al., 2007),

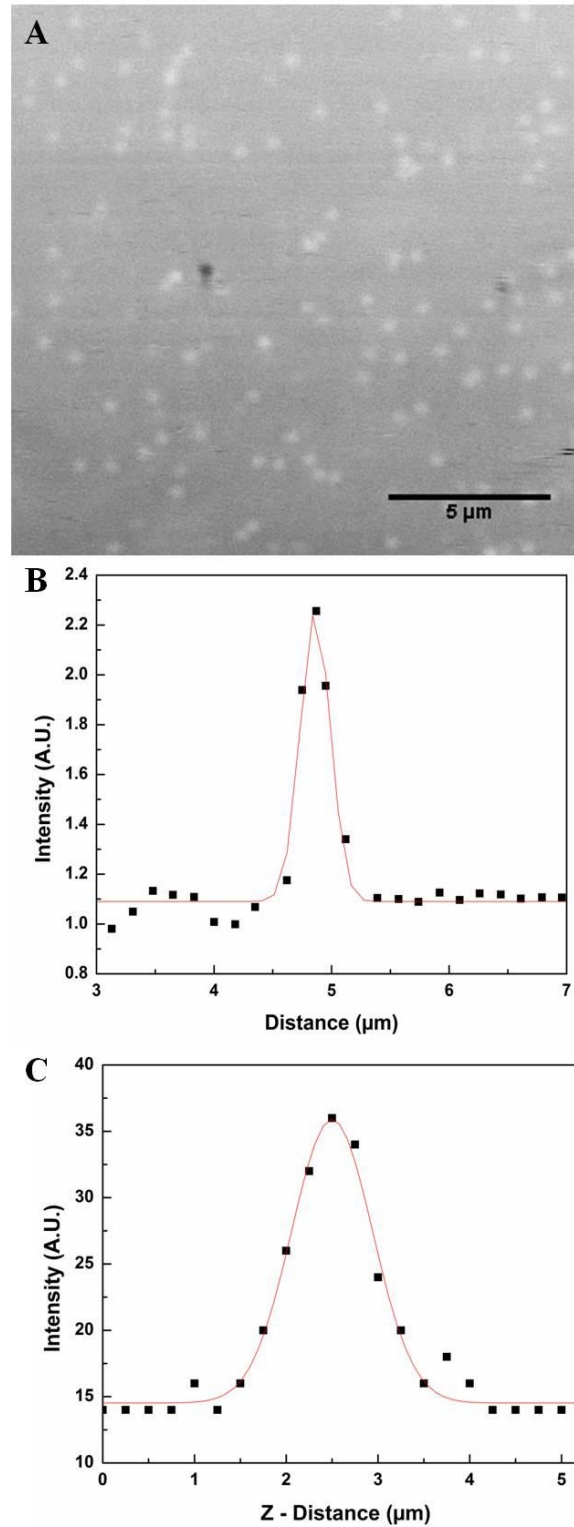


Figure 2.5: (A) Confocal image of polystyrene beads having a mean size of 100 nm. Lateral (B) and axial (C) line intensity profile of a single 100 nm polystyrene bead.

$$d_p = 2 \frac{f_{FC}}{f_{SL}} M_{OBJ} \frac{0.61 \lambda}{NA}$$

Where f_{FC} is the focal length of the detection lens, and M_{OBJ} is the magnification of the objective and f_{SL} is the focal length of the scan lens. In these experiments we have used a lens of focal length 120 mm to focus the fluorescent beam to an optical fiber of core diameter 400 μm . For a 60X objective having a numerical aperture of 1.25, and 488 nm excitation laser wavelength, the theoretical lateral and axial resolution of the microscope can be calculated as 238 nm and 648 nm respectively, close to experimentally measured values.

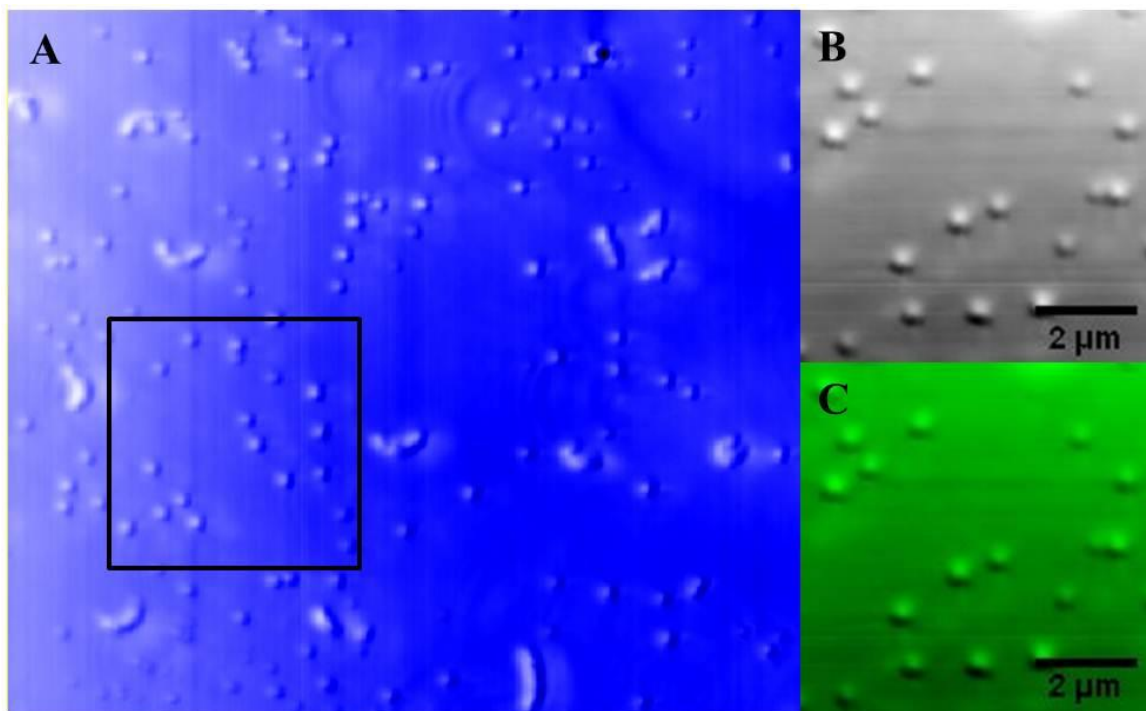


Figure 2.6: (A) LabVIEW raw image of polystyrene beads having a mean size of 100 nm acquired with CLSM. Selected squared shaped area shown in raw image is processed with ImageJ with gray (B) and green (C) filter.

2.5.3. Optical Sectioning Capability

Sectioning of standard microparticles is done with 5 μm silica gel beads and pollen grains. Different Z-sections of the dye doped silica beads are taken. Figure. 2.7 shows the fluorescence image of 5 μm size fluorescent dye labeled silica microparticles.

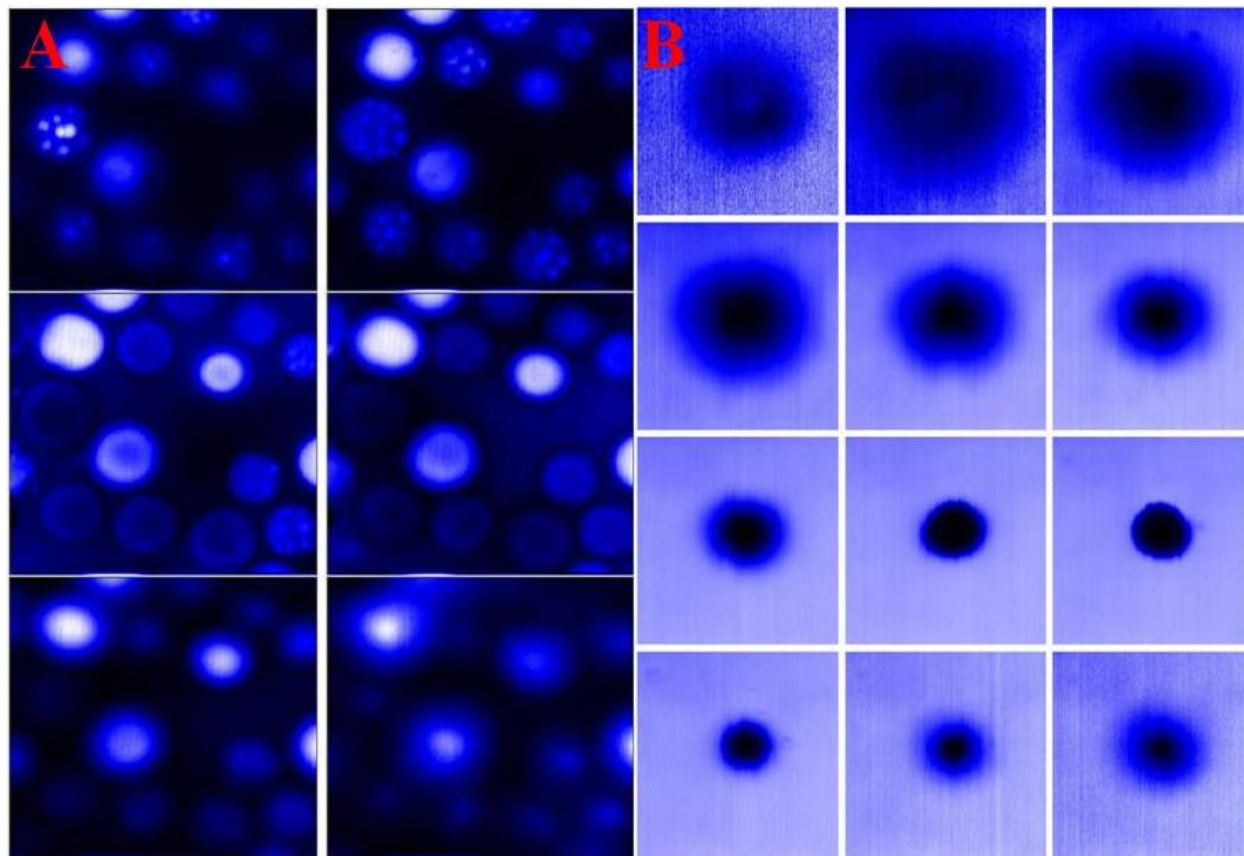


Figure 2.7: (A) Six 2-D sections of the 5 μm silica gel bead sample, showing slices at the lower, middle and upper half of the bead. (B) Optical Z-sections of a single 5 μm silica gel bead showing sections from top to bottom.

Different Z-sections of the pollen grains are taken using CLSM. Optical sections are gathered in approximately 2 μm steps perpendicular to the Z-axis by moving the objective manually using the axial fine motion knob of the microscope. Figure 2.8 (A) shows ten axial cross sections of pollen grains. The weak constant background mostly arises from electronic noise and background illumination. Figure 2.8 (B) shows the 3D reconstruction of the sample pollen grain constructed from these optical cross sections using ImageJ software (Schneider *et al.*, 2012). These images are acquired using 488 nm wavelength line of an argon ion laser. The laser power at the objective focus plane is 50 kWcm^{-2} . Scan frequencies of 25 Hz and 0.05 Hz respectively are used for the X and Y scan mirrors, providing a pixel dwell time of 80 μs .

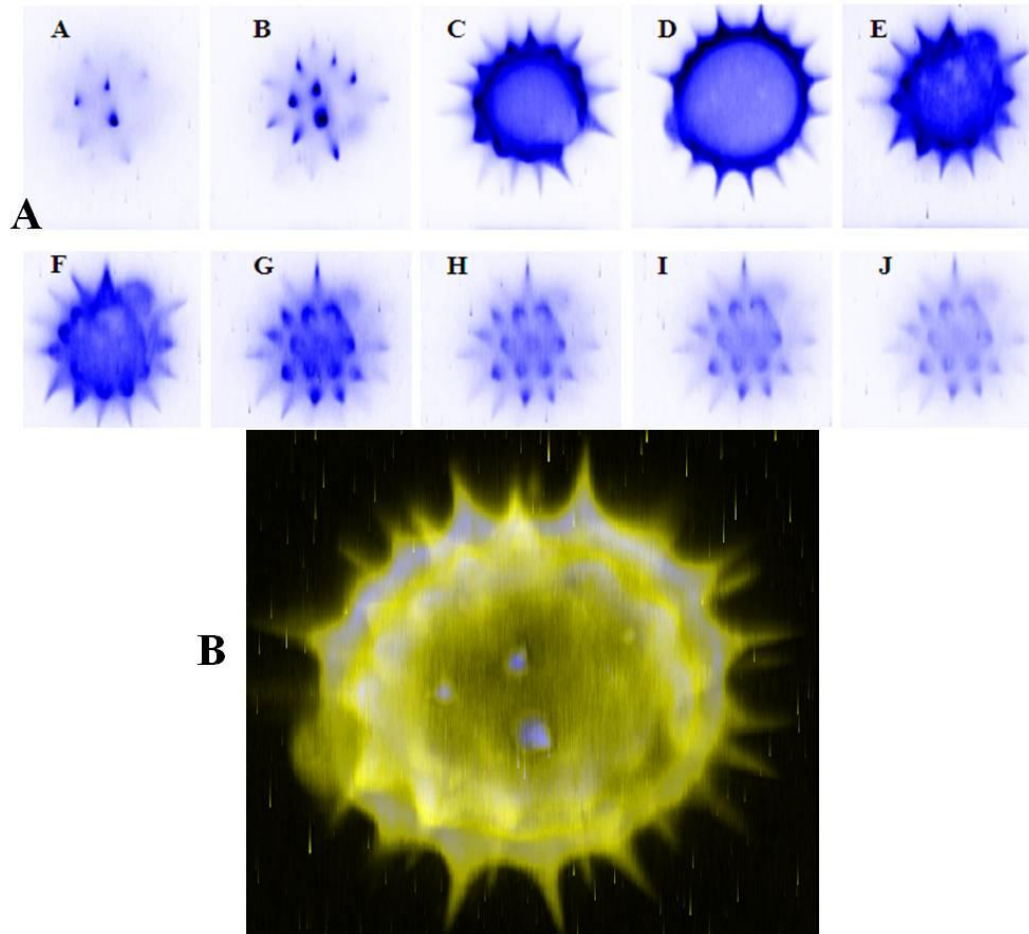


Figure 2.8: (A) Cross sectional images of a dye labeled pollen grain shows the optical sectioning capability of CLSM. Figures A-J shows ten confocal cross-sections of dye labeled pollen grain from top to bottom view. (B) 3D reconstruction of the pollen grain serial optical sections.

2.5.4. Fluocell Test Slide

FluoCells prepared microscope slide contain multi-labeled Muntjac skin fibroblast cells preparations for observation by fluorescence microscopy. The prominent filamentous actin in these cells is labeled with Alexa Fluor 488 phalloidin. Confocal image taken by the CLSM set up with Argon ion laser beam with 488 nm excitation beam is given in figure 2.9. Figure 2.9 A and C show original LabVIEW images without any processing while figures 2.9 B and 2.9 D show the images processed with ImageJ software using a green filter. Fluocell images acquired with 60X objective shows the actin filaments clearly as well distinguished lines and exhibiting the capability of our CLSM.

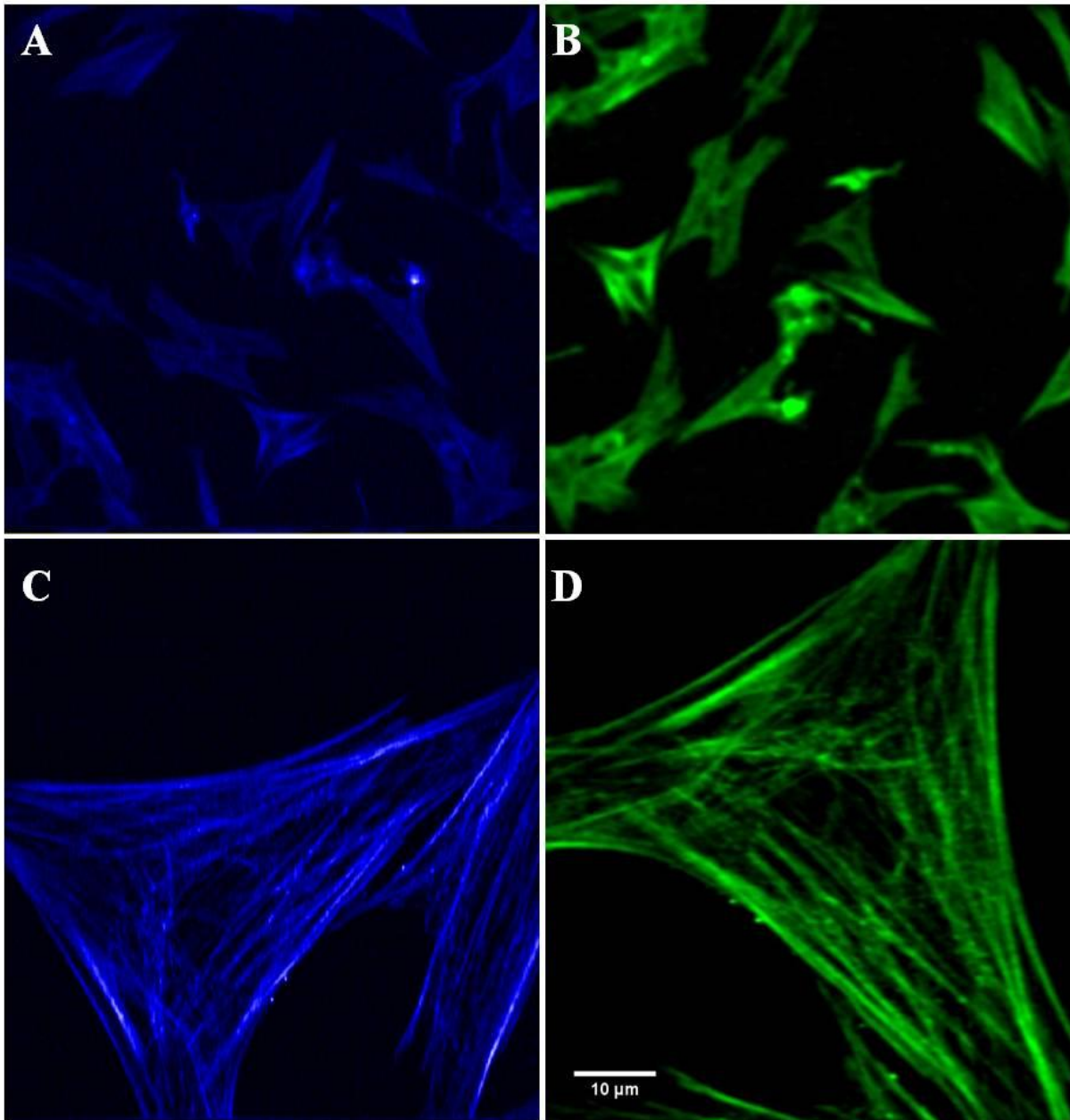


Figure 2.9: Confocal image of actin filaments in FluoCells prepared slide contains Muntjac skin fibroblast cells stained with an Alexa Fluor 488 phalloidin. First two images (A and B) are acquired with 10X objective and the next two images (C and D) are acquired with 60X objective.

In summary we have successfully implemented a CLSM using an Olympus IX-71 microscope and an X-Y scan mirror system and standardized the confocal microscope using different standard microparticles and biological samples. Our home-build CLSM set up is stable and delivering reproducible intensity measurements with good image quality.

CHAPTER THREE

TIME LAPSE CONFOCAL FLUORESCENCE IMAGING OF NUCLEAR TRANSPORT

3.1. INTRODUCTION

Confocal optical fluorescence microscopy records the fluorescence from a specific axial volume of interest and thus can be used to selectively study a particular constituent or section of an appropriately labeled cell nucleus. In time lapse confocal fluorescence imaging one monitors a cross sectional area of interest as a function of time. The technique can be used to study the temporal evolution of a microscopic system (Villalta *et al.*, 2011, Kreft *et al.*, 2005). Time lapse confocal microscopy has been extensively used in cell biology to observe artificially cultured/*in vitro* cells (Gfrerer *et al.*, 2013, Attik *et al.*, 2013, Li *et al.*, 2011, Megason, 2009, Nowotschin *et al.*, 2010). The time lapse imaging scheme has also been successfully employed to monitor cell behavior and molecular movements in living cells by many groups. Such studies on the rates of transport of biomolecules through biological membranes can be used to estimate the permeability of nuclear membranes (Mohr *et al.*, 2009, Peters, 1983b, Peters, 1983a, Ribbeck & Gorlich, 2001).

In the present work we have employed times lapse confocal fluorescence imaging to study the transport of dye labeled dextran molecules of different sizes through the nuclear pore complexes. Experiments are carried out in digitonin permeabilized cells under transient conditions. In this chapter we give the methodology employed in these measurements and discuss time lapse imaging scheme by presenting cross sectional images of two standard nuclei, the HeLa cell nucleus and A549 cell nucleus, after the addition of dye labeled dextran molecules in the cytoplasm. Detailed introductory background is given on cell culture handling, growth and maintenance during different stages of cell growth and digitonin permeabilization. Images of the equatorial plane of the nucleus at different times after the addition of dye labeled prototype dextran molecules are presented. Methods employed in the analysis of this data, and determination of the rate constants of nuclear import is discussed in detail.

3.2. MATERIALS

3.2.1. Adherent Cell Lines

Two types of adherent cell lines are used in the studies reported here. These cell lines, A-549 and HeLa, are obtained from Cell Repository division of National Centre for Cell Science (NCCS), Pune, India.

A549 cells are adenocarcinomic human alveolar basal epithelial cell lines. This cell line is a suitable transfection host. The A549 cell line is first developed through the removal and culturing of tumorous lung tissue in the explanted tumor. In nature, these cells are responsible for the diffusion of some substances, such as water and electrolytes, across the alveoli of lungs. If A549 cells are cultured *in vitro*, they grow as monolayer cells, adherent or attaching to the culture flask (Stephanova *et al.*, 2008).

A **HeLa cell** is an immortal cell line widely used in scientific investigation. It is the oldest and most commonly used human cell line. The cell line is derived from cervical cancer cells. We obtained this HeLa cells with earlier passage number from NCCS. HeLa cells have been used for research on cancer, AIDS, the effects of radiation and toxic substances, gene mapping, and in many other scientific pursuits (Bruni *et al.*, 1961).

3.2.2. Cell Culture Materials

Dulbecco's Modified Eagle Medium

Dulbecco's Modified Eagle Medium (DMEM) with 4.5 grams glucose per litre, sodium pyruvate and sodium bicarbonate without L-Glutamine obtained from HiMedia Laboratories (Product Code: AL007) is used in cell culture experiments as liquid cell culture medium. DMEM is one of the most commonly used modifications of Basal Medium Eagle (BME) that contains four-fold concentration of amino acids and vitamins. The original formulation contains 1000 mg/L of glucose and is originally used to culture embryonic mouse cells (Zhang *et al.*, 2006).

Fetal Bovine Serum

Fetal bovine serum (FBS) is a universally used important supplement in cell culture growth media. Heat inactivated FBS (Product Code: RM9955) is a mixture of proteins, vitamins, hormones, lipids, carbohydrates, minerals growth factors and trace elements and is used as a common growth supplement effective for most types of human and animal cells (Witzeneder *et al.*, 2013).

Antibiotic Antimycotic Solution

Antibiotic Antimycotic Solution 100X (Product Code: A002) is a mixture of Penicillin, streptomycin and amphotericinB. Penicillin and streptomycin are broad spectrum bacteriostatic and bactericidal agents effective against Gram positive and Gram negative bacteria. AmphotericinB is an antifungal agent effective against fungi and yeasts. Penicillin acts by inhibiting cell wall synthesis in bacteria. Streptomycin blocks the initiation complex of protein synthesis.

Complete Growth Medium

Most cell culture media are sold as basal media. Basal medium is a complex mixture of salts, vitamins, carbohydrates, metabolic precursors, amino acids and trace elements. To enhance cell growth, you must add growth factors, hormones, and other proteins to the basal medium. Often this is accomplished by supplementing the basal medium with serum. We used complete growth medium for the growth of adherent cell lines which contains 90% DMEM with 10% FBS and little amount of antibiotic antimycotic solution. We normally prepare complete medium in 50 mL falcon tubes and use within two week of preparation.

Freezing Medium

Composition of freezing media depends on cell type. Standard freezing media contains 90% Media and 10% DMSO. We generally use 90% cold FBS and 10% DMSO in freezing media to preserve the cells. High concentration of serum will help in storing the cells at -80°C for long duration.

Trypan Blue

Trypan blue is usually used in microscopy for cell counting. Trypan blue is a diazo dye used to selectively stain dead tissues or cells blue. 0.4% Trypan blue solution in Dulbecco's phosphate buffered saline (TCL046, Himedia Laboratories) is routinely used for analyzing live cells during trypsinization procedure in cell culture.

PBS Buffer

Phosphate Buffered Saline (PBS) is a common buffer widely used in molecular biology and tissue culture as dilution and wash buffer as it is isotonic and nontoxic to living cells. PBS is water based salt solution containing Sodium phosphate, Sodium chloride and Potassium phosphate. 10X PBS, pH 7.4 is a concentrated form and has to be diluted to 1X concentration (using nuclease free sterile water) before usage. 10X PBS is prepared with 10 mM Disodium hydrogen phosphate, 137 mM Sodium chloride, 2 mM Potassium dihydrogen phosphate and the pH is adjusted to 7.4. This solution is extensively used for dilution and washing during various biological applications as it maintains the physiological pH and osmolarity. The phosphate groups of this buffer help to maintain a constant pH.

Trypsin

Trypsin is a serine protease derived from porcine pancreas. It is generally used for disaggregation and dissociation of adherent cells. Product TCL006 (HiMedia Laboratories) is 0.25% Trypsin in Dulbecco's phosphate buffered saline. Time required for detachment of cells from surface depends on cell density, cell type, potency of trypsin, serum concentration in growth medium and time since last subculture. We usually incubate cells with 0.25% trypsin solution for 5 min at 37°C for trypsinization procedure.

Tissue Culture Vessels

Plastic wares used in growing cell culture are obtained from Tarsons Product Pvt. Ltd. We used 25 cm² NEST tissue culture flask with filter cap-sterile (Product code: 950040), 75 cm² tissue culture flask (Product code: 950020) and 35 mm diameter NEST tissue culture petri dish-sterile

(Product code: 960010) for growing cells. All these flasks and plates can be used for growing adherent cell cultures.

Heamocytometer

For cell culture and many other biological applications that require use of suspensions of cells it is necessary to determine cell concentration. We used a cell counting device heamocytometer (Model: BS 748, Rohem Instruments Pvt. Ltd.) to count cells. It is a thick glass microscope slide with a rectangular groove that creates a chamber. This chamber is engraved with a laser-etched grid of perpendicular lines. The device is carefully crafted so that the area bounded by the lines is known, and the depth of the chamber is also known. It is therefore possible to count the number of cells or particles in a specific volume of fluid, and thereby estimate the concentration of cells in the fluid overall.

3.2.3. Reagents Used in Nuclear Transport Studies

Digitonin

Digitonin is a glycoside used as a detergent; it effectively water-solubilizes lipids in membranes. As such, it has several membrane related applications in biochemistry, precipitating cholesterol, including solubilizing membrane proteins and permeabilizing cell membranes. This mild nonionic detergent can be used to solubilize receptors and permeabilize cellular and nuclear membranes. We have used digitonin (HiMedia Laboratories, Product Code: RM807) prepared in transport buffer for nuclear transport studies.

Rabbit Reticulocyte Lysate

Rabbit Reticulocyte Lysate (RRL) is obtained from Sigma Aldrich (Product no: R-1378). Reticulocyte is an immature red blood cell. Lysate is a solution that is formed when a cells membrane is ruptured *in vitro*. RRL is prepared from white rabbits using a standard protocol that ensures reliable and consistent reticulocyte production. The reticulocytes are purified to eliminate contaminating cells, which could otherwise alter the translational properties of the final extract. The lysate contains the cellular components essential for protein synthesis (tRNA, amino acids, ribosomes and initiation, elongation and termination factors).

FITC Labeled Dextrans

Dextran is a polymer of anhydro-glucose. It is composed of about 95% alpha-D-(166) linkages. The remaining (163) linkages account for the branching of dextran. FITC is conjugated randomly to hydroxyl groups of dextran at a frequency of 0.003 to 0.02 moles of FITC per mole of glucose. The excitation maximum of FITC-dextran is at 490 nm. The emission maximum is at 520 nm. The fluorescence emission from the dye increases with pH and is optimal at pH 8 and above. Various MW of dextrans are produced by limited hydrolysis and fractionation. Fractionation is accomplished by size exclusion chromatography or ethanol fractionation, where the largest MW dextrans precipitate first. The FITC conjugation with hydroxyl groups of dextran is carried out in DMSO. Stored properly at 2 – 8°C and protected from light FITC-dextran powders should be stable for a minimum of three years. FITC-dextran is used extensively in microcirculation and cell permeability research utilizing microfluorimetry. FITC labeled dextrans of average molecular weights 4 kDa (model-FD4S), 10 kDa (FD10S), 20 kDa (FD20S), 40 kDa (FD40S), 70 kDa (FD70S) and 150 kDa (FD150S) are obtained from Sigma Aldrich Chemicals Pvt. Ltd.

3.2.4. Major Instruments Used

Following instruments are used in growing and maintaining cell lines.

CO₂ incubator: Sanyo, MCO-18AIC Model CO₂ Incubator

Laminar flow hood: Imset 2 ft × 2 ft × 2 ft Laminar air flow chamber

Spectrophotometer: Shimadzu UV2450

PCR machine: Biorad MJMini thermal cycler

Gel Doc apparatus: Biorad Gel Doc XR

DNA electrophoresis: Genei Submarine electrophoresis system

Deep freezer (-80 C): New Brunswick Scientific

Microscopes: Olympus IX-71 Inverted Microscope, Nikon Eclipse TS100 inverted fluorescent microscope and Olympus BX-41 Phase contrast Microscope.

3.3. EXPERIMENTAL METHODS

3.3.1. Adherent Cell Line Culture

Cultures are obtained as growing cell cultures in T-flasks from NCCS, Pune. The procedure for handling the cultures aseptically under sterile conditions upon receipt is taken care. The flask is seeded and entirely filled with transport medium to avoid loss of cell viability in transit. Upon receipt most of the medium is removed except for a sufficient volume to cover the floor of the flask (5 – 10 mL). The cells are augmented with serum to the necessary level of supplementation (0.5 – 1.0 mL of FBS) and incubated at 37°C until confluency is reached.

Adherent cell lines are cultured in Dulbecco's Modified Eagles Medium complemented with 10% fetal bovine serum. Antibiotics are not routinely used for tissue culture unless cryptic contamination is suspected. Eradication of suspected contamination is only carried out if the cell line is irreplaceable and involved a two week culture period in antimetabolic and antibiotic solution. When cells became more than 70% confluent, or every three days (whichever is earlier) cultures are passaged (split). Medium from flasks/plates is carefully poured into suitable disinfectant. Each 75 cm² (T-75) flask is washed 2 times with 2 – 3 mL of pre-warmed PBS (Phosphate Buffered Saline) and then incubated for 5 minutes at 37°C with 2 mL of 0.25 % Trypsin-EDTA solution. After this incubation time, cultures are vigorously agitated. Cells normally separate from the flask/plate easily after this time. If cells did not separate from the culture dish, a longer incubation or using high concentrated Trypsin-EDTA is sometimes necessary. The supernatant containing the cells is then centrifuged at 2000 rpm for 5 minutes in a 15 mL falcon centrifuge tube. The resulting pellet is resuspended in 10 mL pre-warmed complete growth medium. The cell density of this mixture is established using a haemocytometer and cells reseeded into new plates at an appropriate density. Trypan blue is used to determine live cell number once a week. This involved mixing an equal volume of trypan blue stain and cell suspension. Cells are then counted using a haemocytometer; strongly stained cells are considered to be dead or dying.

Frozen cell stocks are produced every month. T-75 flask of cells are trypsinised as mentioned above, collected, centrifuged at 2000 rpm for 5 minutes and the pellet resuspended in 1mL of 90% FBS and 10% di-methyl sulphoxide (DMSO) and placed in cryo vials. These tubes are placed at -20°C overnight in polystyrene containers to slow the freezing process. The morning after, cells are moved to storage in -80°C freezer or liquid nitrogen container.

When counting cells for seeding experiments, a haemocytometer is used. Cells are diluted with an equal volume of trypan blue. Cells which are healthy excluded the dye from their membranes. Unhealthy or dead cells appeared blue under microscopy and are not counted. If large numbers of dead cells are seen in a culture, it is discarded. Tissue culture microscopy is performed using an Olympus IX-71 inverted microscope. The aperture is 10 or 60 X with total final magnification 100 – 600 X. Images are taken using a Samsung Camera (Model: SDC-313B) and software.

3.3.2. Cell Doubling Time Measurement

Cell doubling time is measured by seeding 1×10^5 cells in 1 mL of appropriate medium in tissue culture plate and culturing for 24 hours. After this time, the number of cells in the well is estimated using a haemocytometer. The cell doubling time in days is calculated according to the formula

$$\text{Doubling time (days)} = \log_{10} 2 / [\log_{10} (a) - \log_{10} (b)]$$

Where a = number of cells after 24 hours and $b = 1 \times 10^5$

This process is performed in triplicate and repeated to allow the cell doubling time to be calculated over the course of the experiment.

3.3.3. Imaging Chamber Preparation

Preparation of cleaned coverslips and growth chambers or imaging chambers is vital for healthy cell cultures. 22×22 mm glass coverslips is first kept overnight in concentrated nitric acid in a glass jar. Then the coverslips are removed from nitric acid and washed extensively (5 – 7 times) in deionized water. Washed coverslips are dried in a laminar flow hood and sterilized with UV light for 30 minutes. Sterilized coverslips are placed into sterile petri dishes for storage.

Imaging chambers are built by drilling a 6 mm hole in the bottom of 35 mm petri dishes and attaching the clean coverslips with a combination of paraffin and petroleum jelly in the ratio of 3:1 (Kapon *et al.*, 2010). Petri dishes are placed upside down on a big glass petri dish and heated at 80°C in an oven for around 10 minutes or until paraffin mixture is melted. Then the dishes are transferred onto a uniform surface and the paraffin mixture is allowed to set at room temperature. Dishes are turned over and sterilized with UV light. We regularly use cleaned coverslips within a week of preparation.

3.3.4. Transport Buffer

The transport buffer used in this study contains 20 mM Hepes; 2 mM magnesium acetate; 5 mM sodium acetate; 110 mM potassium acetate; 1 mM Methylene glycol-bis (β -aminoethyl ether)-N,N,N,N,-tetraacetic acid; 2 mM dithiothreitol (DTT) and protease inhibitors (aprotinin, pepstatin, leupeptin; each at 1 μ g/mL), pH adjusted to 7.3 with sodium hydroxide. First 10X transport buffer salt solution that lacks DTT and protease inhibitors is made and sterilized by filtration and stored at 4°C. Fresh 1X transport buffer is prepared from this 10X salt solution with sterile distilled water, DTT and protease inhibitors.

3.3.5. FITC-Dextran Preparation

FITC labeled dextrans of average molecular weights 4 kDa, 10 kDa, 20 kDa, 40 kDa and 70 kDa (Sigma Aldrich) are dissolved in sterile distilled water at a final stock concentration of 25 μ M. FITC-dextran stock solutions are further diluted with 1X transport buffer (TB), pH 7.3 [20 mM Hepes; 110 mM potassium acetate; 2 mM magnesium acetate; 5 mM sodium acetate; 1 mM EGTA; pH adjusted to 7.3 with sodium hydroxide and 2 mM DTT and protease inhibitors (aprotinin, leupeptin, pepstatin; each at 1 μ g/mL) added immediately before use] and dialyzed RRL to the final concentration of 1 μ M.

3.3.6. Digitonin Permeabilization

In this work the nucleocytoplasmic transport of fluorescently labeled biomolecules are studied using a digitonin permeabilized cell system. For permeabilizing the cell membranes the following protocol is used. Stock solution of 40 mg/mL of digitonin is prepared by dissolving in DMSO. Stock solution is then aliquoted to 2 μ L in sterile micro centrifuge tubes and stored in

freezer (-20°C). Working concentration is prepared freshly by adding 1X Transport buffer with 40 mg/mL digitonin-DMSO stock. The plasma membrane must be permeated to allow entry of cell-impermeable fluorescent probes. Digitonin can preferentially permeabilize the plasma membrane of mammalian culture cells while leaving the nuclear membrane intact. In this study, we checked the permeability with six different concentration of digitonin detergent (10, 20, 30, 40, 50 and 60 $\mu\text{g}/\text{mL}$). The optimized concentration for digitonin permeabilization is determined by checking the entry of control molecule through the nuclear membrane. 70 kDa FITC labeled dextran is used as a control molecule during this digitonin permeabilization experiment.

3.3.7. Dialysis of Rabbit Reticulocyte Lysate

Nuclear transport in digitonin permeabilized cells is assayed in the presence of a rabbit reticulocyte lysate. RRL is used as exogenous cytosol in the transport studies, and before use it is dialyzed against transport buffer (1X) using a membrane (25,000 MW cut-off). RRL is dissolved in 1 mL of 64 mM potassium chloride (KCl) and 25 μM Hemin. Two liter of fresh 1X transport buffer is prepared from 10X stock for dialysis experiment. Dialysis apparatus is set up in cold room (4°C) with magnetic stirrer. The membrane is tightened with dialysis clips and processed with distilled water and buffer before the experiment. Buffer is changed three times and kept for overnight in cold room. Dialysis allowed fast and effective buffer exchange with $\sim 20\%$ dilution of the extract. Final volume derives around 1.5 mL. Dialyzed extract is then aliquoted in sterile micro centrifuge tubes and stored in refrigerator (4°C). In a typical nuclear import assay, cytosol accounted for 50% of a 25 μL reaction volume. We have used Nanodrop lite spectrophotometer to measure the protein concentration in the dialyzed RRL extract.

3.3.8. Import Mixture Preparation

Import mixture contains desired concentration of molecules needed to be transported into nucleus along with the transport buffer components and with or without RRL. Import mixture is prepared freshly before the nuclear transport experiments. Usually the final import mixture will have the transport molecule with 1X transport buffer and 50% RRL. All the components in the import mixtures are mixed properly with the use of cyclo mixers and then stored properly in dark containers.

3.3.9. Nuclear Transport Studies

Growth of adherent cell cultures in petridishes is carried out and the procedure is optimized. For the nuclear transport studies cells are permeabilized with digitonin. Flow chart of nuclear transport experiment procedure is given in figure 3.1.

Protocol used for the Nuclear Transport experiments

First Day

1. Approximately ~ 20,000 cells are added to the coverslip sealed with petri dish with a hole of 6 mm in the centre.
2. Allowed to grow for 18 – 24 hours.

Second Day

3. Preparation of fresh 1X transport buffer and digitonin solution.
4. Complete medium is changed two hours before the experiment and fresh medium added.
5. Cells are washed with Transport buffer.
6. Cells are permeabilized with 25 μ L of optimized concentration of digitonin for 5 minutes at room temperature.
7. Then the cells washed three times with 1X TB to remove excess digitonin.
8. Import mixture is then added into the culture plate, keeping the equatorial plane of the cells in the focus of the confocal laser scanning microscope.

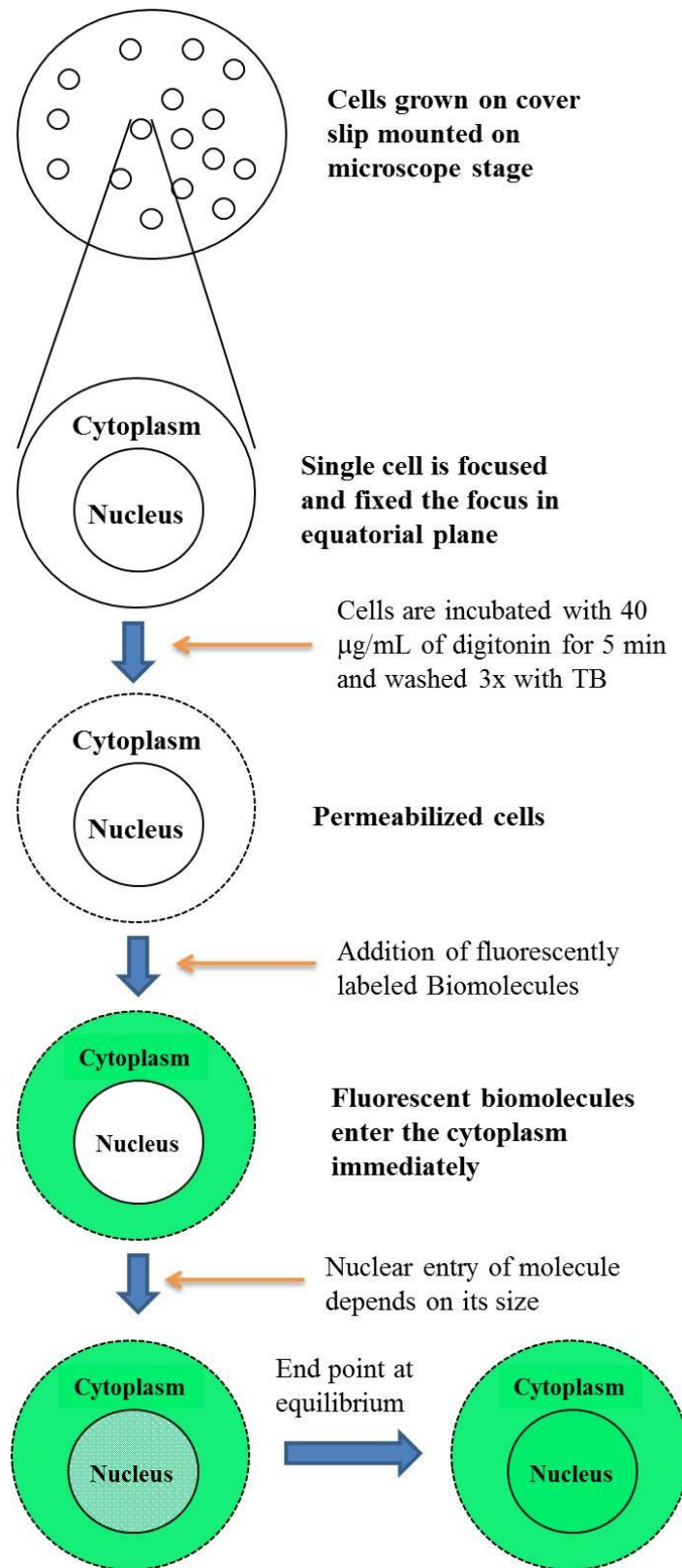


Figure 3.1: Flow chart of nuclear transport experiment procedure.

3.3.10. Confocal Imaging of Nuclear Transport

Diffusion of FITC-labeled dextran molecules from cytoplasm to the nucleus is studied using a home built confocal fluorescence microscope. The details of the design and construction of the confocal laser scanning microscope is as described in chapter 2. In the time lapse imaging of nuclear transport we have employed lock in detection of the fluorescence signal so as to improve the signal to noise ratio and thus image quality. Briefly, the excitation laser beam (Argon ion laser, 488 nm wavelength) is passed through an acousto-optic modulator (Isomet, 1205C-1) and directed to the scanning mirrors by a dichroic mirror as per the layout given in figure 3.2. The modulated laser beam reflects off the two scan mirrors and is focused to the conjugate plane of the microscope by the scan lens. The emitted fluorescence returns along the same pathway, and is de-scanned by the mirrors and transmitted to the photo detector through the dichroic mirror. Emitted fluorescence is collected using a 510 – 590 nm band pass filter and a silicon photomultiplier tube (SensL, MiniSM). The signal from the receiver is sent to a 200 MHz dual phase lock in amplifier (Stanford Research Systems Inc., SR-844) to discern the laser induced variation in the scattered beam. Data acquisition card (National Instruments Corporation, USA, NI-USB-6251) controls the optical scanners and also acquires data from the detector using the computer. Images of 250×250 pixels are acquired using a custom made LabVIEW imaging and data acquisition program. Scan frequencies of 100 Hz and 0.4 Hz, respectively are used for the X and Y scan mirrors. Studies are carried out in the time lapse imaging scheme. Argon ion laser power at the objective focus is 2 kW/cm^2 . The diffusion of biomolecules into the nucleus is quantified by estimating the fluorescence intensity at the equatorial plane.

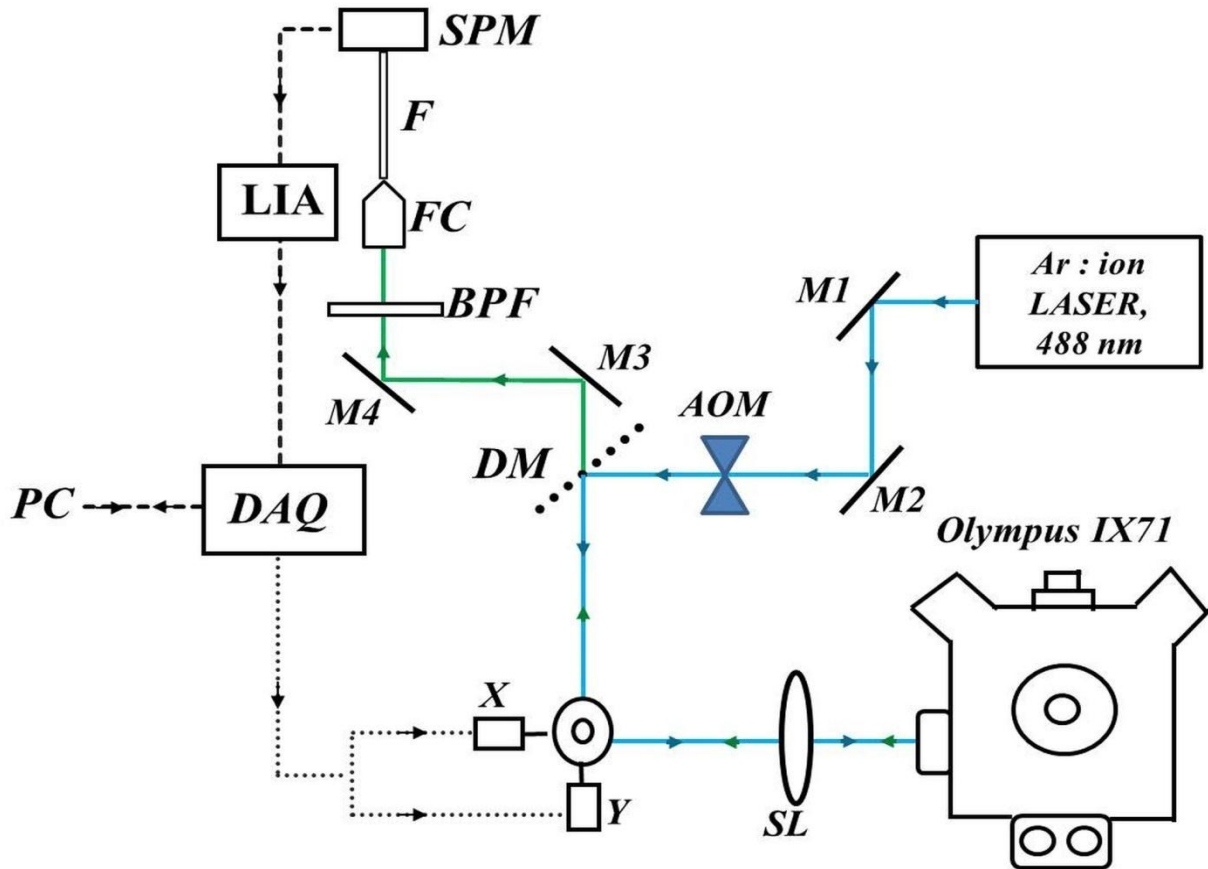


Figure 3.2: Experimental layout of the confocal laser scanning microscope used in time lapse imaging of nuclear transport. SL – Scan Lens, X and Y – Scanning mirrors, DM – Dichroic Mirror, FC – Fiber Coupler, F – Optical Fiber, BPF – Band Pass Filter, SPM – Silicon photomultiplier, M1-M4 – Mirrors, AOM – Acousto Optic Modulator, LIA – Lock in Amplifier, DAQ – Data Acquisition Card and PC – Computer.

3.3.11. Model of Nuclear Transport Kinetics

The nuclear import through the NPCs can be modeled by considering a two-compartment arrangement consisting of a cytoplasm and nucleus. These compartments are separated by a thin membrane, the nuclear membrane having discrete transporters, the NPCs (Kiskin *et al.*, 2003). The biomolecule or transport substrate is assumed to be instantaneously added to the cell cytoplasm at zero time. The cytoplasm is permeabilized and has a leaky membrane so that the transport substrate concentration in the cytoplasm (C_C) is constant. The nucleus is small compared to the cytoplasm that the transport substrate is quickly dissipated to the nucleus by

diffusion. Thus the intra-nuclear concentration (C_N) of the transport substrate is a function of time only. For a purely passive, diffusional nuclear membrane transport process the transport molecule is not absorbed or produced anywhere in the system and its equilibration across the nuclear membrane is very fast. Under these conditions the flux of substrate per unit membrane area ($\text{mol}/\mu\text{m}^2/\text{s}$) is quasi-stationary at any time and can be expressed as:

$$\phi(t) = P [C_C - C_N(t)] \quad (3.1)$$

Where P is the permeability coefficient ($\mu\text{m}/\text{s}$). The total flux through a nuclear envelope is the sum of the unitary fluxes through individual nuclear pore complexes, each having the average single transporter permeability P_{NPC} ($\mu\text{m}^3/\text{s}$). For a membrane patch of surface area S containing a large number n of NPCs at an average density σ ($\text{NPC}/\mu\text{m}^2$)

$$P = n P_{NPC}/S = \sigma P_{NPC} \quad (3.2)$$

For a constant concentration difference ΔC across the membrane (e.g., 1 μM), the flux and permeability described by equation. 3.1 can be linked to the permeability and expressed using Avogadro's number N_A as a unitary flux (molecules/s/NPC)

$$\phi_{NPC} = P_{NPC} N_A \Delta C = P N_A \Delta C / \sigma \quad (3.3)$$

The mean time of biomolecular substrate diffusion inside the nucleus is proportional to $(\text{Nucleus dimension})^2/D$ where D is the diffusion constant of the substrate. The nucleus can be considered as being well homogenized and the concentration C_N is a function of time only. Suppose the cytoplasm and nucleus have volumes V_C and V_N , respectively and that the membrane covering the nucleus have surface area S . Then the kinetics of substrate accumulation in the nucleus due to the flux through the membrane patch is given by

$$\frac{dC_N(t)}{dt} + P S \frac{V_C + V_N}{V_C V_N} C_N(t) = \frac{P S M(t)}{V_C V_N} \quad (3.4)$$

Where $M(t) = V_C C_C(t) + V_N C_N(t)$ is the total amount of transport molecule. In the typical cell the volume of the cytoplasm is large ($V_C > V_N$) and the amount of substrate in the nucleus is negligible, so that equation 3.4 simplifies to

$$\frac{dC_N(t)}{dt} = \frac{PS}{V_N} [C_C(t) - C_N(t)] = k [C_C(t) - C_N(t)] \quad (3.5)$$

The rate constant k is given by

$$k = \frac{PS}{V_N} = \frac{n P_{NPC}}{V_N} \quad (3.6)$$

For a constant concentration of the substrate in the cytoplasm $C_C(t) = C_{max}$ the solution of Equation. 3.5 is

$$C_N(t) = C_{max}[1 - \exp(-kt)] \quad (3.7)$$

3.3.12. Estimation of Rate of Nuclear Transport

Assuming that the fluorescence signal $F(t)$ is measured in the microscope under constant experimental conditions and that it is proportional to number of fluorescently tagged dextran molecules, the normalized nuclear fluorescence $F(t)$ can be well fitted by a first order kinetic function of the following form from equation 3.7.

$$F(t) = F_{max} (1 - e^{-kt}) \quad (3.8)$$

Normalized nuclear fluorescence $F(t)$ is determined by taking ratio of average fluorescence signal from the nucleus to that of the cytoplasm measured under constant experimental conditions. The plot of $F(t)$ versus time after addition and equilibrations of fluorescently labeled biomolecules in the cytoplasm can give the nuclear transport rates k for biomolecules and are determined from the best fit of data. The ratio between average intra-nuclear and extra-nuclear fluorescence is calculated using ImageJ (Schneider *et al.*, 2012).

3.4. RESULTS AND DISCUSSIONS

3.4.1. Cell Growth and Monitoring

For successful implementation of the time lapse imaging scheme to study nuclear import and to infer true transport rates and permeability, it is important to carry out studies on a cell system

containing healthy cells. It is important to ensure that the cells are in the correct stage of growth and that they are not in a dividing stage. For this we monitor the cell growth with the help of an inverted microscope having an objective lens of appropriate magnification. The confluency of the cell is checked using a 4X magnification objective. For proper visualization of cells we used a 20X objective which gives more idea about cell attachment and morphology. Nuclear transport studies after permeabilization are performed using 60X objective.

In figure 3.3 (A) we show the image of HeLa cells imaged using 10X objective of the Inverted Microscope. Figure 3.3 (B) shows the HeLa cells imaged using 60X objective after permeabilizing the cell membrane with 40 $\mu\text{g}/\text{mL}$ of digitonin. Figure 3.4 shows the inverted microscope image of healthy A549 cell image obtained using 10X objective (A), 20X Objective (B) and 60X objective (C). Dividing cells are indicated with arrow mark.

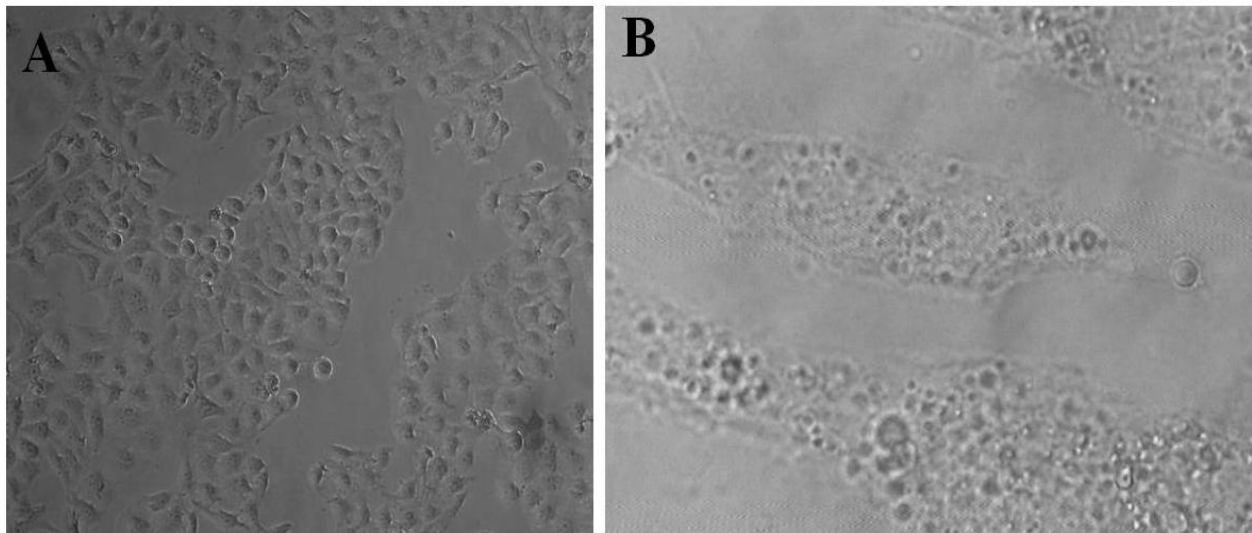


Figure 3.3: (A) HeLa cells grown in a glass bottom petridish imaged using 10X objective. (B) Inverted microscope image of permeabilized HeLa cell imaged with 60X objective.

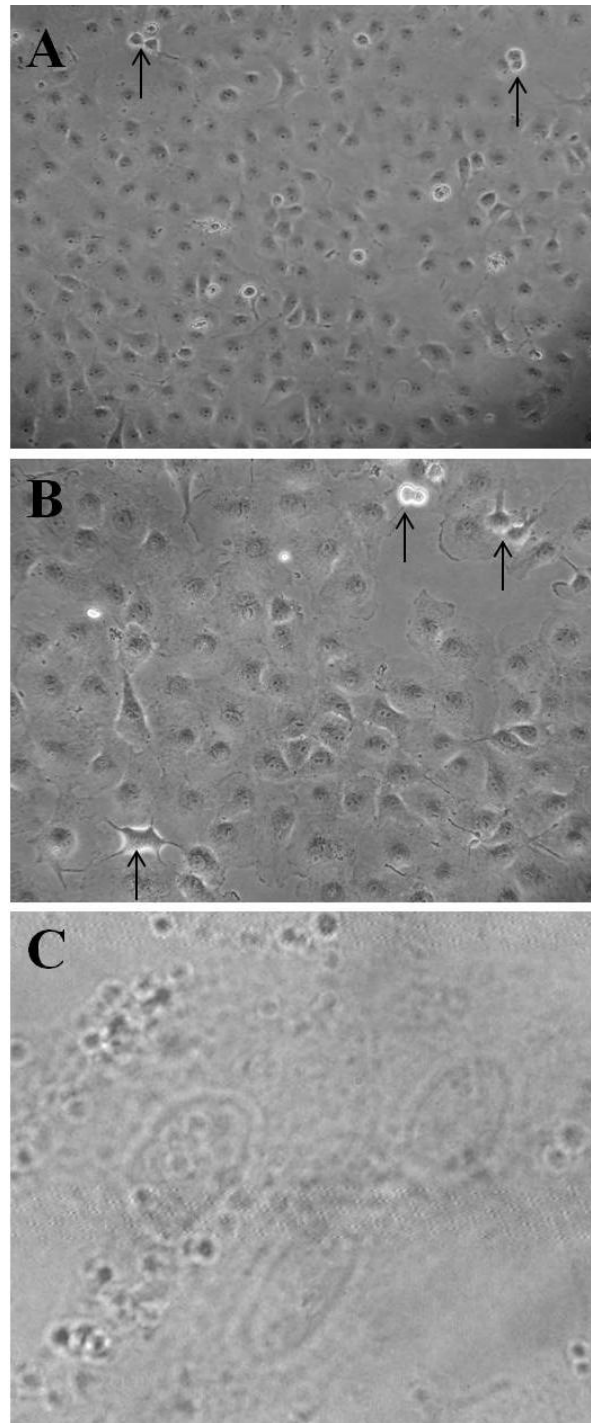


Figure 3.4: Inverted microscope images of A549 cells grown in T25 flask after 24 hours of growth observed with 10X objective (A) and 20X objective (B). Dividing cells are shown with arrow mark. (C) Inverted microscope image of A549 cells grown on glass bottom petridish after permeabilizing with 40 µg/mL of digitonin for 5 minutes.

3.4.2. Digitonin Permeabilization Optimization

After making sure that the cells are healthy and confluent they are permeabilized using digitonin. Permeabilization should be optimized to make the cell membrane permeable without affecting the nuclear membrane. The optimum permeability of the membrane is first confirmed by checking the integrity of the nuclear envelope. In this study, we checked the permeability with six different concentrations of digitonin detergent. Control experiments are carried out with 70 kDa FITC labeled dextrans having a radius of 6 nm. An intact nuclear envelope does not allow the entry of 70 kDa dextran even after permeabilization of cell membrane.

Figure 3.5 shows the image of the cells at 10 minutes after the addition of 70 kDa FITC dextrans to the cells which are permeabilized with digitonin concentrations of 10, 20, 30, 40, 50, 60 $\mu\text{g/mL}$ for 5 minutes respectively. The figure shows that the 70 kDa dextran does not enter the nucleus even after 10 minutes for digitonin concentrations up to 40 $\mu\text{g/mL}$ indicating an intact nucleus. After checking the permeability with 70 kDa, we added 10 kDa dextrans (radius – 2.3 nm) and checked the intensity of fluorescence entry into the nucleus. Figure shows that the 70 kDa dextran readily enters the nucleus for concentrations greater than or equal to 40 $\mu\text{g/mL}$. With lower concentrations of digitonin (10 and 20 $\mu\text{g/mL}$), the cell plasma membranes are not completely permeabilized and allowed very little entry of 10 kDa dextrans into the nucleus. 30 $\mu\text{g/mL}$ of digitonin exhibited permeabilization for many cells but few cells left non-permeabilized and these showed less entry of 10 kDa into cell nucleus. Higher concentrations (50 and 60 $\mu\text{g/mL}$) showed entry of 70 kDa molecule into nucleus and also a detachment in cell lines after washing steps. The optimized concentration for digitonin permeabilization is thus found to be 40 $\mu\text{g/mL}$ for the incubation time of 5 minutes at room temperature. No adverse effect on cell viability is observed when permeabilized with the above concentration of digitonin.

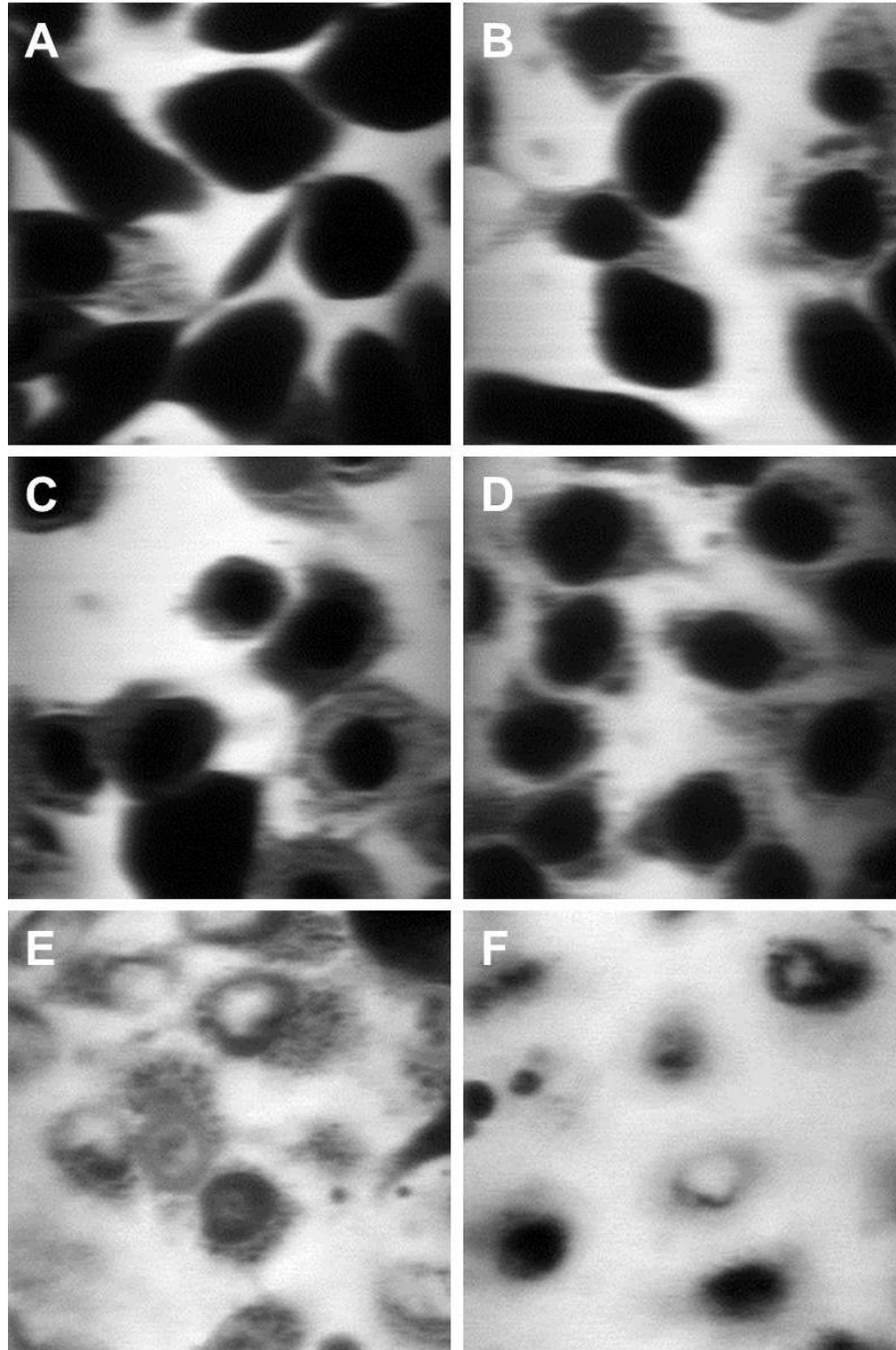


Figure 3.5: Confocal images of A549 cells with 70 kDa FITC labeled dextran molecules added to permeabilized cells which are permeabilized with different concentration of digitonin, 10 $\mu\text{g/mL}$ (A), 20 $\mu\text{g/mL}$ (B), 30 $\mu\text{g/mL}$ (C), 40 $\mu\text{g/mL}$ (D), 50 $\mu\text{g/mL}$ (E), 60 $\mu\text{g/mL}$ (F) for five minutes in room temperature. In A, B and C cell is not properly permeabilized, the cell membrane is intact. In E and F the nuclear membrane as well as the cell membrane is damaged. In D cell membrane is damaged while nuclear membrane is intact.

3.4.3. Confocal Time Lapse Imaging

Transport rates of FITC labeled dextran molecules through A549 cells and HeLa cells nuclear membrane is studied using the in-house constructed confocal laser scanning microscope. Confocal images of permeabilized cells are acquired at fixed intervals after the addition of FITC labeled dextran into the cytoplasm. The intake and intracellular distribution are found to be dependent on the molecular weight of the dextrans. Figure 3.6 shows the time lapse images of the cells at particular time interval after the addition 10 kDa FITC dextrans to the cells which are permeabilized with the 40 $\mu\text{g/mL}$ digitonin concentrations. The images shown are acquired with the voltage of 2 V applied to the scanning mirrors with the imaging area of $87 \mu\text{m} \times 87 \mu\text{m}$.

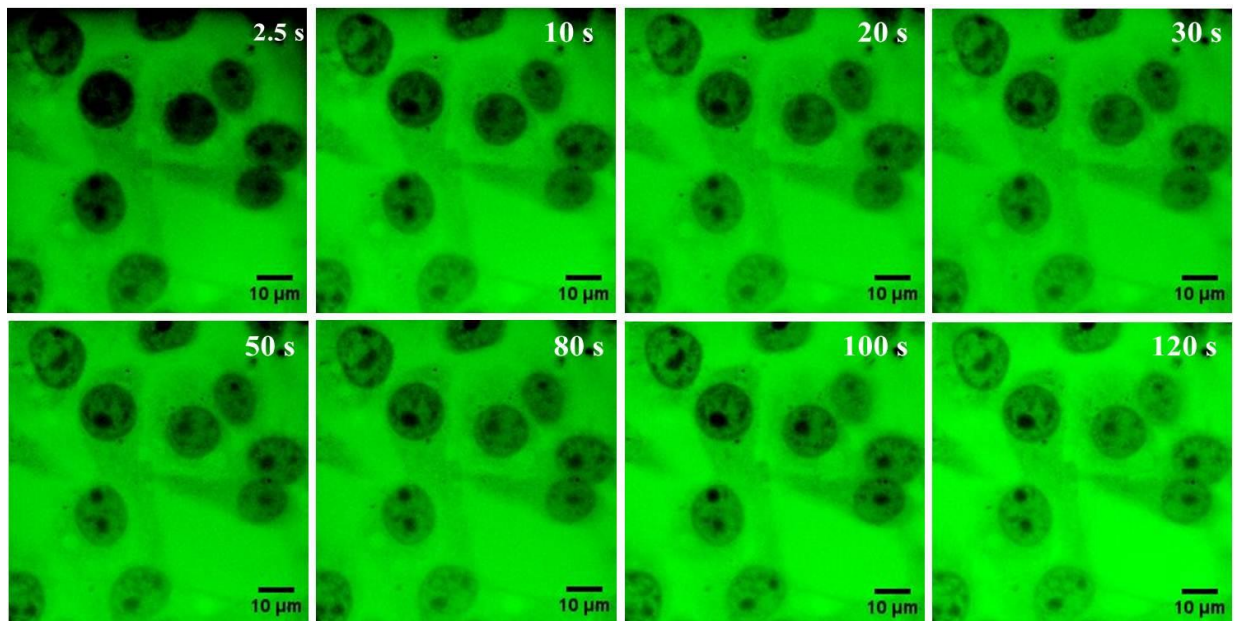


Figure 3.6: Time lapse confocal images of A549 cells after the addition of 10 kDa FITC labeled dextran molecules to digitonin permeabilized cells. At 2.5 s the nuclei appears dark because the no significant amount of dye labeled dextran has entered the nuclei. As time progress the nuclei changes to green indicating entry of dextran molecules.

We studied how the biomolecules are transported into nucleus in cancer cells because these cells proliferate rapidly. These cell lines are suitable transfection host. All the image and data recordings are made directly on the non-fixed samples using time-lapse scheme in confocal laser scanning microscopy. Transport through nuclear membrane pores is measured by analyzing

the intensity values obtained from CLSM images of cell nucleus. The Z position in all pictures is adjusted to the equatorial level of the nuclei. Data and images are acquired using LabVIEW software program. The data are converted to tiff images using the Matlab software program. ImageJ software program is used for the quantification of the stained nuclei from the time lapse stacks of tiff images. The images in figure clearly show an increase in fluorescent intensity with time inside nucleus which indicates the transport of FITC labeled dextran into the nucleus. A control experiment carried out using 70 kDa dextran molecules showed no change in intensity inside the nucleus with time. To further quantify the diffusion of dextran molecules into the nucleus we estimated the fluorescence intensity in the equatorial plane using ImageJ software. Normalized nuclear fluorescence values are calculated by taking the ratio of intensity inside the nucleus and the initial intensity in cytoplasm.

Assuming that the fluorescence signal $F(t)$ measured in the microscope under constant experimental conditions, influx can be well fitted by a first order kinetic function given in equation 3.8. (Naim *et al.*, 2007). Plot of normalized integrated nuclear fluorescence versus time for the nuclear transport of FITC labeled dextran can give the rate of transport using the time course fits to an exponential relation defined in equation 3.8.

The method described in this chapter is not restricted to nuclear transport processes of dextran alone. It may be used, for instance, to analyze translocation of different biomolecules like proteins and nucleic acids across different bio-membranes. We have used this optimized concentration of digitonin for cell permeabilization, nuclear transport procedure and time lapse imaging scheme in the next three chapters.

CHAPTER FOUR

PASSIVE PERMEABILITY AND EFFECTIVE PORE SIZE OF HELA CELL NUCLEAR MEMBRANES

4.1. INTRODUCTION

Nuclear pore complexes in the nuclear envelope act as the sole gateway for the import of nuclear proteins into, and export of RNA and ribosomal sub-particles from the nucleus (Tate & Elborn, 2005, Rout *et al.*, 2000, van der Aa *et al.*, 2006, Katta *et al.*, 2013, Bagley *et al.*, 2000, Adam, 2001). It is believed that there are around 3,000 – 5,000 NPCs in a proliferating human cell. These NPCs allow passive diffusion of small solutes, as well as mediated selective transport of macromolecules in a signal dependent manner called active transport. The mechanism of active translocation through NPC involves interactions between the soluble carriers and proteins present inside the NPC (Wente & Rout, 2010, Strambio-De-Castillia *et al.*, 2010, Schuldt, 2012, Kapon *et al.*, 2010, Conti *et al.*, 1998, Rout *et al.*, 1997). The passive transport takes place through simple diffusion through the concentration gradient and the rate of diffusion will critically depend on the size of the pores.

Nucleocytoplasmic transport is a truly impressive activity: in a growing mammalian cell, more than two million macromolecules per second are exchanged between nucleus and cytoplasm, amounting to a total mass flow of more than 200 GDa (Ribbeck & Gorlich, 2001). In order to understand this amazing molecular activity, it is essential to understand the structure and effective pore size of the NPCs. Though there are microscopic examinations of the NPCs on fixed cells using AFM and TEM (Akey, 1989, Goldberg & Allen, 1993, Ris, 1997, Huang *et al.*, 2010) these studies are not conclusive with regards to live cells. Optical microscopic techniques do not have the resolution to directly visualize the NPC structure, but provide information on cellular activities involving changes in the concentration of proteins, DNA and other cellular components. In particular, confocal fluorescence microscopy, a widely popular imaging technique having three dimensional sectioning capability, can be used to monitor the movement of biomolecules from the cytoplasm to the nucleus. Such studies would not only allow the

estimation of the transport rates of biomolecules but also will provide valuable information on the functioning of NPCs. Also analyzing the transport rates of molecules having different Stokes radius, one may infer the effective pore size of the NPC.

Analysis of molecular transport through nuclear membranes has been used by many research groups to estimate nuclear permeability and number of pores in the nucleus. Paine *et al.*, has studied the transport of microinjected dextran to amphibian oocyte nucleus using radioactive tracer studies as early as 1970 (Paine *et al.*, 1975, Franke, 1970). This study showed that the nuclear pore complexes contain aqueous channels of ~5 nm radius that allows passive diffusion of small molecules and metabolites across the nuclear membrane. The influx of fluorescently labeled dextrans of graded molecular size into isolated rat liver cell nuclei has been studied by fluorescence microphotolysis by the Peters group. The group estimated the functional pore radius of 5.6 – 5.9 nm for the nuclei (Peters, 1983, Peters, 1986). In another study optical single transporter recording is used to determine the permeability coefficients of single NPCs for fluorescently labeled dextrans and the diffusion channel radius is estimated to be in the range of 4.4 – 6.1 nm (Keminer & Peters, 1999, Peters *et al.*, 2002). Most of these studies are carried out under conditions such that the distribution of dextran or biomolecules is near steady state in the cytoplasm and the nucleus.

Above studies on nuclear pore size estimation are carried out in mammalian cells and the nuclear structure of these cell lines is expected to be similar to that of human cells. However a recent study on human cell lines reported much smaller nuclear pore radius for HeLa cell nuclei (Mohr *et al.*, 2009). To the best of our knowledge this is the only report on the estimation of nuclear pore channel radius in HeLa cell lines in transient conditions. In this detailed study the initial kinetics of passive transport into HeLa cell nucleus is examined using different protein molecules of radius ranging from 0.67 nm to 2.85 nm. Studies are carried out in digitonin permeabilized cells, one of the most commonly used experimental system for studying nuclear transport under transient conditions (Adam *et al.*, 1990, Faustino *et al.*, 2002, Brownawell *et al.*, 2002). These studies carried out with and without the presence of transport inhibitors suggest that both active and passive transport takes place along the same channel. Analysis of passive transport rates showed that majority of the channels have a radius of ~ 2.6 nm and that there could be few channels with larger radius.

The literature, briefly discussed above indicates that only limited data is available on the nuclear transport rates of biomolecules into the cell nucleus, and this data itself differs on the transport rates and estimated nuclear pore radius. This has prompted us to look at the nuclear import of a set of molecules having identical structure, but differed sizes to estimate the transport rates and thereby to deduce the nuclear pore radius. Fluorescein isothiocyanate (FITC) labeled dextran molecules are used as a model system and studies are carried out on the passive nuclear import of FITC labeled dextran molecules in digitonin permeabilized HeLa cells. In this chapter we present the results of the studies carried out on the passive permeability of nuclear membranes using the home built confocal laser scanning microscope, described in the chapter 2.

4.2. MATERIALS AND EXPERIMENTAL METHODS

Preparation of FITC labeled dextrans of different sizes and all other materials related to growth and maintenance of cell lines, digitonin permeabilization and confocal time lapse imaging scheme are discussed already in chapter 3.

By monitoring the diffusion of similarly structured molecules having different Stokes radius, we estimate the permeability of the membrane and determine the effective pour radius of a porous membrane. In the present study we have monitored the diffusion of FITC labeled dextran molecules from the cytoplasm to the nucleus of HeLa cells. Fluorescence intensity from the equatorial plane of the nucleus is recorded at intervals of 2.5 seconds after the injection of 1 μ M solution of FITC-dextran to cells. Dextran molecules having similar structure but different molecular weights ranging from 4 kDa, 10 kDa, 20 kDa, 40 kDa and 70 kDa are used in the study. These molecular weights correspond to equivalent Stokes radius of 1.4 nm, 2.3 nm, 3.3 nm and 4.5 nm (as per manufacturer's specification). Diffusion of 70 kDa dextran molecules having a Stokes radius of 6 nm is studied as a control experiment to confirm the integrity of the nuclear membrane. An intact nuclear membrane does not allow the entry of 70 kDa dextran molecules even after permeabilization of cell membrane. No contrary effect on cell viability is detected during the nuclear transport studies.

In all the experiments the HeLa cells are grown on glass bottom petri dishes and permeabilized with digitonin for 5 minutes before adding the import mixture. The glass bottom petri dish allows for the observation of the cells using an inverted microscope. The microscope is focused to the equatorial plane of the cells before adding the import mixture. The influx of dextran molecules to the nucleus is quantified by the strength of the fluorescence signal inside the nucleus, represented by the depth of color in the image.

4.3. RESULTS

In figure 4.1 to 4.5 we depict six representative confocal cross-sectional images of permeabilized HeLa cells taken after the addition of the import mixture containing 4 kDa, 10 kDa, 20 kDa, 40 kDa and 70 kDa dextran molecules labeled with FITC. The images show an increase in fluorescent concentration with time inside nucleus which indicates the transport of FITC labeled dextran into the nucleus. Control experimentation carried out using 70 kDa dextran molecules showed no change in intensity inside the nucleus with time. It is observed that 4 kDa and 10 kDa FITC-dextran (figure 4.1 and 4.2) is homogeneously distributed and saturated inside the nucleus within few tens of seconds while 20 kDa (figure 4.3) takes more time to become saturated. FITC-dextran with molecular weight of 70 kDa (figure 4.5) showed no signs of diffusion through nuclear membrane, whereas 40 kDa (figure 4.4) diffused into the nuclear membrane to a small extend. In figure 4.6 we show the image of the cells 100 seconds after the addition of import mixture containing dextran molecules of molecular weight 4 kDa, 10 kDa, 20 kDa, 40 kDa and 70 kDa respectively. Figure 4.7 gives the percentage of dextran molecules that have entered the cell nucleus after 100 seconds against its molecular Stokes radius. The figure clearly indicates that the diffusion rate critically depends on the molecular weight and shows that the number of higher molecular weight dextrans that have entered the nucleus is much less than that of the 4 kDa dextran molecules. At 100 seconds 98% of 4 kDa dextrans entered the nucleus while only 8% of 40 kDa entered the nucleus.

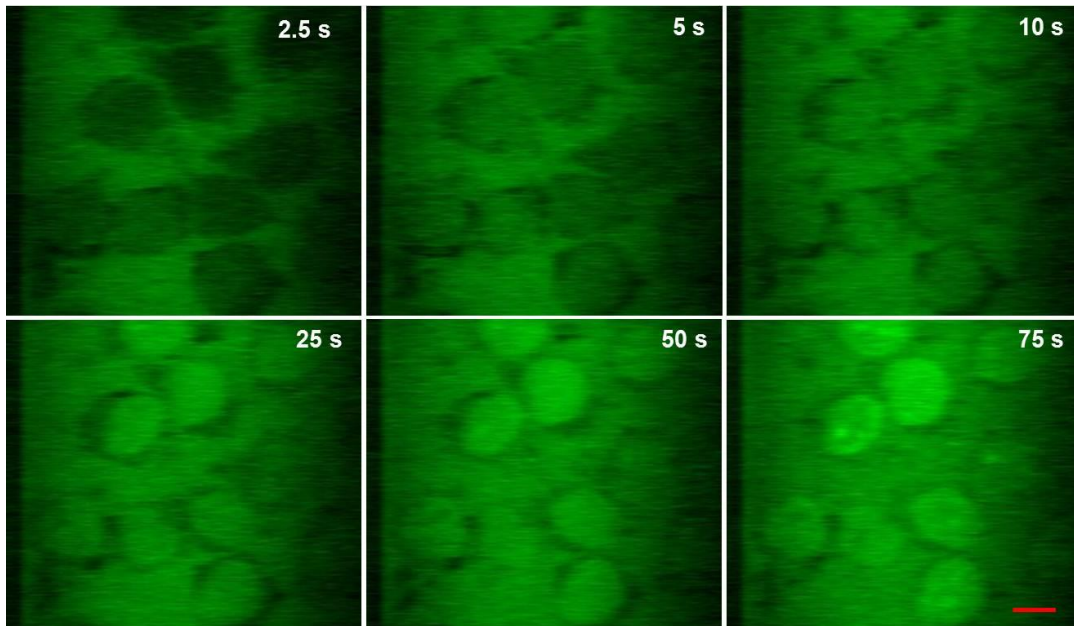


Figure 4.1: Time lapse confocal images of HeLa cell nucleus after the addition of 4 kDa FITC labeled dextran molecules. The images presented here are acquired at 2.5 s, 5 s, 10 s, 25 s, 50 s and 75 s. Scale bar is 10 μm .

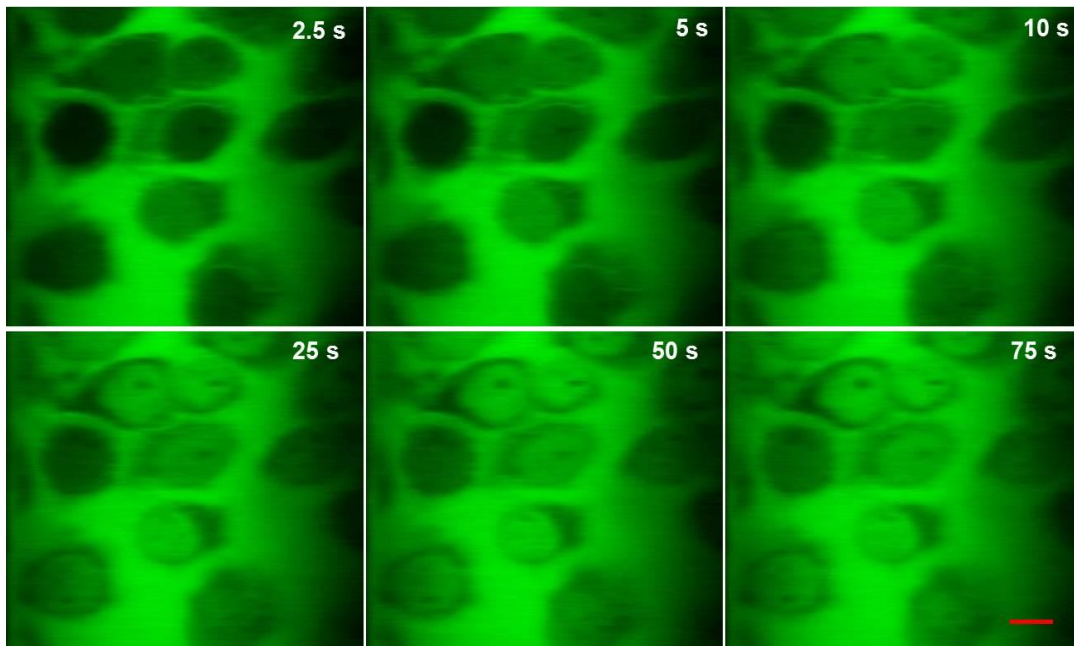


Figure 4.2: Time lapse confocal images of HeLa cell nucleus after the addition of 10 kDa FITC labeled dextran molecules. The images presented here are acquired at 2.5 s, 5 s, 10 s, 25 s, 50 s and 75 s. Scale bar is 10 μm .

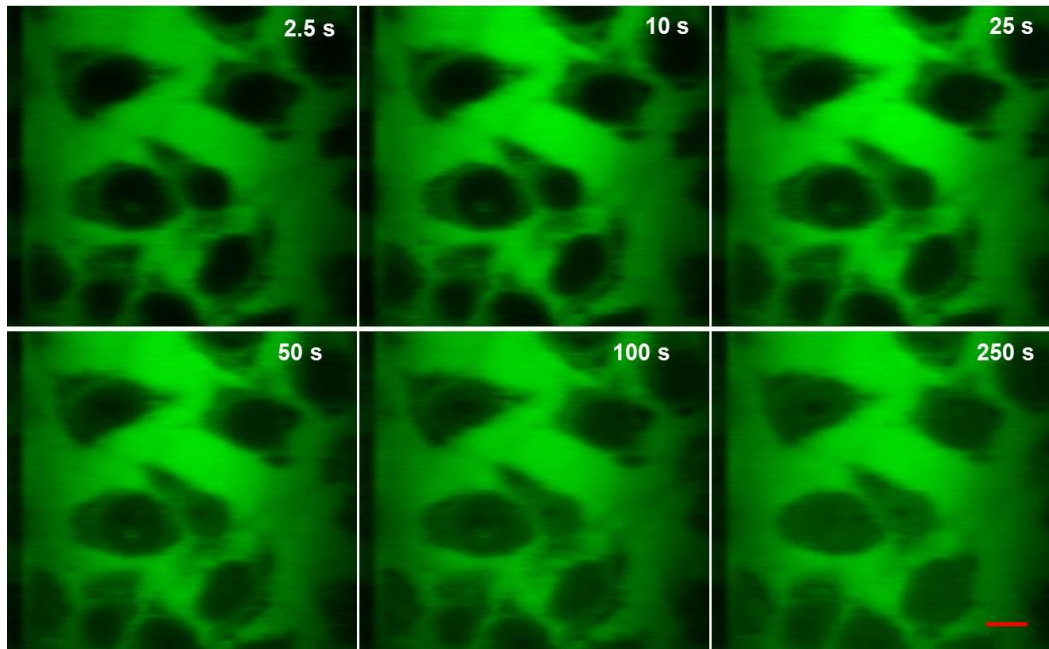


Figure 4.3: Time lapse images of HeLa cell nucleus after the addition of FITC labeled dextran molecules of MW 20 kDa. The images shown here are acquired at 2.5 s, 10 s, 25 s, 50 s, 100 s and 250 s. Scale bar is 10 μ m.

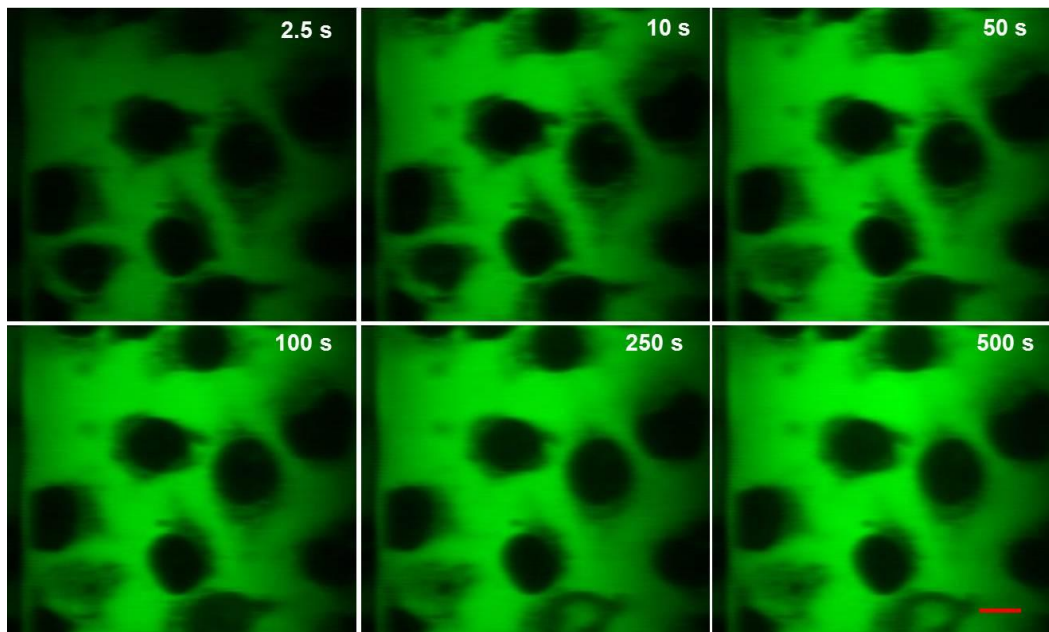


Figure 4.4: Time lapse images of HeLa cell nucleus after the addition of FITC labeled dextran molecules of MW 40 kDa. The images shown here are acquired at 2.5 s, 10 s, 50 s, 100 s, 250 s and 500 s. Scale bar is 10 μ m.

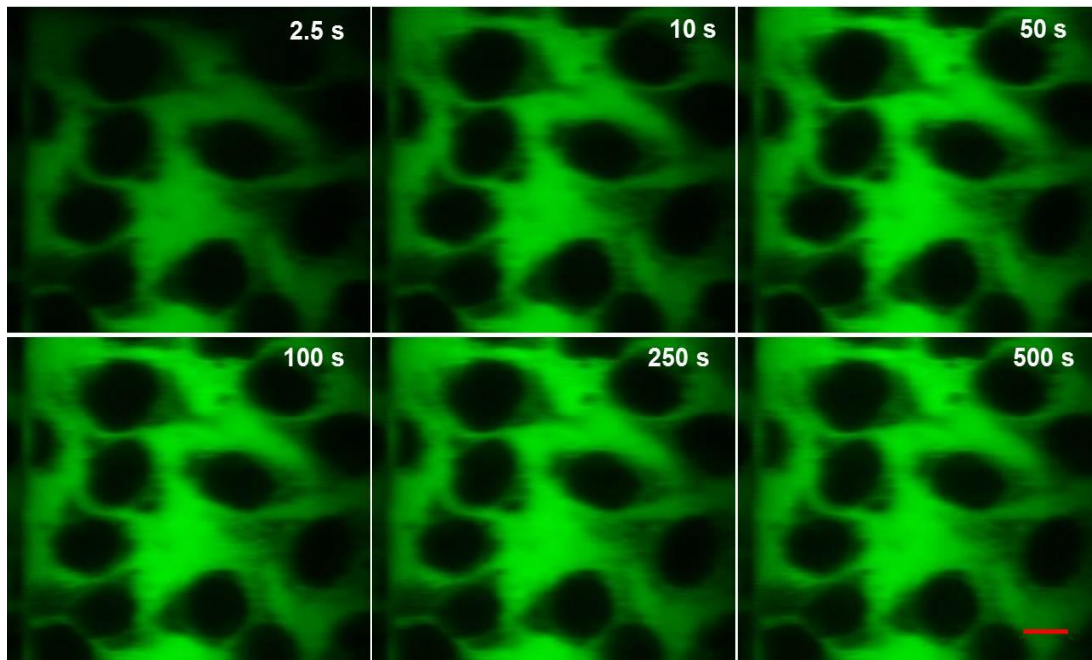


Figure 4.5: Time lapse confocal images of HeLa cell nucleus after the addition of FITC labeled dextran molecules of MW 70 kDa. The images presented here are acquired at 2.5 s, 10 s, 50 s, 100 s, 250 s and 500 s. Scale bar is 10 μm .

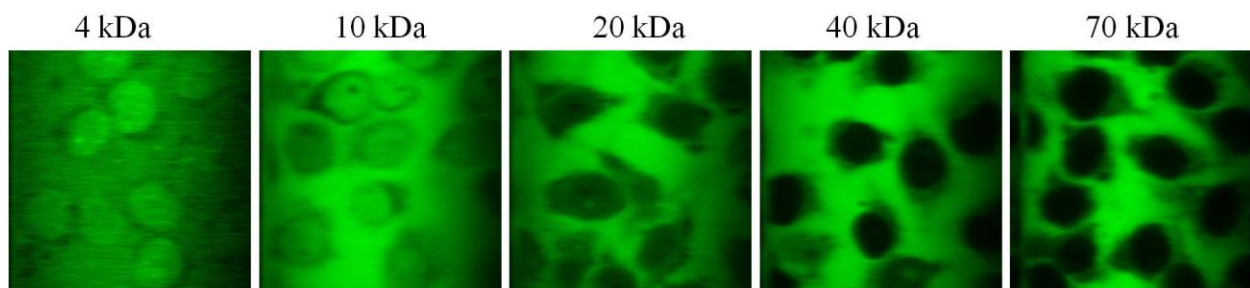


Figure 4.6: Image of the cell nucleus at 100 seconds after the addition of import mixture containing dextran molecules (1 μM) of molecular weight 4 kDa, 10 kDa, 20 kDa, 40 kDa and 70 kDa respectively.

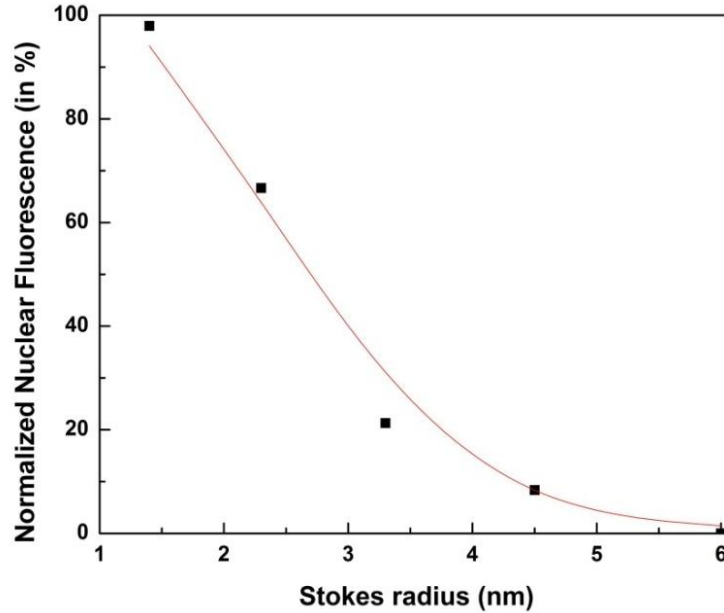


Figure 4.7: Percentage of dextran molecules that entered the cell nucleus after 100 seconds as estimated from figure 4.6. The continuous line represents the r dependence given in the equation 4.3 with the nuclear pore radius set to 5.3 nm.

In order to further quantify the diffusion and determine the rate constant of transport, we define the normalized nuclear fluorescence as the ratio of the mean intensity inside the nucleus to that of the cytoplasm. Normalized nuclear fluorescence is determined for all the four sizes of dextran molecules at time intervals of 2.5 seconds after the addition of the import mixture. If we assume first order kinetics, the normalized nuclear fluorescence $F(t)$ measured under constant experimental conditions varies as (Naim *et al.*, 2007, Mohr *et al.*, 2009),

$$F(t) = F_{max} (1 - e^{-kt}) \quad (4.1)$$

Normally the data immediately after the addition of the dye is prone to error due to non-equilibrium distribution of the dye in the cytoplasm. Hence, typically we have waited for 2.5 seconds for equilibration in each case and redefined the origin of time accordingly. In figure 4.8 we show the plot of $F(t)$ versus time after addition and equilibrations of FITC labeled dextran molecules of molecular weight 4 kDa (■), 10 kDa (●), 20 kDa (▲) and 40 kDa (▼). The data for all the four curves fits well to the single-exponential curve defined in equation 4.1 confirming first order kinetics. The rate constants of transport (k) and the saturation value of

normalized fluorescence F_{max} can be obtained from the best fit to the data as shown in figure 4.8. From the figure it can be observed that the rate constants of transport critically depend on the size of the particles. Further it can be noticed that the value of F_{max} differs from 1 and is varying with the size of dextran molecules. If the nucleus and cytoplasm are both filled with perfect aqueous solutions, one would expect that passive nuclear transport by diffusion would proceed towards an equilibrium value of 1. The difference observe in these experiments may be attributed to the differential phase properties of the medium in the two compartments and the presence of preferential binding sites for dextran in the cytoplasm.

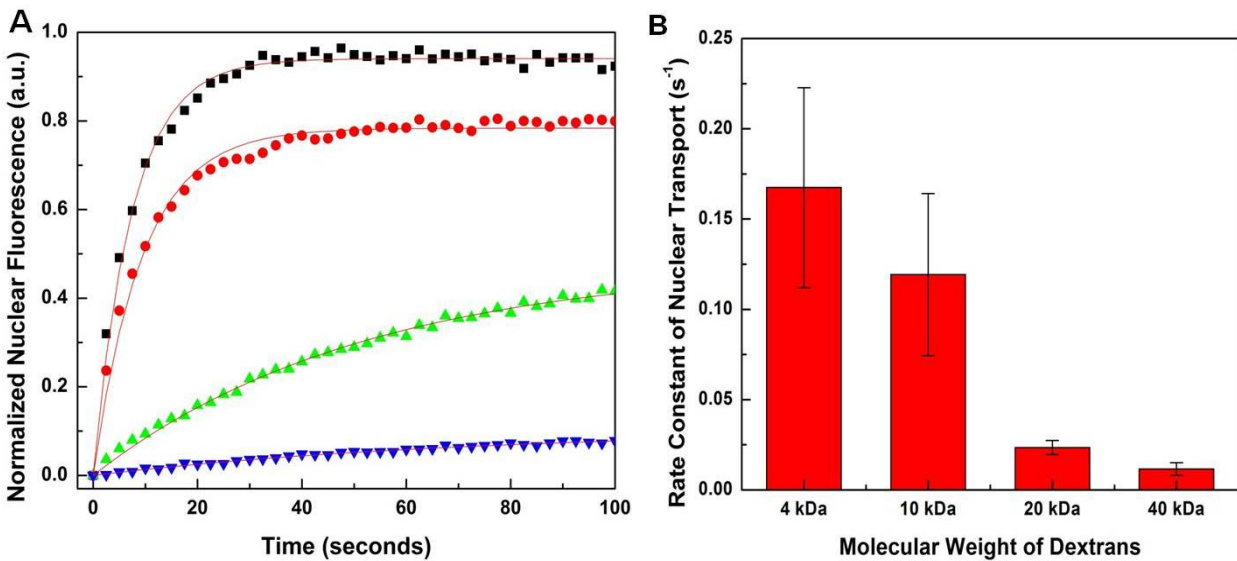


Figure 4.8: (A) Nucleo-cytoplasmic flux of dextrans having four different molecular mass. Plot shows normalized nuclear fluorescence versus time for the transport of FITC labeled dextrans of 4 kDa (■), 10 kDa (●), 20 kDa (▲) and 40 kDa (▼). In all experiments, the time-dependent rise in the ratio between background corrected nuclear and cytoplasmic mean fluorescence intensity, is fitted well to a single-exponential curve of the form $F(t) = F_{max} (1 - e^{-kt})$, where t is time, $F(t)$ is the normalized nuclear fluorescence, F_{max} is the endpoint of the reaction and k is the first-order rate constant. (B) Nuclear import rate constants of FITC labeled dextrans of four different molecular weights. The data shown here are representative data corresponding to a particular nucleus. The rate constants shown are average over many nuclei.

The rate constant (k) is related to the permeability coefficient (P) by (Peters, 1983),

$$P = (V/A)k \quad (4.2)$$

Where V and A are the volume and area, respectively, of the cell nucleus. HeLa cell nuclei can be approximated by spheres of radius $R = 6 \mu\text{m}$. V/A is then equal to $R/3 = 2 \mu\text{m}$. We have carried out the experiments on 4 sets of plates each containing minimum of 4 – 5 cells in the imaging area. The average rate constants and permeability is calculated by averaging the rate constants of about 16 – 20 well congruent nucleus. Cells near the edges of the petridish are not considered for the analysis. The average rate constants and permeability of transport of dextran molecules into the nucleus thus deduced is given in table 4.1.

Table 4.1: Rate constants of transport and permeability coefficients of HeLa cells nuclear membrane for dextran molecules.

Molecular mass of Dextran molecules	Stokes radius	Rate constant $k \text{ s}^{-1}$	Permeability coefficient $P \times 10^{-8} \text{ m/s}$
4 kDa	1.4 nm	0.26 ± 0.06	52
10 kDa	2.3 nm	0.10 ± 0.02	20
20 kDa	3.3 nm	0.024 ± 0.003	4.8
40 kDa	4.5 nm	0.009 ± 0.003	1.8

If passive diffusion is the major process for translocation, the rate constant k for molecules having radius (r) less than that of the pore radius (R) is given by, (Mohr *et al.*, 2009)

$$k = \frac{\text{NPC's per nucleus. channels per pore. } k_B \cdot T \cdot (R - r)^2}{V \cdot L \cdot 6 \cdot \pi \cdot \eta \cdot r} \quad (4.3)$$

Here η is the viscosity of the medium within the nuclear pore channel; k_B is the Boltzmann constant, V is the nuclear volume, L is the length of the channels and T is the absolute temperature. Thus, the number of molecules that have diffused into the nucleus at any particular time critically depends on the ratio $(R-r)^2/r$. In figure 4.7 the continuous line represents the r dependence given in the equation 4.3 with an assumed nuclear pore radius of 5.3 nm.

Equation 4.3 contains many unknown parameters and it will not be possible to determine the values of R from this equation through a best fit. We may eliminate the unknown parameters in equation 4.3 by taking the ratio q_i of the rate constant from dextran molecules of two different Stokes radii.

$$q_i = \frac{k_i}{k_{ref}} = \frac{r_{ref} (R - r_i)^2}{r_i (R - r_{ref})^2} \quad (4.4)$$

The nuclear pore radius R may be estimated from ratio q_i for a series of molecules by considering one of the molecules as a reference molecule. In table 4.2 we give three sets of ratios q_i 's, with 4 kDa, 10 kDa and 20 kDa molecules as reference. We plotted the ratio q_i against the molecular Stokes radius (r_i) and the best value of the nuclear pore radius (R) satisfying equation 4.4 is determined graphically through best fit as shown in figure 4.9. The R values thus deduced for the three sets of ratios are also given in the table 4.2. The average nuclear pore radius is thus estimated as 5.3 nm.

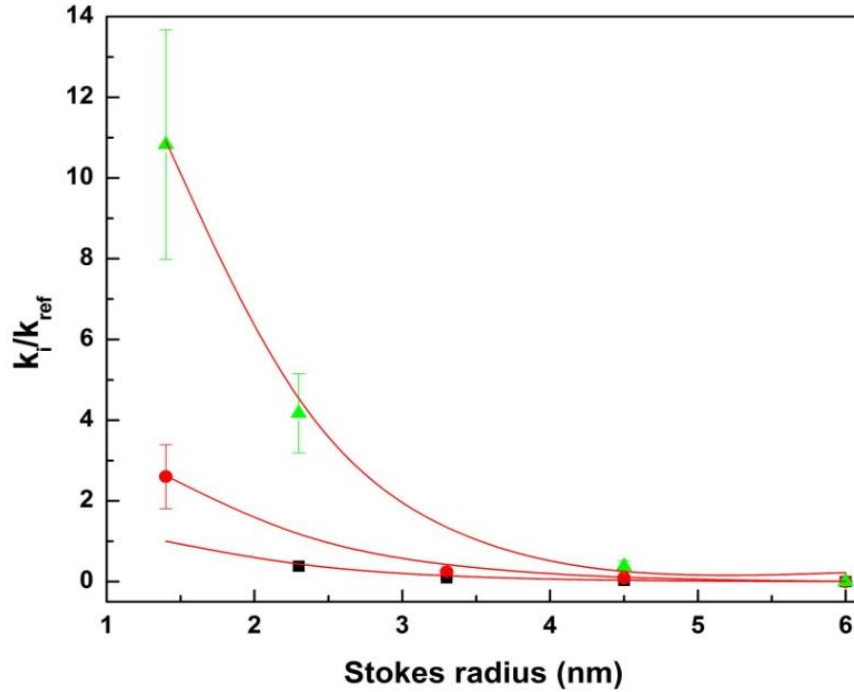


Figure 4.9: Estimation of passive pore radius from diffusion rates. The ratio of rate constants of the molecules to that of a reference molecule (k_i/k_{ref}) plotted against the Stokes radius for the three sets of ratios. (■) Reference molecule 4 kDa, (●) Reference molecule 10 kDa and (▲) Reference molecule 20 kDa. The radius R of the nuclear pore is deduced from a best fit (solid line) to the data satisfying equation 4.4.

Table 4.2: Equivalent radius of the diffusion channel in the nuclear pore complex. q_i is the ratio of rate constants of the molecules (k_i) to that of a reference molecule (k_{ref}). R values are estimated from the best fit to the data in figure 4.9.

Reference Dextran Molecule	$q_i = k_i/k_{ref}$				Estimated R Value from fittings (nm)
	4 kDa	10 kDa	20 kDa	40 kDa	
4 kDa	—	0.4 ± 0.1	0.09 ± 0.02	0.03 ± 0.01	5.4 ± 0.2
10 kDa	2.5 ± 0.8	—	0.24 ± 0.06	0.09 ± 0.03	5.7 ± 0.2
20 kDa	11 ± 3	4 ± 1	—	0.4 ± 0.1	4.95 ± 0.05

4.4. DISCUSSIONS

The nucleus of the cell stores and organizes the genetic code of an organism and protects this information from other cellular components. The nuclear pore complex, the biggest protein complex in the cell, is responsible for the protected exchange of components between the nucleus and cytoplasm and for stopping the transport of material not meant to cross the nuclear envelope. The structure and properties of this functionally important protein complex is still not well understood. In this work we have used dextrans, a biocompatible and neutral polysaccharide molecule having molecular weight greater than 1000 Dalton as a model system for studying nuclear transport rates and permeability of nuclear membrane. Passive diffusion studies are carried out under transient conditions using time lapse confocal fluorescence microscopy.

The experimental system of choice used for the studies are permeabilized HeLa cells, which have leaky plasma membranes but intact nuclei. Digitonin permeabilization on adherent cells works best when the cells are 40 – 70% confluent and poorly if the cells are approaching confluence. Cells that are not well adhered may detach during the permeabilization and washing steps. Cells near the edge of the cover slip may be subject to evaporation artifacts and hence our analysis is limited to cells in the central area of the cover slip. Dextrans used in this study have an average molecular mass of 4 kDa, 10 kDa, 20 kDa 40 kDa and 70 kDa respectively, and the degree of labeling is 0.003 to 0.02 moles of FITC per mole of glucose. Table 4.1 gives the diffusion rate constants and permeability values for the above four dextran molecules in HeLa cell nucleus. The effective pore radius estimated from the study is given in table 4.2.

FITC labeled dextran molecules studied here are used extensively in microcirculation and cell permeability research in the literature. When diffusion is the major process by which molecules are transported through the membranes, the permeability of the molecule depends on its size. It can be seen from table. 4.1 that there is a strong dependence of permeability on the size of the dextran. It decreases more than 10-fold for a 2.36-fold increase of molecular radius. While 4 kDa molecules are readily transported to the nucleus, 40 kDa molecules are sparingly transported. The rate constants obtained by us are of the same order of magnitude as reported in other cells using different techniques (Peters, 1983). The effective pore radius estimated by us is also in general agreement with the previous studies in mammalian cells. Paine *et al.*, estimate the

pore radius to be 4.5 – 5 nm (Paine *et al.*, 1975). Peters and co-workers using steady state diffusion analysis have reported the pore radius to be 5.6 – 5.9 nm (Peters, 1983, Peters, 1986). Using optical single transporter recording studies Peters group has estimated the pore radius to be 4.4 – 6.1 nm (Keminer & Peters, 1999, Peters *et al.*, 2002).

In contrast to the above studies Mohr *et al.*, in a detailed study on diffusion of small protein molecules, have estimated a much smaller nuclear pore radius for HeLa cell nuclei. They conducted passive diffusion studies under transient conditions and found that protein molecules of radius less than 2.5 nm are readily transported to the nucleus while those having radius larger 2.6 nm are sparingly transported. The rate of nuclear transport reported by Mohr *et al* is less than that obtained in the present work and in earlier studies. One of the main differences between this study and our work is that we have used inert dextran molecules to probe the nuclear transport compared to the protein molecules used by Mohr *et al.* Here we wonder whether the non-specific binding of protein molecules to the Phenylalanine Glycine (FG) repeat units in the NPC hinders the flow of protein molecules. We should also take into account, as pointed out by Mohr *et al*, the possible effects of the ellipsoidal shape of dextran molecules. However the Stokes radius of the dextran molecules used here is defined as the radius of a hard sphere that diffuses at the same rate. Equivalent pore analysis based on mean spherical shape better approximates the passive diffusion of macromolecules across membrane pathways (Matsukawa *et al.*, 1997, van Os *et al.*, 1974).

Another important difference in our experiments is that we have used 50% RRL in the import mixture added to permeabilized cells so as to mimic the actual living conditions of the cell. The RRL we used in the import mixture, and normally found in cell cytoplasm could have a favorable effect on the transport of passive molecules through the nuclear membrane. RRL contains importin β which normally assists active transport through the nuclear membrane. If active and passive nuclear transport take place through the same channel, then molecules such as importin β that help active translocation should also help passive diffusion. Mohr *et al.*, have shown that the inhibitor negative importin β affects both passive and active transport of molecules through nuclear membrane. We feel that the effect of cytosolic extract/RRL on the nuclear transport of both active and passive pathways has to be examined more thoroughly.

In summary, the Kinetics of transport of FITC labeled dextran molecules through HeLa cell nuclear membrane is studied using an in-house constructed confocal laser scanning microscope. Membrane permeability of digitonin permeabilized cells is determined for the sizes 4 kDa, 10 kDa, 20 kDa and 40 kDa. The 40 kDa molecules are transported across the nucleus with very low rate constant, while 70 kDa molecules are completely blocked. From the analysis of the diffusion rate constants of these molecules, we estimate the effective pore radius of HeLa cell nucleus to be in the range of 4.9 – 5.7 nm (mean 5.3 nm).

CHAPTER FIVE

INFLUENCE OF RABBIT RETICULOCYTE LYSATE ON THE NUCLEAR
TRANSPORT KINETICS OF DEXTRAN AND DNA

5.1. INTRODUCTION

There has been a considerable interest in recent years on the nuclear delivery of deoxyribonucleic acid (DNA) from the point of view of gene therapy strategies (Vacik *et al.*, 1999, Munkonge *et al.*, 2003). In gene therapy a foreign DNA is transferred to the nuclei for its transcription so as to express a therapeutic protein. Normally the cell nucleus is not receptive to this DNA and the efficiency of such gene delivery is very poor. The ability to send a desired molecule into the nucleus is a crucial first step in non-viral gene delivery and the success of gene therapy experiments will depend on strategies that can enhance the nuclear uptake of DNA. However the kinetics of transport of DNA into the nucleus is not well studied and the environmental factors that affect the transport rates are largely unknown.

DNA import into the nucleus is size dependent. In this study we analyze the effect of linear double stranded DNA fragment size on its passive diffusion to A549 cell nuclei and determine the transport rate constants. The import assay is performed using Polymerase chain reaction (PCR) products of various molecular weights. Studies are carried out on fluorescein labeled DNA having 113 base pairs (bp), 304 bp, 480 bp, 750 bp and 1000 bp using time lapse confocal fluorescence imaging in digitonin permeabilized cells.

There could be different factors that can positively or negatively affect the transfection efficiency. Cytosolic extract, present in the cell cytoplasm in nature and consisting of water, dissolved ions, small molecules, and protein molecules, play an important role in the regulation of cell functions. Rabbit reticulocyte lysate (RRL) is a compound normally used as a substitute for cytosolic extract to mimic the normal living environment of a cell in laboratory experiments. The RRL contains the cellular components tRNA, amino acids, ribosomes, and initiation, elongation and termination factors which are essential for protein synthesis. RRL contains

transport receptors like importin β , which binds to the FG repeats due to hydrophobic interactions and is found to increase the rate of the active transport. Here we study the effect RRL concentration in the import mixture on the passive diffusion of biomolecules by taking dextran molecules of varying molecular weights as the model system. The study shows that the transport rates of dextran molecule are influenced significantly by the concentration of RRL in the import mixture. Further we looked at the effect of RRL on the transport rates of DNA base pairs by carrying out the studies using import mixture containing 50% of RRL. This concentration is chosen based on results of studies carried out in the model system, dextran. Studies are repeated in many cells with and without the presence of RRL in the import mixture and the rate constants are compared. The study shows that the RRL present in the cell do influence the nuclear uptake of DNA positively and that the transfection efficiencies could be increased by increasing the concentration of RRL.

This chapter will start with background introduction of materials used in study of nuclear transport of DNA fragments. Major components of such a transport assay including preparation of different size of DNA fragments, cell culture reagents, transport buffer and import mixture components and fluorescent labeling techniques will be individually addressed. Subsequently we will discuss the dependence of the RRL concentration on the nuclear import rates of dextran molecules of various Stokes radii. After that the transport kinetics of different sizes of fluorescently labeled DNA's in the presence and absence of RRL will be presented. The chapter will end with a discussion on the results of RRL dependence on biomolecular transport through nuclear membranes.

5.2. MATERIALS

5.2.1. Materials used in PCR Reaction

Lambda DNA

We used Lambda DNA as a template DNA in PCR reaction for amplification of DNA fragments. Template DNA is the DNA molecule containing the segment of DNA to be amplified. Lambda

DNA is a linear, double stranded DNA of 48502 bp size (product code: MAR 04) and is obtained from Chromous Biotech Pvt. Ltd., Bangalore.

Primers

Primers are small piece of DNA (typically 18 to 25 bases long) that bind to complementary regions on opposite strands of the template DNA. The primers serve as replication initiation points. Two primers are used to amplify one DNA segment namely forward primer (FP) and reverse primer (RP). Primers are obtained from BioCorporals Pvt. Ltd., Chennai.

DNA Polymerase

DNA polymerase is the enzyme used to amplify DNA molecule. It adds bases onto the 3' ends of the annealed primers. DNA polymerase should be stable at high temperatures for using in PCR. We used the AmpliTaq enzyme, a DNA polymerase isolated from bacteria that prosper in the hot springs. TAQ DNA polymerase (D4545-1.5KU) is obtained from Sigma Aldrich chemicals Pvt. Ltd., Bangalore.

Magnesium Chloride

Mg^{2+} is a cofactor for the enzyme DNA polymerase. Magnesium chloride is used as a source to provide magnesium ion (Mg^{2+}) to the PCR reaction. DNA polymerase will not function without Mg^{2+} .

dNTPs

dNTPs (deoxynucleoside triphosphates) are the nucleotides used by the DNA polymerase enzyme for addition onto the 3' ends of the annealed primers. Deoxynucleotide set, which contain 0.5 mL each of 10 mM dATP, dCTP, dGTP and dTTP (DNTP10-1KT) kit is obtained from Sigma Aldrich chemicals Pvt. Ltd., Bangalore.

PCR Buffer

PCR buffer obtained from Sigma Aldrich maintains the pH of the PCR reaction mixture at a level where the DNA polymerase is most active.

PCR Machine

Biorad MJ Mini thermal cycler (Product code: PTC-1148) is used in our studies for DNA amplification. We can set the temperature control in the machine and also store our protocol and run whenever is needed. The MJ mini cycler accepts both 0.2 mL and 0.5 mL tubes. Protocols may require some adjustment to ensure optimum performance when using a different vessel type. We usually use 0.5 mL PCR tubes with the total reaction volume upto 50 μ L.

3.2.2. Reagents Used in DNA Preparation

TAE Buffer

TAE buffer is a buffer solution containing a mixture of Tris base, acetic acid and EDTA. In molecular biology it is used in agarose electrophoresis experiments typically for the separation of nucleic acids such as DNA and RNA. It is made up of Tris-acetate buffer, usually at pH 8.0, and EDTA, which sequesters divalent cations. The constitution is tris-acetate 0.4 M, ethylene di-amino tetra acetic acid (EDTA) 0.01 M.

Agarose

Agarose (Product code: BIO-41026) is obtained from LGC Promochem India Pvt. Ltd., Bangalore. Agarose is often used in molecular biology for the separation of large biomolecules, particularly DNA, by electrophoresis. Slabs of agarose gels for electrophoresis are readily prepared (usually 0.7 – 2%) by pouring the warm, liquid TAE buffer into a gel cast. We have used 2% of Agarose in TAE buffer for separating the DNA fragments from 100 – 2000 bp in size.

Fluorescein

Fluorescein is a fluorophore frequently used in microscopy as a fluorescent tracer for many biological imaging applications. Fluorescein has an absorption maximum at 490 nm and emission maximum of 514 nm in 0.1 M Tris buffer with pH 8.0. We used this fluorescein (Sigma Aldrich, Product code - 46955) for labeling DNA fragments.

5.3. EXPERIMENTAL METHODS

Growth and maintenance of cell lines, digitonin permeabilization and confocal time lapse imaging schemes are discussed already in previous chapters.

5.3.1. Preparation of DNA for Nuclear Transport Studies

For the nuclear transport studies we prepared different sizes of bacteriophage λ -DNA using Polymerase chain reaction (PCR). DNA fragments are purified and then labeled with fluorescent dye for nuclear transport study.

Primer Design

We designed the primers for the PCR reaction to get the desired length of the DNA. Primers are designed using the Primer3 software tool and Invitrogen oligo perfect designer. The primers are used to make DNA fragments of different sizes by PCR amplification method. The sequences of the primers and the product length are given in table 5.1. For the experiments DNA is covalently labeled with different fluorescent dyes.

Table 5.1: PCR Primer Sequences and PCR Product length. FP indicates forward/upstream primer; RP indicates reverse/downstream primer.

DNA fragment name	Product Length	PCR Primer Sequences
DNA seq. 1	113 bp	FP1: 5'- AGGAGCTGGACTTTACTGATGC -3' RP1: 5'- ACTGTCAGGTGGCTCAATCTCT -3'
DNA seq. 2	304 bp	FP2: 5'- CATTGAGAGTGAGCTGGATACG -3' RP2: 5'- GTAGCTCATCTGGGCGTAATTC -3'
DNA seq. 3	480 bp	FP3: 5'- CCTCAGAGAGGCTGATCACTAT -3' RP3: 5'- AGCAGTAGCACCAAAGGAAACC -3'
DNA seq. 4	750 bp	FP4: 5'- CATTGAGAGTGAGCTGGATACG -3' RP4: 5'- CTGCTGTCACCTCTTCTCCTCCT -3'

5.3.2. PCR Reaction

Polymerase chain reaction is carried out to amplify DNA fragments. Reaction is performed on a PCR machine (Biorad MJMini thermal cycler). Reaction conditions are optimized based upon the melting temperature (T_m) of the primers, the guanine-cytosine (GC) content and length of the amplified fragment. Typically, reaction volume is 50 μL . 5 μL of complete PCR buffer (Sigma), 1 μL Taq DNA polymerase (Sigma), 1 μL 10 mM dNTP's and 100 ng of each primer are added to the target DNA and the volume made up by UV treated nuclease free water (sterile injection water). 10 ng – 1 μg DNA is used depending on the quality of the sample. Typical amplification conditions are 35 – 40 cycles of 95°C for 1 minute, 55°C for 1 min, 72°C for 2 minutes, followed by a further 1 minute at 72°C. Controls included a no polymerase reaction and a no template DNA reaction to ensure there is no cross contamination. If no product is seen, the annealing step (55°C) temperature is lowered, if multiple nonspecific products are seen, this temperature is increased. If the product is large (>1kb), the length of the extension step (72°C) is increased to 4 or 6 minutes. After cycling, the product is mixed with 4X DNA loading buffer and placed on agarose gel for analysis. Optimized volume of PCR reaction constituents and reaction conditions are as given below.

Reaction Setup

Reaction buffer	5 μL
MgCl ₂	5 μL (total conc. should to be 5mM)
dNTPS	5 μL (total conc. should to be 0.2 to 0.5mM)
Lambda DNA	2 μL
Forward primer	1 μL
Reverse primer	1 μL
Taq DNA polymerase	0.5 μL
Nuclease free water	30.5 μL

Total volume 50 μ L

Reaction Conditions

Initiation 95°C for 3 min

Denaturation 94°C for 30 sec

Annealing 55°C for 30 sec

Extension 72°C for 1 min

35 cycles

Final extension 72°C for 5 min

5.3.3. Agarose Gel Analysis

1% weight/ volume (w/v) agarose in TAE (tris-acetate 0.4 M, ethylene di-amino tetra acetic acid (EDTA) 0.01 M) gels are used for analysis throughout this studies. Agarose gels are prepared by heating the agarose in 1X TAE mixture until the agarose is fully dissolved. Between 50 and 100 mL of the solution is poured into a gel cast, an appropriate comb added and left to cool for 10 – 15 minutes. Gels are placed in a tank containing 1X TAE. Samples are loaded with a Promega 1 kb ladder in lane 1 and electrophoresed at 50 – 100 V/cm for 30 minutes for 2 hours depending on the size of fragments and resolution required.

5.3.4. Purification of DNA Fragments

Enzyme is removed by agarose gel analysis and extraction using Bioline PCR clean-up kit (used according to the manufacturers guidelines). After blunting, alkaline phosphatase treatment is required to prevent backbone self-ligation. 5 units of alkaline phosphatase is added to the DNA and 5 μ L of SAP 10X buffers. Final volume is made up to 50 μ l with water. This mixture is incubated at 37°C for 15 minutes and enzyme removed by phenol/chloroform extraction. Up to 100 mg of gel is placed in an eppendorf tube and 300 μ l buffer added (BIOLINE). Mixture is incubated at 65°C for 10 minutes and purified using supplied column, centrifugation at 13,000 g

and washing using buffer QG and PE. Elution is in 50 μL (or 30 μL if quantity of DNA is low or high concentration of DNA is required) sterile water.

5.3.5. Fluorescent Dye Labeling of DNA

Labeling of DNA is done with the fluorescein dye molecules by covalent labeling method. λ -DNA is added to a solution of the dye in 40 mM Tris-acetate, 2 mM EDTA, pH 8.0 to yield a DNA concentration of 0.3 ng/ μL and a minimum ratio of 5:1, DNA base pairs (bp) to dye molecules. Ratio 5:1 corresponds to addition of 0.3 ng of λ -DNA to 0.1 μM dye (Frank H. Stephenson, 2008). The extent of labeling is checked by running the dye labeled DNA in agarose gel electrophoresis followed by visualization using a UV – transillumination.

5.3.6. Preparation of Cells for Nuclear Transport

A549 cells are cultured in Dulbecco's minimum essential complete medium with 10% heat inactivated fetal bovine serum at 37°C in a humid atmosphere containing 5% CO_2 , and passaged every 3 days. The cells are grown on the glass bottom petri dish to enable it to be viewed under the 60X objective. For nuclear transport studies, cells are used in 24 – 48 hour after seeding on glass bottom petri dish. Cells on coverslips are washed and permeabilized with digitonin (HiMedia; 40 $\mu\text{g}/\text{mL}$) for 5 minute at room temperature. Permeabilization reaction is stopped by aspirating the digitonin solution and replacing with complete transport buffer. Cells are washed thrice by alternate steps of aspiration and transport buffer addition. After washing with 1X TB, cells in the imaging chamber is mounted on the inverted microscope (equipped with a 60X, NA – 1.25 oil immersion objective lens) stage and allowed to equilibrate for few minute before microscope analysis.

5.4. RESULTS

5.4.1. RRL Dependence of Dextran Transport

Nuclear import assays are performed with rabbit reticulocyte lysate as a cytosol source in the import mixture. Measurement of Protein concentration in dialyzed RRL extract is done in Nanodrop lite spectrophotometer. And the concentration of protein present in RRL is found to be

around 40 mg/mL. Time lapse confocal imaging studies are carried out on the nuclear import of dextran molecules of Stokes radius 2.3 nm (10 kDa) and 3.3 nm (20 kDa). The concentrations of dextran in all experiments are kept at 1 μ M. The confocal imaging of the nuclear import of dextrans of both sizes are repeated with import mixture containing 0%, 12.5%, 25%, 50% and 75% RRL. The respective concentration of RRL in import mixture is 0, 5, 10, 20 and 30 mg/mL.

Confocal cross sectional images of the equatorial plane of the nuclei are taken at 2.5 s interval after the addition of the import mixture so as to study the nuclear transport of dextrans. Figure 5.1 shows 5 representative confocal cross sectional images of the nuclei taken 2.5 s, 5 s, 10 s, 50 s and 100 s after the addition of import mixture containing 1 μ M of 10 kDa dextran molecules for different RRL concentrations. Figures 5.1 (A) to 5.1 (E) are confocal cross sectional images after addition of import mixture having RRL concentration of 0 mg/mL, 5 mg/mL, 10 mg/mL, 20 mg/mL and 30 mg/mL respectively, but with the same concentration of dextrans. These data are analyzed to determine the normalized integrated nuclear fluorescence $F(t)$ at each 2.5 s interval after the addition of import mixture. The rate constants of transport are extracted from normalized nuclear fluorescence verses time graphs with the help of best fitting to a first order kinetic function as described in chapter 3. The experiment is repeated with 20 kDa dextrans and the results depicted in figure 5.2. (A to E). In Figure 5.3 we plot the average normalized nuclear fluorescence as a function of time for 10 kDa (A) and 20 kDa (B) experiments with different RRL concentrations. Table 5.2 gives the rate constants of transport of 10 kDa and 20 kDa dextran molecules for different RRL concentrations.

The experiments described above are repeated on 3 – 5 plates, each containing minimum of 3 – 8 cells. Thus, the transport rates reported in table 5.2 are an average over a minimum of 10 cells. The spread in the rate constants over different cells are given in this table. In figure 5.4 we compare the average nuclear transport rates of 10 kDa and 20 kDa dextran molecules in A549 cells for various RRL concentrations. The figure shows that the transport rates of both these sizes are strongly influenced by RRL and that the rates are enhanced by more than a factor of 2 for 30 mg/mL of RRL concentration. Also it can be noticed that the enhancement in rate constants of transport is higher in dextran molecule of molecular weight 10 kDa.

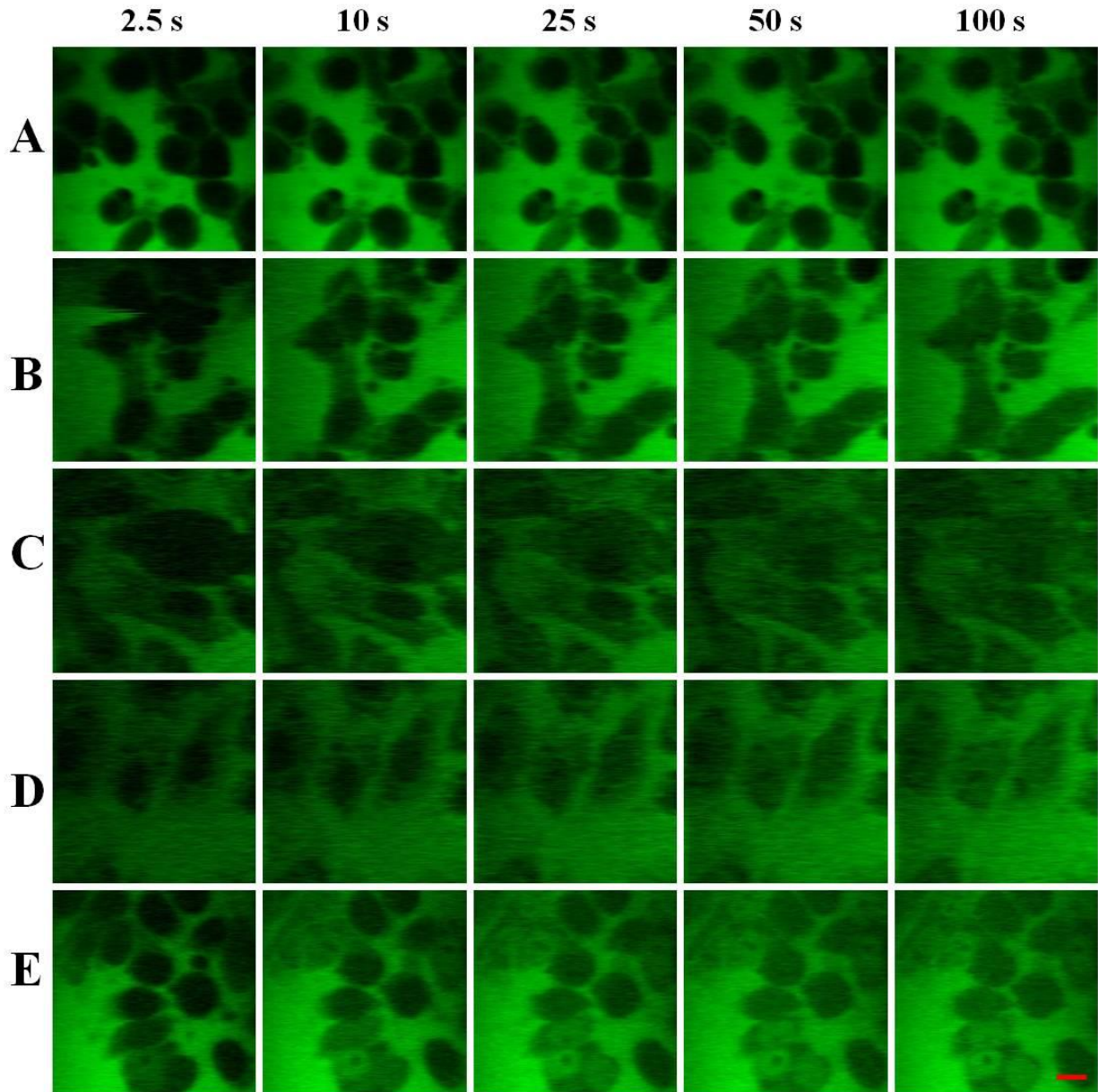


Figure 5.1: Time lapse confocal images of A549 cell nucleus after the addition of FITC labeled dextran molecules of MW 10 kDa with different RRL concentrations of 0 mg/mL (A), 5 mg/mL (B), 10 mg/mL (C), 20 mg/mL (D) and 30 mg/mL (E). The images shown are acquired at 2.5 s, 10 s, 25 s, 50 s and 100 s. Scale bar – 10 μ m.

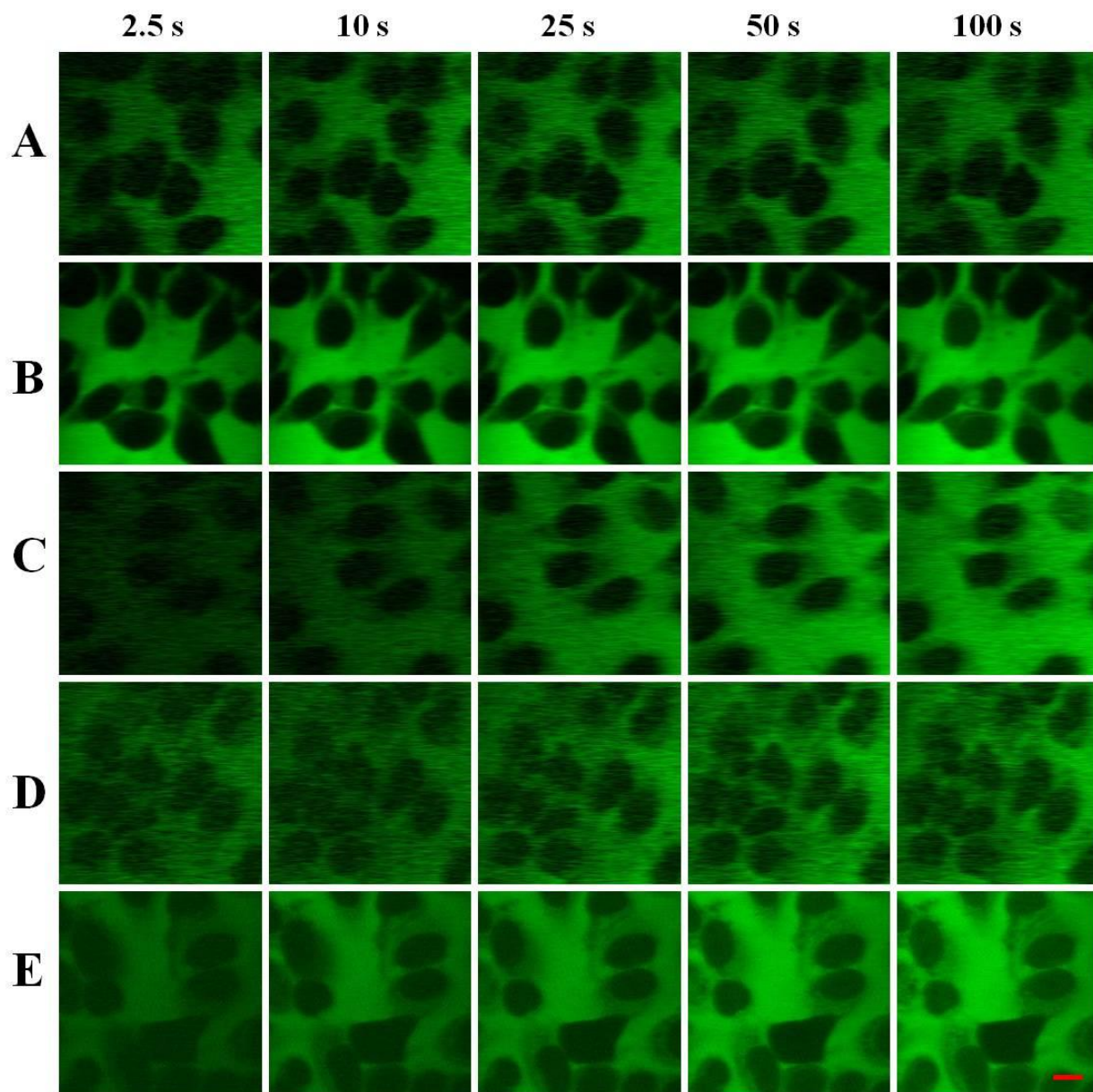


Figure 5.2: Time lapse confocal images of A549 cell nucleus after the addition of FITC labeled dextran molecules of MW 20 kDa with different RRL concentrations of 0 mg/mL (A), 5 mg/mL (B), 10 mg/mL (C), 20 mg/mL (D) and 30 mg/mL (E). The images shown are acquired at 2.5 s, 10 s, 25 s, 50 s and 100 s. Scale bar – 10 μ m.

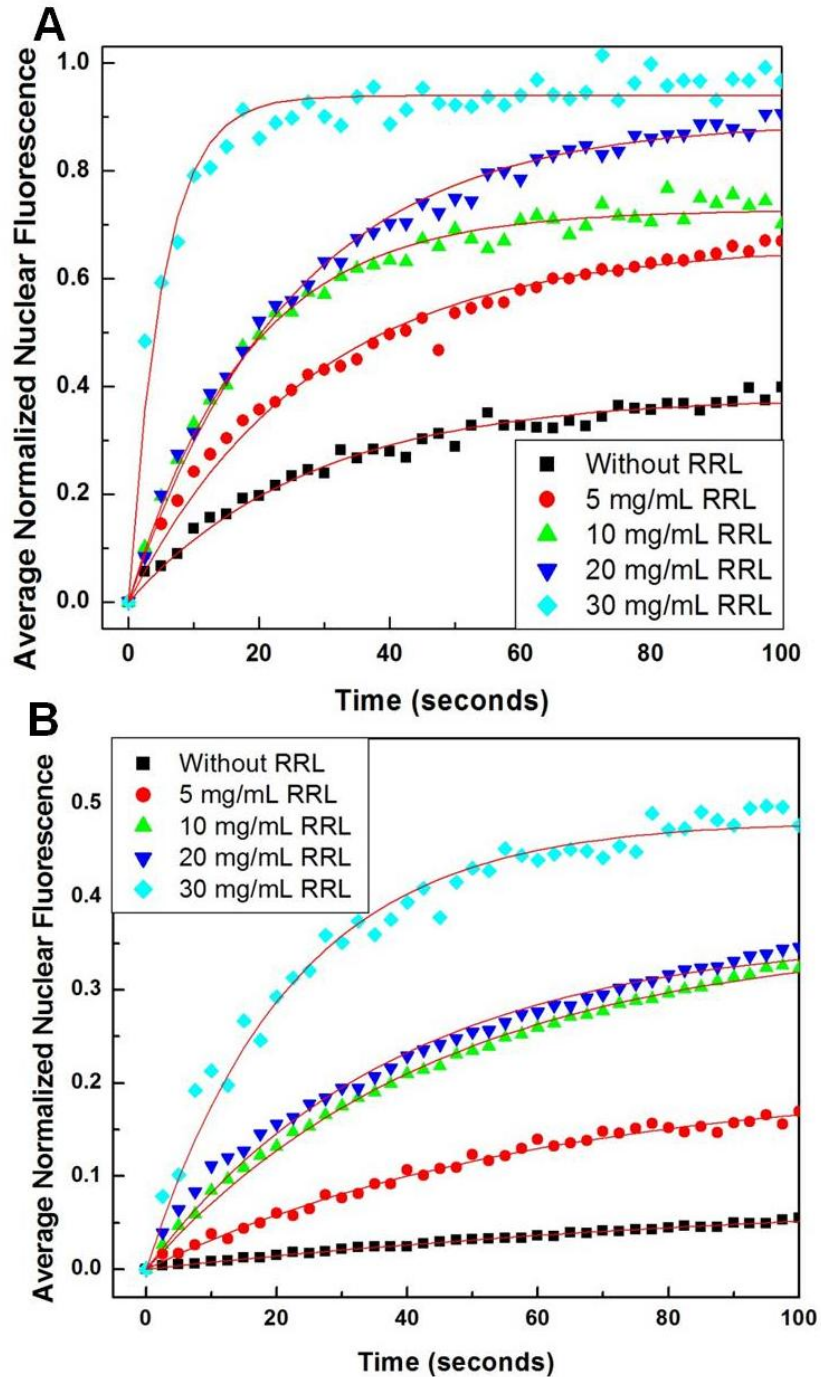


Figure 5.3: Nucleo cytoplasmic flux of dextran molecules of 10 kDa (A) and 20 kDa (B) with four different concentrations of RRL. Plot shows average normalized nuclear fluorescence versus time for the transport of FITC labeled dextrans with 0 mg/mL (■), 5 mg/mL (●), 10 mg/mL (▲), 20 mg/mL (▼) and 30 mg/mL (◆) of RRL.

Table 5.2: Rate constant for 10 kDa and 20 kDa FITC labeled dextrans transport through nuclear membrane of A549 cells with different concentrations of RRL.

Concentration of RRL in mg/mL	Rate constant of nuclear transport for 10 kDa Dextran molecules (s^{-1})	Rate constant of nuclear transport for 20 kDa Dextran molecules (s^{-1})
0	0.031 ± 0.009	0.012 ± 0.004
5	0.040 ± 0.008	0.018 ± 0.007
10	0.07 ± 0.03	0.021 ± 0.004
20	0.09 ± 0.04	0.024 ± 0.006
30	0.11 ± 0.06	0.04 ± 0.01

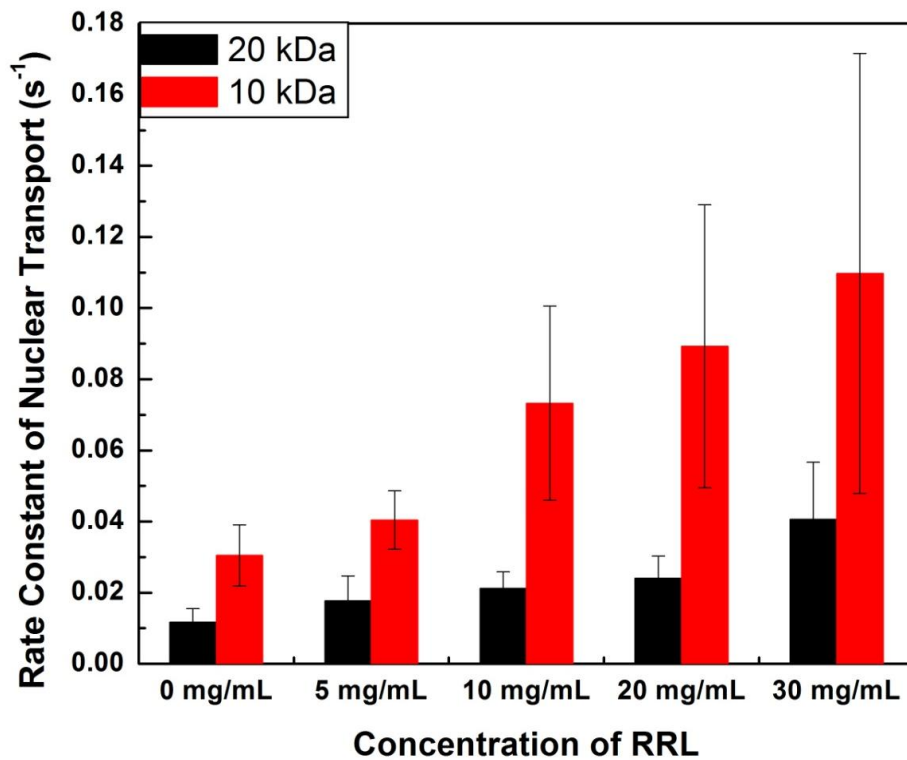


Figure 5.4: The average transport rate constant values are shown with spread of the rates gained with 10 kDa and 20 kDa dextran molecules.

5.4.2. PCR Products

PCR products are run in 2% agarose gel in electrophoresis and the DNA bands are visualized under Biorad digital gel documentation system (Biorad Gel Doc XR). The PCR protocol is optimized with respect to the GC content present in the primer sequences. The distance that the DNA fragments migrate in the agarose gel is proportional to its size. So, we used 1 kb DNA Ladder (or DNA size marker) which is a mixture of fragments of known sizes in one well, determine how far each fragments moved and that allows us to find out the length of other DNA fragments on the gel. The PCR results are illustrated in Figure 5.5 and the PCR products are marked with arrow lines. The gel results shows the PCR products are produced with the desired size without any cross contamination.

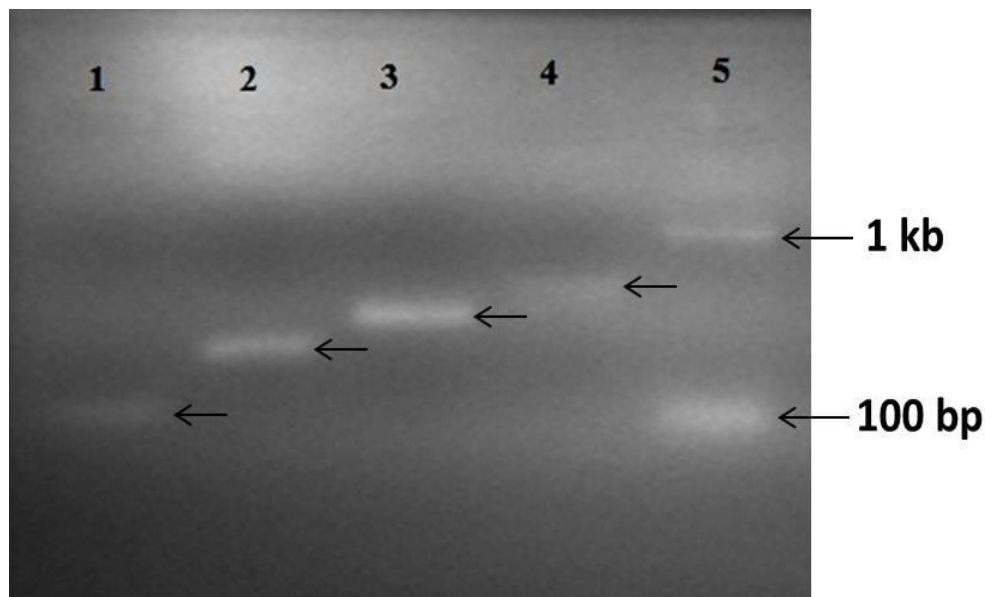


Figure 5.5: Gel documentation image of agarose gel with PCR products. 1 kb ladder is added in lane 5. Lane 1 – 4 contains PCR amplified DNAs of length 113 bp, 304 bp, 480 bp and 750 bp.

5.4.3. DNA Transport through Nuclear Membranes

Linear DNA fragments of various sizes obtained from the PCR technique are labeled with Fluorescein dye for microscopic examination. The confocal microscopy set up is optimized using appropriate filters suitable for fluorescence emission at 514 nm before carrying out the study. In the experiment, nuclear transport of fluorescently labeled DNA base pairs are examined in

digitonin permeabilized cells under transient conditions. Transport assays are carried out in the presence (+RRL) or absence (-RRL) of RRL as a source of cytosolic factors. The concentration of protein present in RRL employed in study is ~ 40 mg/mL and 50% of the transport solution is RRL.

Time lapse images from the equatorial plane of the nucleus are acquired at intervals of 2.5 seconds after the injection of import mixture containing 1 μ M solution of Fluorescein labeled DNA to the cells. Figures 5.6 and 5.7 are confocal cross sectional images after addition of import mixture having DNA fragments having 113 bp, 304 bp, 480 bp, 750 bp and 1000 bp of respectively, but with and without the presence of RRL in the transport solution. It is observed that the 113 bp DNA is accumulated strongly in nucleolus. Diffuse staining is observed throughout the rest of the nucleus, and the fluorescence becomes almost uniform in nucleus. The 304 bp DNA distributed evenly inside the nucleus. This is true for both the cases, in the presence of RRL and absence of RRL. Nuclear accumulation of the DNA is higher when RRL is present. 480 bp and 750 bp DNA exhibited binding to the nuclear membrane, and showed less frequent staining in the nucleus in absence of RRL. Nuclear accumulation of 480 bp and 750 bp DNAs increased with the presence of RRL but to a lesser extent. The 1 kb DNA sample had no DNA entry into the nuclei even with the presence of RRL.

The time lapse images are further analyzed as discussed earlier to quantify the rate of nuclear transport. In figure 5.8 we plot the normalized integrated nuclear fluorescence corresponding to each of the above DNA base pairs as a function of time. The graphs contain representative plots for both the cases, studies carried out in the presence of RRL (figure 5.8 A) and in the absence of RRL (figure 5.8 B). The rate constants of transport are extracted from this graph with the help of best fitting to a first order kinetic function as described in chapter 3.

A quantitative analysis of the images in figure 5.6 and 5.7 are done on 15 – 20 nuclei for each DNA base pairs. In figure 5.9 we compare the rate constants of nuclear import in presence of RRL to that in absence of RRL for all the 4 sizes of DNA. The dark lines represent the spread in rate constants among the nuclei studied. Table 5.3 gives the average rate constants as indicated in the figure along with the spread.

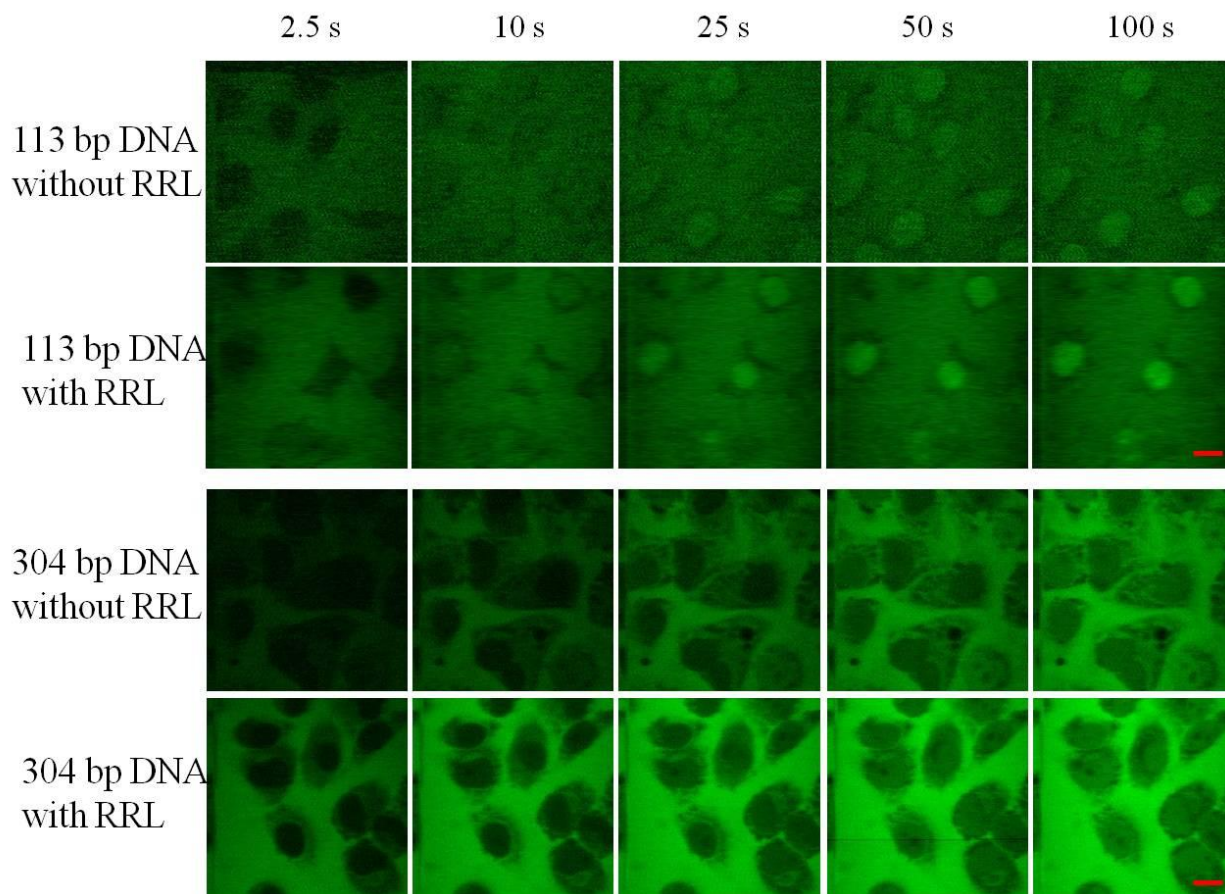


Figure 5.6: Confocal Time lapse images of A549 cell nucleus after the addition of 113 bp and 304 bp of DNA in digitonin permeabilized cells at 37°C with and without RRL. Scale bar – 10 μm .

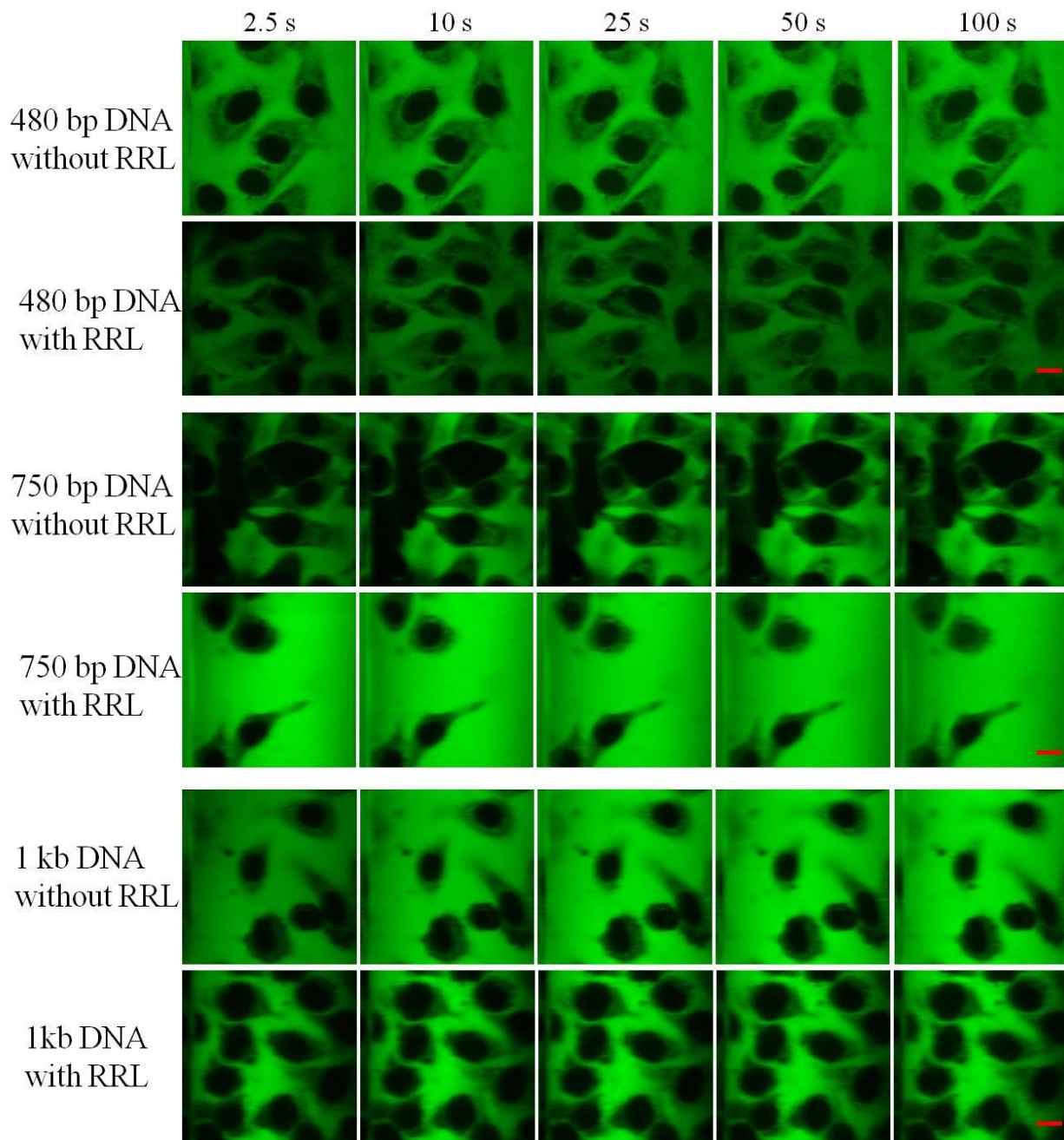


Figure 5.7: Confocal Time lapse images of A549 cell nucleus after the addition of 480 bp, 750 bp and 1000 bp of DNA in digitonin permeabilized cells with and without RRL. Scale bar – 10 μ m.

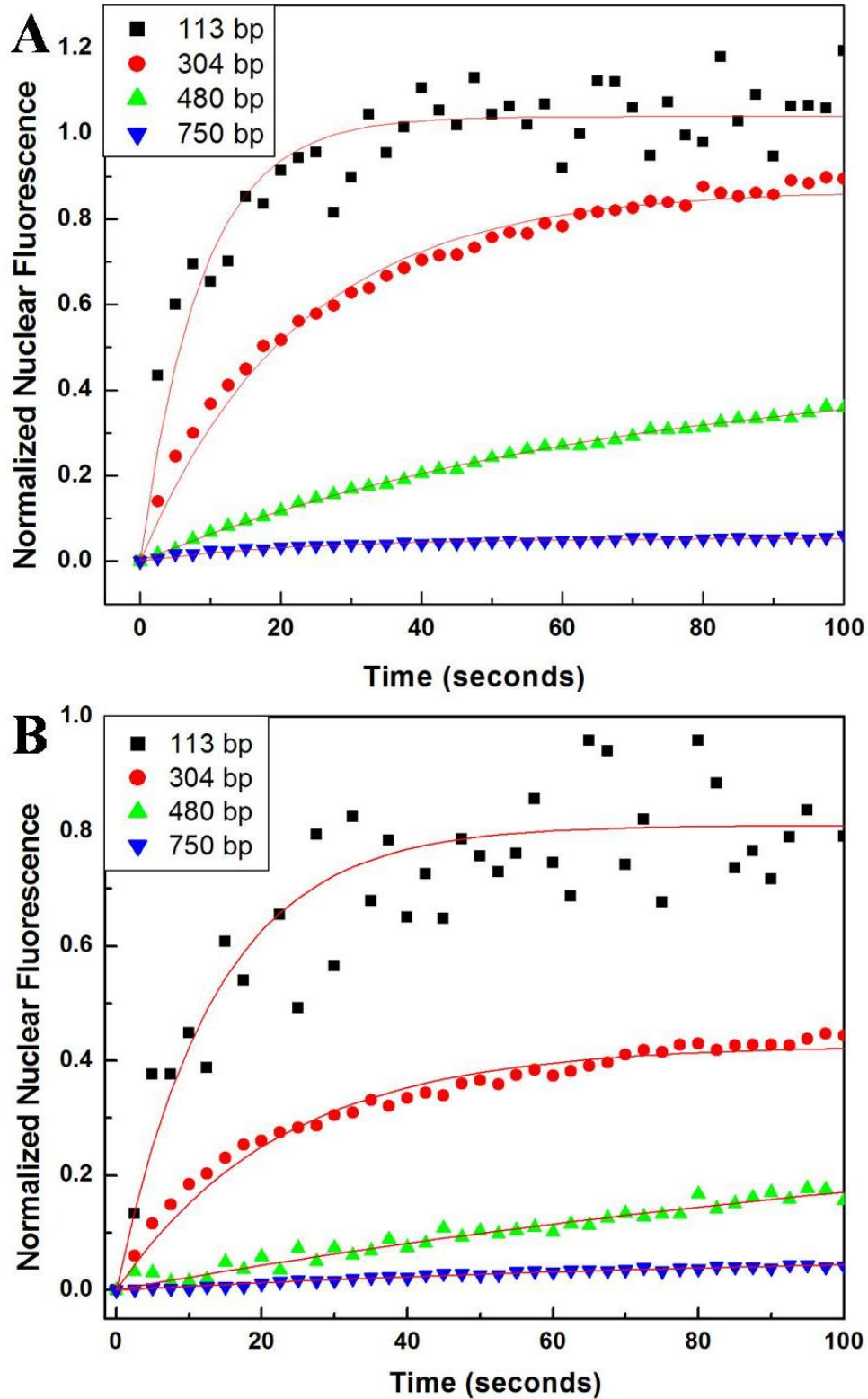


Figure 5.8: Normalized nuclear fluorescence versus time for the transport of different sizes of DNA fragments with the presence of RRL (A) and absence of RRL (B).

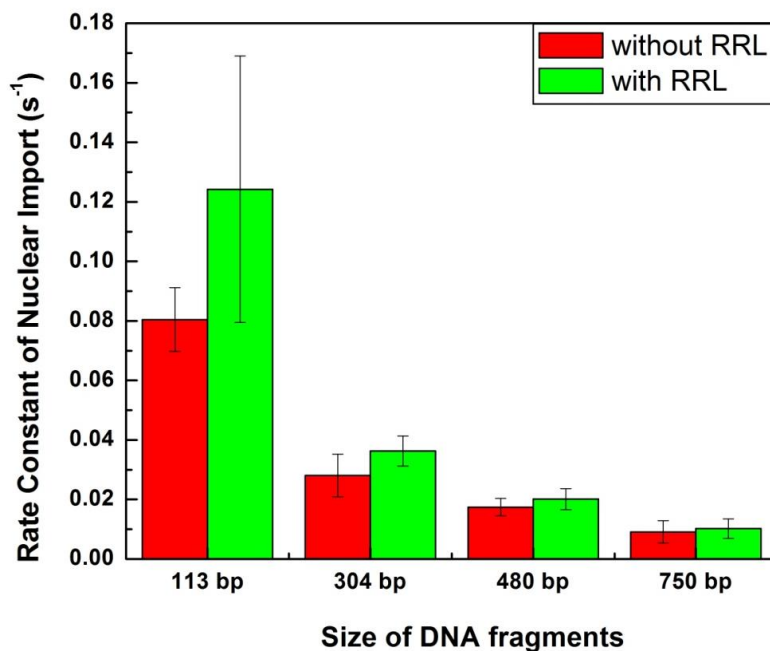


Figure 5.9: Effect of DNA size on nuclear accumulation in digitonin permeabilized cells with and without RRL for the sizes of 113 bp, 310 bp, 480 bp and 750 bp.

Table 5.3: Percentage increase in rate constant of transport of different sizes of DNA fragments through A549 cell nuclear membranes. Percentage increase in rate constants in the presence of RRL is also given.

Size of DNA Fragments	Rate constant values of nuclear import in absence of RRL	Rate constant values of nuclear import in presence of RRL	% of increase in nuclear import in the presence of RRL
113 bp	0.08 ± 0.01	0.12 ± 0.04	54 %
304 bp	0.028 ± 0.007	0.036 ± 0.005	29 %
480 bp	0.017 ± 0.003	0.02 ± 0.004	15 %
750 bp	0.009 ± 0.003	0.01 ± 0.003	13 %

5.5. DISCUSSIONS

One of the commonly used techniques in gene therapy is to use a non-viral carrier to import genes to the nucleus (Deng *et al.*, 2013, Escriou *et al.*, 1998). Though having many advantages, the use of non-viral delivery systems in human gene transfer is limited by poor transfection efficiencies. This is largely due to the inability of genes to translocate across the nuclear pore complexes. It is in this context that we studied and reported the transport rates of dextran molecules through the nuclear pore complex, in chapter 5. In order to evaluate the influence of environmental factors on nuclear transport, we looked at the effect of RRL on the nuclear uptake of this model drug and found that the transport rates are significantly enhanced in the presence of RRL. The nuclear transport rates of dextran molecules in digitonin permeabilized cells depend on the concentration of RRL present in the import mixture. This dependence is more pronounced in the case of 10 kDa dextran molecules than in the case of 20 kDa molecules. For 10 kDa dextran molecules the nuclear transport rate increases from a value of 0.03 s^{-1} in the absence of RRL to 0.04 s^{-1} with 12.5% (5 mg/mL) of RRL and to 0.11 with 75% (30 mg/mL) of RRL. For 20 kDa dextran this increase is from 0.018 s^{-1} for 5 mg/mL RRL to 0.04 s^{-1} for 30 mg/mL RRL. This dependence of biomolecular transport through nuclear pore complexes on the concentration of RRL present in the import mixture is not thoroughly examined so far in the literature. RRL is a protein extract solution similar to the one normally found in the cytoplasm of eukaryotic cells. Cell free rabbit reticulocyte lysate has been used extensively to elucidate the mechanisms of mammalian translation, co-translational modifications, post translational modifications and translocation of proteins. Further studies are needed to ascertain the mechanism of this enhanced transport rates of biomolecules in the presence of RRL, but as an intelligent first guess we may attribute this dependence to the transport receptors present in RRL. RRL contains transport receptors such as importin β which binds to the FG repeats due to hydrophobic interactions and help in the active transport. It is possible that this ‘opening up’ for active transport has a positive effect on the transport of passive molecules as well. It was shown recently that negative importin β , which normally plays the role of inhibitor to the active transport, also adversely affects passive transport. In the same fashion, it is quite possible that importin β favorably influence the passive nuclear transport. Studies are currently being planned by the group to examine this dependence, but are not included in this thesis.

There have been many studies on the nuclear transport of proteins and RNAs in the literature (Schutz *et al.*, 2014, Twyffels *et al.*, 2014, Fraser *et al.*, 2014, Huet *et al.*, 2010, Hardeland & Hurt, 2006). However, transport of DNA, a potential candidate in non-viral gene delivery strategies has not received much attention. It is known that DNA fragments having only a few base pairs can be transported to the nucleus through passive diffusion, but the kinetics of this transport is not examined so far (Ludtke *et al.*, 1999, Wilson *et al.*, 1999). In this work we studied the nuclear import of different DNA fragments using time lapse confocal microscopy and determined the rate constants of transport. It is observed that the DNA can indeed enter intact nuclei passively and that the diffusion constants critically depend on the number of DNA base pairs. DNA fragments having 113 base pairs are readily transported to the nucleus with a rate constant of 0.1 s^{-1} . DNA fragments having base pairs upto 750 are diffuses to the nuclei but with a much slower rate of 0.01 s^{-1} and with saturation stepping in after 5% of molecules are transported at 100 s. Previously it was reported that only DNA fragments having base pairs of up to 310 bp enter the nuclei through passive diffusion (Ludtke *et al.*, 1999). This under estimation is probably made in the absence of time lapse analysis of the rates of diffusion.

If we compare the nuclear transport rates of DNA fragments with that of dextran molecules of similar molecular weight, it can be seen that in general the rates are lower for the DNA. There is also some difference in the distribution of DNA base pairs of different molecular weight inside the nucleus as detailed in the results section, and as observed previously (Mearini *et al.*, 2004, Etheridge *et al.*, 2014). In comparison, the dextran molecules are distributed uniformly inside the nucleus regardless of its size.

There has been an attempt to enhance the nuclear uptake of DNA and to realize the potential in gene transfer (Hebert, 2003, Escriou *et al.*, 2003). The common strategy employed in these studies is to attach an NLS (nuclear localization signal) molecule to the DNA so that the DNA can enter the nuclei in an active transport process. An enhanced nuclear uptake of covalently bound NLS-DNA was observed by Hebert (Hebert, 2003). However, another report suggests that the covalently bound NLS-DNA do not show an enhanced transport, but only an enhanced expression (Hagstrom *et al.*, 1997). In another report it has been shown that can enhance the nuclear uptake of DNA.

Hagstrom *et al.*, studied the nuclear transport of fluorescently labeled DNA in digitonin permeabilized cells (Hagstrom *et al.*, 1997). They concluded that DNA nuclear entry is energy dependent and occurred via the nuclear pore complex, but contrary to the mechanism of nuclear transport for other macromolecules like proteins and dextrans, it did not require the addition of soluble cytoplasmic factors. In a study conducted on digitonin permeabilized HeLa cell nucleus, Hagstrom *et al.*, conclude that the RNA present in the cytoplasmic factors can react with 932 bp DNA and reduce the rate of nuclear import. Another work predicts that cytosolic extracts containing both DNA binding proteins and the NLS-dependent import machinery are essential for nuclear import of plasmid DNA molecules (Wilson *et al.*, 1999). They propose that the nuclear transport of plasmid DNA in digitonin permeabilized cells requires both cytoplasmic factors and specific DNA sequences.

In this work, we find that linear double stranded λ DNA fragments having up to 750 base pairs enter the intact nucleus via passive diffusion, even in the absence of cytosolic extracts. Further, based on the results of our study on dextran molecules, we checked the effect of rabbit reticulocyte lysate as cytoplasmic factor in nuclear import of linear double stranded DNA. We analyzed the effect of RRL in nuclear transport by determining the transport rate of different sizes of DNAs with 50% RRL (20 mg/mL) in import mixture. We find that RRL is indeed helpful in enhancing the nuclear transport rates of linear double stranded DNA in digitonin permeabilized A549 cells. An increase of around 50% is seen in the transport rates of small size DNA fragment of 113 bp. In case of larger molecule like 750 bp size DNA we observe around 10% increases in transport rate. Thus, it is seen that cytoplasmic factors/ rabbit reticulocyte lysate is an important factor in the nuclear import of DNA. However this result is in contradiction to that predicted by Hagstrom *et al.*, and in agreement with that reported by Wilson *et al.* In our studies we looked at the effect of RRL that is dialyzed overnight on the nuclear transport buffer. The dialysis process can remove lower molecular size component such as RNA and thus the above interaction may not be a possibility in our studies. In addition to that RRL helps in maintaining the integrity of nuclear membranes.

Our study showed that linear DNA of size ≥ 1 kb is not transported into the nucleus by a passive diffusion process even in the presence of RRL. This may be because larger DNA molecules are liable to be deposited outside the nucleus because of its greater binding to

cytoplasmic elements. A critical ratio of DNA binding sites inside and outside the nucleus could determine whether or not nuclear transport will occur. Another reason is that a very long piece of DNA would be more likely to bind several pores, inhibiting import. The distance between nuclear pores varies with cell type and metabolic activity. The fact that the length of the DNA is larger than the length of the pores could also be a factor in this (Riviere *et al.*, 2010, Hindley *et al.*, 2007, Mearini *et al.*, 2004).

CHAPTER SIX

FAST DETECTION AND IMAGING OF GOLD NANOPARTICLES USING LASER SCANNING PHOTOTHERMAL MICROSCOPY

6.1. INTRODUCTION

In this thesis we have employed confocal fluorescence microscopy to study biomolecular transport through nuclear membranes. Confocal fluorescence microscopy has many advantages over conventional microscopic techniques. Indeed, it is one of the most vital techniques in biological systems (Robinson, 2001; Pawley, 1995; Xi *et al.*, 2007; Matsumoto, 1993). In confocal fluorescence microscopy chemical selectivity is achieved by labeling the molecules of interest with a fluorescent dye. These fluorophores can be easily attached to biomolecules and since the fluorescence emission is Stoke shifted from that of the exciting laser wavelength high signal to noise ratio is achieved in imaging. The confocal detection scheme provides for dimensional sectioning capability and the technique can be used effectively to monitor a cross section of the cell as a function of time. Further, the laser scanning technique employed in this study allows for fast acquisition of images. Though confocal fluorescence microscopy has many advantages, the inherent instability and photo bleaching of dye labels under laser excitation precludes the use of this technique in observing biomolecular processes for long duration. A long period observation is important in many experimental situations, especially in studies involving tracking of biomolecular movement in cytoplasm or biomolecular transport between cytoplasm and the nucleus. In fact, photo-bleaching of the dye label was one of the major challenges we faced in this work. This has prompted us to look at and develop alternative imaging techniques suitable for experiments requiring long period of observation. Different label free methods of imaging, for example, based on coherent Raman microscopy have been developed to circumvent this limitation of fluorescence microscopy (Nandakumar *et al.*, 2009; Volkmer *et al.*, 2009; Freudiger *et al.*, 2008). Though promising, these techniques involve complex and challenging experimental set ups and are not widely popular. There is a continued interest in developing new photo-stable labels as well as simple microscopic techniques that will allow fast scanning and

image acquisition. In this final chapter we report on our attempt to develop a laser scanning photothermal microscope that can detect and image gold nanoparticles, a potential photo stable label for biological imaging.

Gold nanoparticles have attracted wide interest recently and are studied from the point of view of applications in labeling, sensing and imaging (Murphy *et al.*, 2008; Jain *et al.*, 2008). Gold nanoparticles in small percentages are biocompatible and can be used with ease to bind to specific molecular targets (Levy *et al.*, 2010). They are highly photostable and chemically inert and could provide a potential alternative label if suitable imaging techniques are developed. Imaging in the context of biological applications requires high signal to noise ratio and faster frame rates considering the possibility of Brownian movement of biomolecules in live cells. In this chapter we describe the design and construction of a laser scanning photothermal microscope that can detect and image gold nanoparticles at fast time scales. The laser scanning method employed by us allows fast image acquisition at 80 μ s pixel dwell time so that a 500 x 500 pixel image is acquired in 20 seconds.

The chapter starts with a brief note on the concept of photothermal imaging and discusses the methodologies employed in the construction of the microscope. Confocal images of 5 nm gold nanoparticles acquired at 80 μ s pixel dwell time are presented. Also in this section we demonstrate capabilities of the microscope by presenting images of a cell nucleus after the addition of gold nanoparticles in the cytoplasm.

6.2. PHOTOTHERMAL IMAGING

Detecting gold nanoparticles using optical microscopic techniques are challenging due to the small size of the particles. Optical microscopy doesn't have the resolution to resolve objects which are closer than Rayleigh limit ($\sim \lambda/2$). Gold nanoparticles are weakly fluorescent and it is difficult to detect them using fluorescence based techniques. As per Mie theory, the scattering cross section of particles having size less than the wavelength of light varies as the sixth power of radius while the absorption cross-section varies only as the third power of radius (Bohren & Huffman, 1998). Hence scattering based techniques typically result in low signal to noise ratio in imaging of gold nanoparticles having size less than ~ 50 nm. Hence absorption based

techniques such as photothermal microscopy would be more effective in detecting nanoparticles in this size range (Rajakarunanayake & Wickramasinghe, 1986; Lu *et al.*, 2010).

Gold nanoparticles have a large absorption cross-section when excited at its plasmon resonance and upon absorption most of the absorbed energy is released to the lattice through nonradiative relaxation. This nonradiative transfer of energy to the lattice will cause a temperature change, which in turn will result in a refractive index gradient around the particles. Photothermal microscopy makes use of this refractive index change to image gold nanoparticles. Photothermal spectroscopy is order of magnitude more sensitive than absorption spectroscopy and one can expect high signal to noise ratio in photothermal imaging. In experiments typically a pump-probe detection scheme is employed to sense the temperature change. The wavelength of the pump beam is so chosen as to coincide with the plasmon resonance absorption band of gold nanoparticles. A nonresonant probe beam is used to detect the temperature induced refractive index changes created by the pump beam. Photothermal microscopy is successfully employed by many groups to image gold nanoparticles (Gaiduk *et al.*, 2010; Zharov & Lapotko, 2003; Kulzer *et al.*, 2008; Berciaud *et al.*, 2006).

Photothermal imaging techniques discussed in the literature typically employ stage scanning to record a 2-dimensional image of gold nanoparticles (Gaiduk *et al.*, 2010a, Kulzer *et al.*, 2008, Boyer *et al.*, 2002, Zharov & Lapotko, 2003, Gaiduk *et al.*, 2010b, Lasne *et al.*, 2006). Stage scanning requires the longest time to acquire an image and specimen motion is often a challenge in this type of microscopy. Photothermal microscopes reported so far have large integration times of the order of milliseconds. Often molecules inside biological specimens are moving or changing dynamically at rates incompatible with the slow scan rates of these microscopes. Developing a microscope capable of fast imaging could help in such studies, especially in experiments aimed at tracking of biomolecular movement. In the present work we employed a galvanometric mirror scanner to raster scan the pump and probe beam over the sample and to acquire the images at fast time scales.

6.3. MATERIALS

The details of the main components used for the photothermal microscope construction and samples used for imaging are given below. More information about Dichroic mirror, Galvanometric mirror scanner, Data acquisition card, LabVIEW software imaging program, Inverted microscope and Optical mountings is given in the materials section of chapter 2.

Lasers

We have used diode pumped solid state laser (Model: Verdi G-5, Coherent Inc., USA) as a pump laser source in photothermal microscopy set up. Verdi G-5 is a family of optically pumped semiconductor lasers and diode-pumped solid-state (DPSS) lasers with CW power up to 5 W at 532 nm. HeNe laser (Model: 25-LHP-151-230, CVI Melles Griot, USA) with the wavelength of 632 nm is used as a probe laser.

Acousto Optic Modulator

An acousto-optic modulator (AOM) is a device which can be used for controlling the power, frequency or spatial direction of a laser beam with an electrical drive signal. It is based on the acousto-optic effect, i.e. the change of the refractive index by the oscillating mechanical pressure of a sound wave. The key component of an AOM is a transparent crystal through which the light propagates. A piezoelectric transducer attached to the crystal is used to excite a sound wave. We have used acousto optic modulator (Model: 1205C-1, Isomet Corporation, USA) for modulating the pump laser beam with a particular frequency.

Lock in Amplifier

To discern the pump induced variation in the scattered probe beam we used 200 MHz dual phase lock in amplifier (Model: SR-844, Stanford Research Systems Inc., USA). The SR844 model is the widest bandwidth lock-in amplifier. It provides uncompromised performance with a frequency range of 25 kHz to 200 MHz and up to 80 dB of drift-free dynamic reserve. Time constants values provided are from 100 μ s to 30 ks.

Filters

Band pass laser line interference filter with the specification of 632.8 ± 10 nm (Model: F10-632.8-4-25.0M, CVI Melles Griot, USA) is used to block the light at wavelengths different from 632.8 nm. This bandpass filter is used in front of the photo-receiver in order to allow only the probe laser beam.

Balanced Photo-receiver

The New Focus 2307-M large area adjustable gain balanced photodiode takes the pain out of aligning and re-aligning 400 – 1070 nm laser beams onto the photodetector. The Model 2307 is a general-purpose balanced photo-receiver with a large-area ‘Silicon’ photodetector. These receivers can be power-driven by battery or by an external ± 15 V power supply. The large area of the photodetector makes it easy to couple light from a variety of sources onto the detector without requiring precise optical alignment or focusing.

Gold Nanoparticles

We obtained Life Science starter kit (code: GCIKITLIFE) which contains 20 mL of 5 nm, 10 nm, 20 nm and 40 nm (Model: EM.GC – 5, EM.GC – 10, EM.GC – 20 and EM.GC – 40 respectively) gold nanoparticles from British Biocell International Limited, UK. A wide range of particle sizes can be used in size dependence study. This gold colloid starter packs provides a range of particle sizes to allow a comprehensive assessment, comprising 20 mL each of a selection of gold colloid. It can be conjugated to proteins and macromolecules as labels. Gold nanoparticles are being investigated as photothermal agents for in-vivo and in-vitro applications.

Spin Coating Unit

Spin coater is used to coat thin layer of gold nanoparticles solution on glass cover slips. Spin Coater (Model: HO-TH-05, Holmarc Optomechatronics Pvt. Ltd., India) is a dedicated tabletop system to spin coat small substrates well controlled spin process parameters. The spin head actuator is a precision DC servo motor with accurate speed and acceleration control. A vacuum chuck powered by oil-less vacuum pump holds the substrate at the spinning head.

6.4. EXPERIMENTAL METHODS

6.4.1. Construction of Laser Scanning Photothermal Microscope

The optical layout of laser scanning photothermal microscope is given in Figure 6.1. Components are mounted on standard post mounts fixed to an optical table with pneumatic isolator (RS 2000 series, Newport). Two independent laser beams are used in the experiment as pump and probe beams. A diode pumped solid state laser (Verdi G-5, Coherent) is used to provide the pump beam having a wavelength of 532 nm in the plasmon resonance band of the gold nanoparticles. The pump beam is modulated at high frequency by an acousto optic modulator (AOM, 1205C-1). A pump modulation frequency of 115 kHz is chosen considering the detector response time and noise background in the laboratory so as to provide maximum signal to noise ratio. The pump beam provides periodic heating of the gold nanoparticles, and the resulting refractive index change is monitored by a HeNe laser. Samples are mounted on an inverted microscope (IX 71, Olympus) equipped with a 60X (NA 1.25) objective. A dichroic mirror combines the pump and probe beams to a coaxial geometry and directs it to a set of scan mirrors (6215 M40) mounted on a heat sink. The coaxial pump and probe beams reflect off the two scan mirrors and are focused to a point source by the eyepiece lens on the conjugate plane of the microscope. Both the eyepiece and the scanning mirrors are mounted on micrometer mounts to facilitate alignment. The optics of the microscope relays the scanning spot to the specimen. The back scattered pump and probe beams return along the same pathway and are descanned by the scan mirrors before reaching the dichroic. The probe beam passes through the dichroic mirror while the pump beam is reflected off. The transmitted probe beam is further filtered by a bandpass interference filter (632 ± 10 nm) and is directed to a large area balanced photoreceiver (2307-M, New Focus). The balanced receiver helps to subtract the DC background and thus allow the lock in amplifier to be used in lower signal ranges without overloading lock in. Reference beam for the balanced receiver, supplied by the beam splitter BS1, is adjusted using a variable neutral density filter so as to give zero dc signals. The differential signal from the receiver is sent to a 200 MHz dual phase lock in amplifier (SR-844, Stanford Research Systems) to discern the pump induced variation in the scattered probe beam. The signal is detected by the lock-in amplifier with an integration time of 100 μ s. A data acquisition card (NI USB-6251) along with National Instruments LabVIEW software is used for acquiring the signals as well as

for controlling the scan mirrors. The program allows for varying the scan frequency and scan voltage. Scan frequencies of 25 Hz and 0.05 Hz respectively are used for the X and Y scan mirrors.

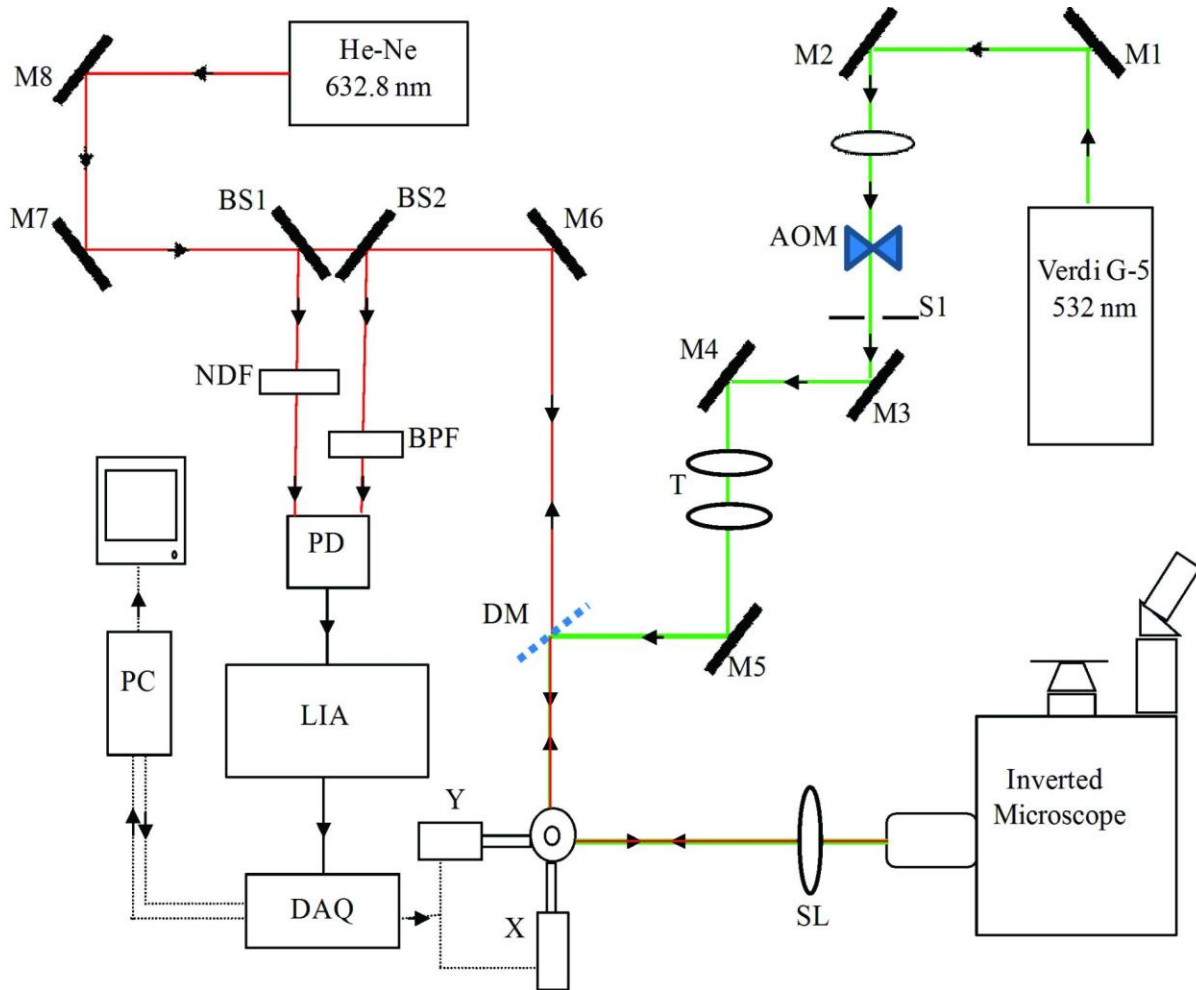


Figure 6.1: Optical layout of Laser Scanning Photothermal Microscope setup. M: Mirror, BS: Beam Splitter, BPF: Band Pass Filter, NDF: Neutral Density Filter, PD: Balanced Photo Receiver, LIA: Lock-in Amplifier, DAQ: Data Acquisition card, PC: Computer, DM: Dichroic Mirror, S1: Aperture, T: Telescope, AOM: Acousto Optic Modulator, SL: Scan Lens and X&Y: Scan Mirrors.

6.4.2. Sample Preparations for Imaging

Colloidal gold nanoparticles of 5 nm and 10 nm diameter obtained from British Bio International. The samples for microscopy are prepared by dilution (1:4) in ultra-pure water. Approximately 25 μL of the suspension is spin coated at 2000 rpm for 5 s, followed by drying at 4000 rpm for 90 s on the surface of a 22×22 mm cleaned cover glass slide. Gold nanoparticles solutions are sonicated for 30 minutes before spin coating so that a uniform thin layer is formed on the cover glass.

Glass cover slides are cleaned in several steps by sonication for 20 min in acetone, ethanol and in Milli-Q water. Experiments are performed in a cell (approx. 50 – 100 μL volume) made from petridish with 9 mm hole in the center. Gold nanoparticle coated cover glass slip is pasted with petridishes using the Press-to-Seal silicone isolator with adhesive of 9 mm diameter, 0.5 mm deep (Invitrogen code: P-24743). Photothermal imaging is carried out at the water-glass interface. Water has good thermal properties and is a natural photothermal medium for live cell imaging.

6.4.3. Photothermal Imaging of Gold Nanoparticles in Live Cell

A549 cells are cultured in DMEM medium supplemented with 10% bovine serum in a humidified atmosphere (95%) at 5% CO_2 and 37°C (detailed procedure of cell growth, permeabilization and time lapse imaging scheme is shown in Chapter 3). For photothermal imaging studies the cells are plated onto glass bottom petridishes to a confluence of 30 – 50% and permeabilized with digitonin with the concentration of 40 $\mu\text{g}/\text{mL}$ incubated for 5 minutes. The cells in growth chamber are then mounted in a microscope stage. 25 μL of colloidal gold nanoparticles are added into the permeabilized cells and the images are acquired in time lapse imaging scheme.

6.5. RESULTS AND DISCUSSION

6.5.1. Photothermal Imaging of 5 nm Gold Nanoparticles

Photothermal images are obtained for different sizes of gold nanoparticles in the size range of 40 nm to 5 nm. In figure. 6.2 (a) we depict the photothermal images of gold nanoparticles having a mean size of 5 nm. A clean area of the sample, free of any particles under normal microscope is chosen for imaging. While taking each image it is verified that the signal disappears when either of the beams is blocked thereby making sure that no spurious scattered image is detected. Pump and probe powers at the objective focus are 1.25 MW/cm^2 and 1 MW/cm^2 respectively. A 500×500 pixel image is acquired in 20 seconds corresponding to a pixel integration time of $80 \mu\text{s}$. Figure. 6.2 (b) depicts pseudo-3D image of a single gold nanoparticle with a diameter of ~ 5 nm. The figure shows a $2 \mu\text{m} \times 2 \mu\text{m}$ area of the sample with the photothermal signal strength as the height coordinate. The signal to noise ratio in the image is computed by taking the ratio of the photothermal peak intensity to the standard deviation of the random background fluctuations. Average signal to noise ratio for the particles shown in the image is 48. In figure. 6.2 (c) we have plotted the peak intensity distribution histogram for all particles in a 500×500 pixel area.

When the pixel integration time is reduced the signal strength also reduces accordingly. In order to detect the pump induced changes in the probe laser one has to employ lock in detection using lower signal range scales of the lock in amplifier. A major problem we faced in this experiment is the overloading of the lock in amplifier. The balanced receiver helps to subtract the DC background and allow the lock in amplifier to be used in lower signal ranges without overloading lock in amplifier.

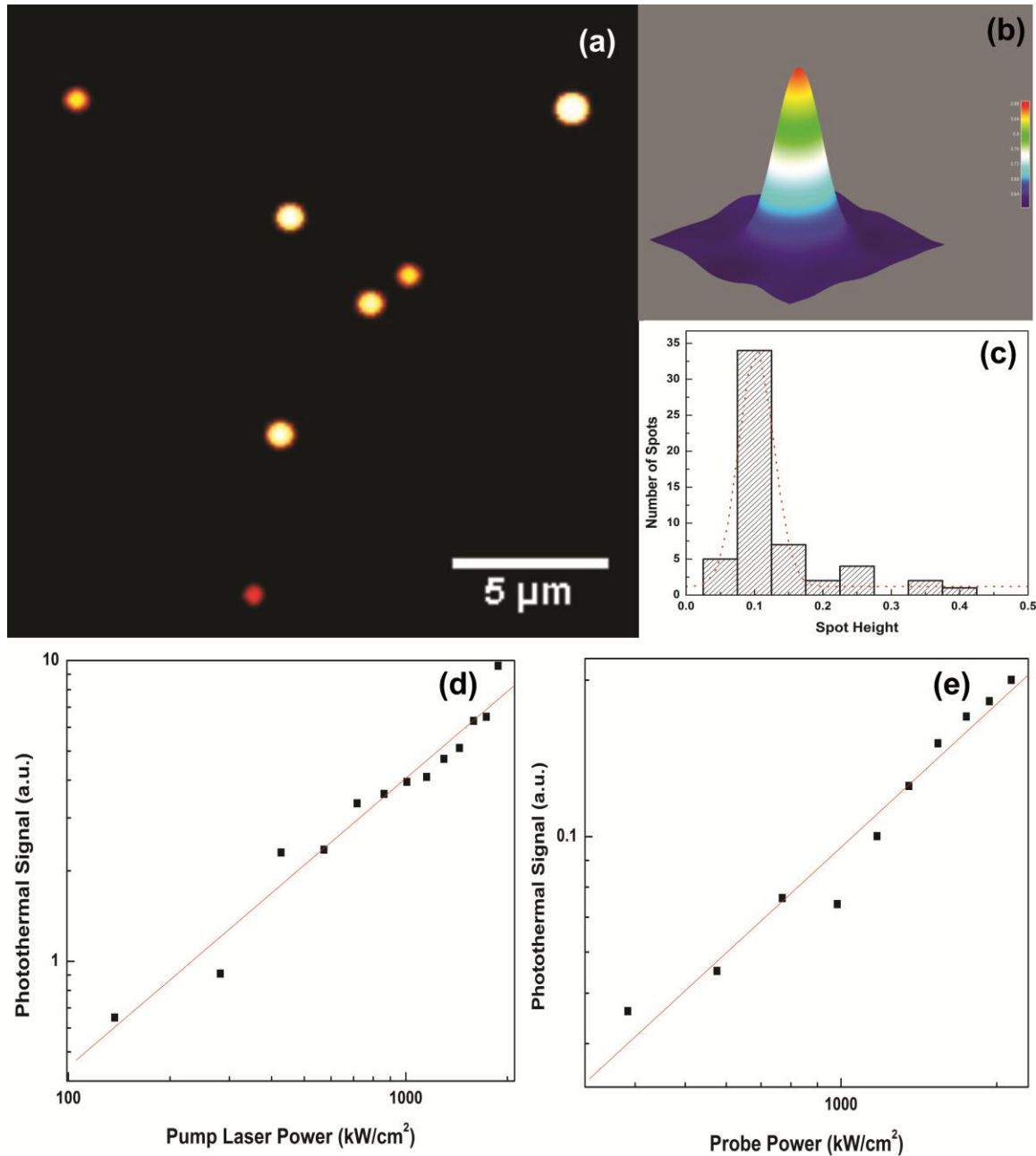


Figure 6.2: (a) Photothermal image of 5 nm gold nanoparticles coated on glass cover slip. Average signal to noise ratio in this image is 48. (b) Pseudo-3D image showing a single nanoparticle in an area of $2 \mu\text{m} \times 2 \mu\text{m}$. (c) Photothermal signal intensity distribution histogram of gold nanoparticles having average size of 5 nm. The full width at half maximum of the Gaussian fit is 0.05 corresponding to a percentage intensity distribution of 48%. (d) Variation of photothermal signal with pump laser power. (e) Variation of photothermal signal with probe laser power.

6.5.2. Photothermal Image of 10 nm and 5 nm Gold Nanoparticles in Same Sample

Further, in figure. 6.3 (a) we show the photothermal image of a sample containing two sets of gold nanoparticles having average diameters of 10 nm and 5 nm. The sample is prepared by spin coating a dilute mixture of gold nanoparticle of the two sizes on a glass slide. The image show two distinct classes of particles as indicated by the intensity distribution histogram plotted in figure. 6.3 (b). The ratio of the intensities at the maxima of the two distinct peaks is close to the photothermal intensity ratio of 8 expected for two particles of well-defined size 5 nm and 10 nm. Given the size distribution of the particles used in the study, this result is also in good qualitative correspondence with the expected cubic dependence of the photothermal signal on the particle radius.

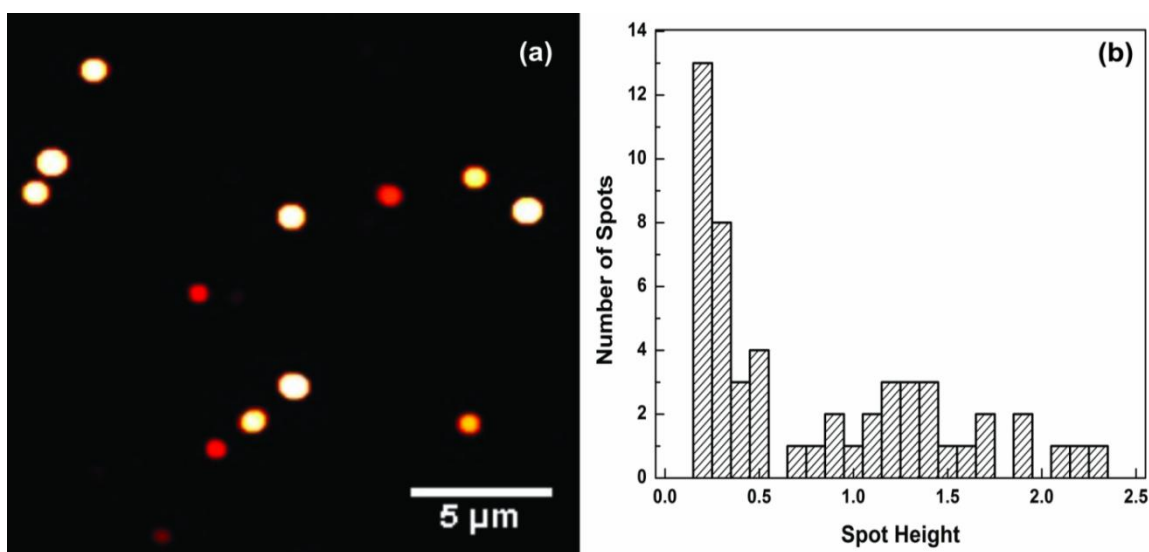


Figure 6.3: (a) Photothermal image of a sample containing two sizes of gold nanoparticles having average diameters of 10 nm and 5 nm. (b) Photothermal signal intensity distribution histogram of gold nanoparticles in the image.

6.5.3. Laser Power Dependence on Photothermal Signal

The photothermal signal strength can be approximated as (Gaiduk *et al.*, 2010)

$$S \approx \frac{1}{\pi\omega_0} n \frac{\partial n}{\partial T} \frac{1}{C_p\lambda^2\Omega} \frac{\sigma_{abs}}{A} P_{pump} P_{probe} \Delta t$$

Here n is the refractive index, T temperature, Ω is the angular frequency of the pump beam intensity modulation, A is the area of the focussed pump beam, ω_0 is the probe beam focal radius, C_p is the heat capacity per unit volume of the photothermal medium, λ and P_{probe} are the wavelength and power of the probe beam, Δt is the integration time, P_{pump} is the power of pump beam and σ_{abs} is the absorption cross-section of the nanoparticle. In figure 6.2 (d) and 6.2 (e) we plot the dependence of the photothermal signal strength on the pump and probe powers. The figure shows that the photothermal signal depends linearly on both the pump and probe powers and that the gold nanoparticles are not damaged at the pump powers used.

Photothermal signal strength in the image acquired with a particular integration time, and a given pump and probe powers is determined by the absorption cross section of the particle. Absorption crosssection of the particle in the size range studied here varies as the third power of radius. Hence in a particular image, the distribution of the photothermal signal intensities of different particles will mimic the volume distribution of the particles present. Figure. 6.2 (c). shows the photothermal intensity distribution histogram of the particles in the image along with a Gaussian fit. The full width at half maximum of the Gaussian fit is 0.05 corresponding to a percentage intensity distribution of 48%. This spread is in good qualitative correspondence with the specified size distribution of the gold nanoparticle (15% as per the manufacturer's specification) sample used. The monomodal distributions indicates that single gold particles are detected.

6.5.4. Modulation Frequency Dependence

Pump modulation frequency dependence on SNR of the photothermal image is shown in figure 6.4. The experiments are carried out at 115 kHz suitable for the detector used and noise levels in the lab. Photothermal images are obtained for different AOM modulation frequencies of 5 nm

gold nanoparticles coated on cover slip. The SNR is decreasing after 115 kHz primarily due to the response time of the detector.

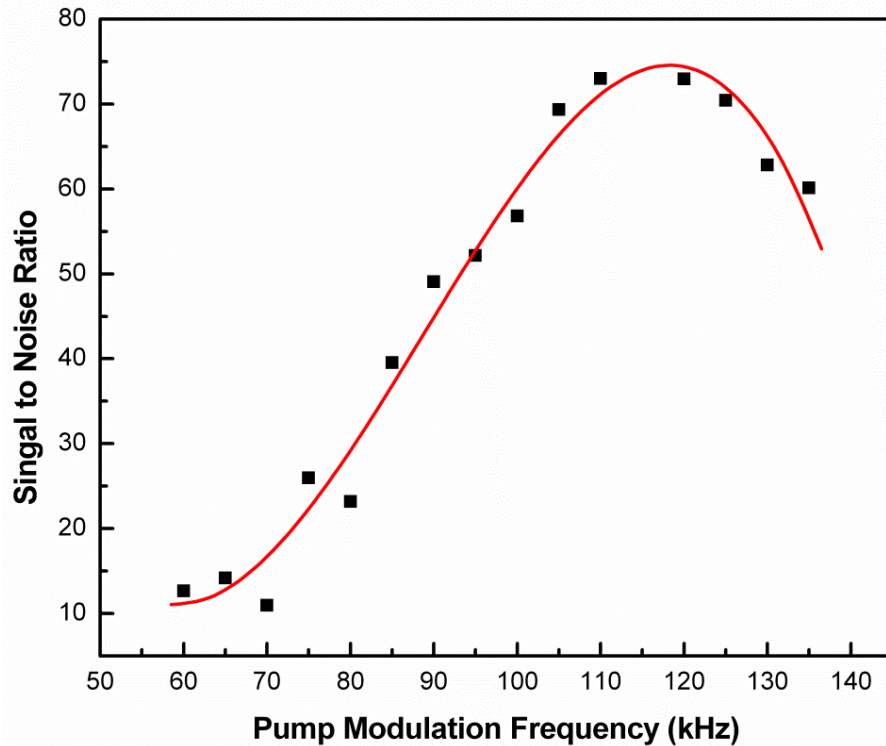


Figure 6.4: Dependence of pump modulation frequency on SNR of the photothermal image.

6.5.5. Size Dependence of the Photothermal Signal

To verify the size dependence of the photothermal signal and to obtain a calibration curve, we have imaged separate samples of gold nanoparticles having average particle sizes of 5 nm, 10 nm, 20 nm and 40 nm. Figure 6.5 shows the photothermal images and the respective intensity distribution histograms for different gold nanoparticle samples.

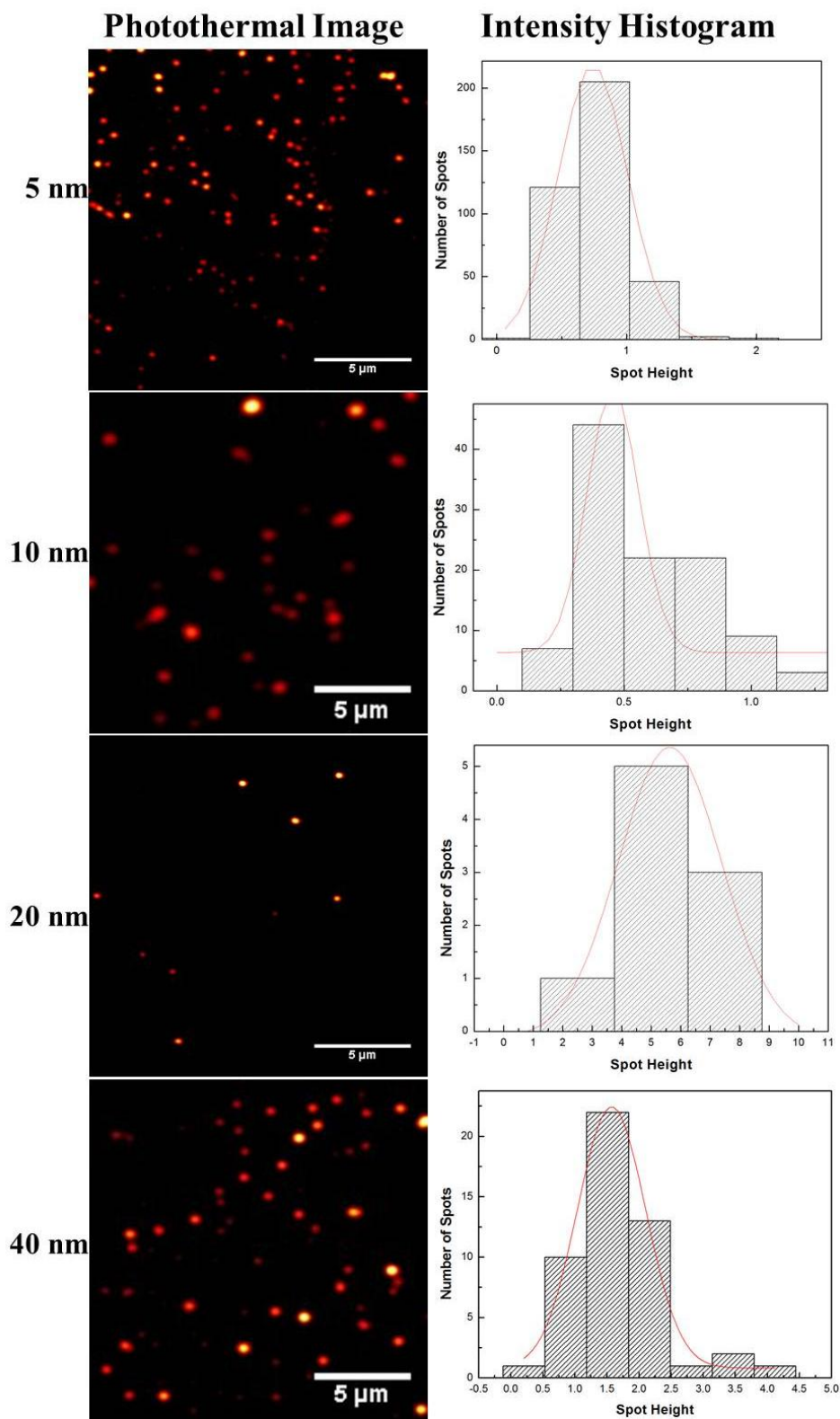


Figure 6.5: Photothermal image and its intensity distribution histograms for samples of gold nanoparticles having average particle sizes of 5 nm, 10 nm, 20 nm and 40 nm.

Imaging different samples with identical alignment conditions is challenging and we repeated the measurements many times to maximize the signal in each sample and to estimate the error in the measurements. It is not possible to image all sizes of gold nanoparticle samples at the same pump power without overloading the lock in amplifier. Hence images of each sample are taken at pump powers optimum for that particle size. Since the pump powers are different it is not possible to directly compare the images. Hence we plotted the intensity histograms for each size and normalized them to unit power so as to compare the signal values. The results of these measurements are shown in figure below, where we show the plot of normalized photothermal intensity versus average size of the particle. The error in the intensity values are as indicated. The size dependence of the photothermal intensity is shown in figure 6.6. The log-log plot of signal intensity against particle size show a slope of 2.7 close to the expected value of 3, with in error limits. All the images acquired for this size dependence study is taken with a pixel dwell time of 80 μ s.

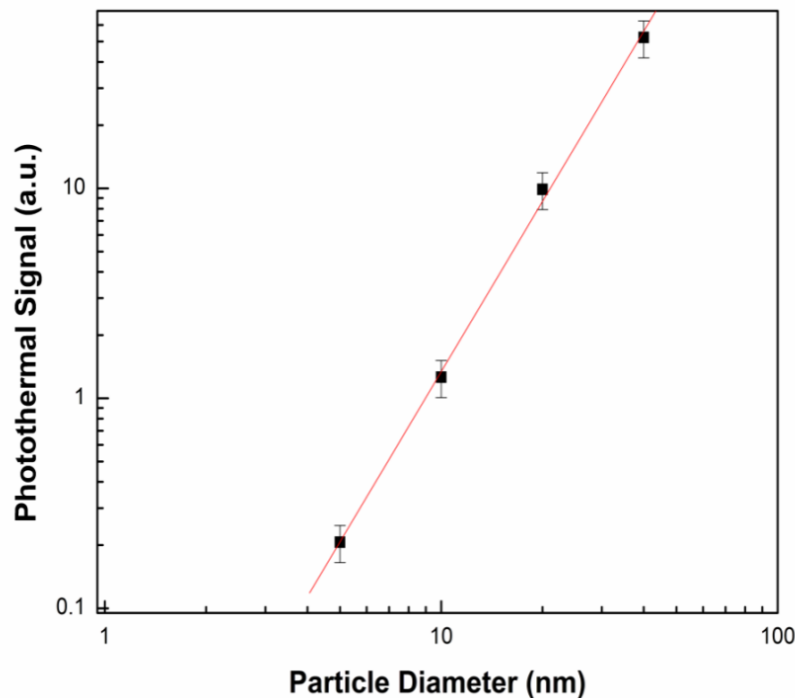


Figure 6.6: Log-log plot of photothermal signal intensity vs. particle size, showing a cubic dependence of the signal on particle size. The squares denote the measured photothermal signal strength and the continuous line is a straight line fit. The straight line has a slope of 2.7 close to the expected value of 3.

6.5.6. Potential in Live cell imaging

As mentioned in the introductory section gold nanoparticles are biocompatible and highly photostable and photothermal microscopy using gold nanoparticles has the potential to be a successful alternative imaging technique in biology. The primary challenge, however, is to develop the capability to image the fast moving molecules in a biological environment. For this it is important to have the ability to acquire high signal to ratio images at time scales which is comparable to the biomolecular movement. In this work, we would say that we have succeeded to an extent we are able to detect and image gold nanoparticles in an aqueous medium sandwiched between two cover slips. Further, to demonstrate the applicability of the technique in biological context, we replaced the dye labeled biomolecules in our study on nuclear transport with the gold nanoparticles, and recorded the images of the nucleus at fixed intervals after the addition of gold nanoparticles in cell system. A 250×250 pixel image is acquired in 5 seconds with the X-scanning frequency of the galvanometric scanner set at 50 Hz corresponding to a pixel dwell time of 80 μ s.

In figure 6.7 below, we show 6 confocal cross sectional images of the A549 cell nucleus at fixed time interval after the addition of an aqueous solution of 5 nm gold nanoparticles (concentration 5.00×10^{13} particles/mL) in the imaging chamber. Images taken after 10 minutes show a very clear image of the nuclear membrane with gold nanoparticles sticking to the membrane. A few particles are seen inside the nucleus also. With time the number of particles entering the nucleus increases and the image taken after 3 hours show almost uniform punctuate staining throughout the nucleus. Similar effects are seen with 10 nm gold nanoparticles (5.70×10^{12} particles/mL) also, but with lesser number of particles entering the nucleus (figure 6.8). When gold nanoparticles having an average diameter of 20 nm (7.00×10^{11} particles/mL) are added to the chamber and imaged we could see the nuclear membrane at all the times, but almost no staining is observed inside the nucleus even after 3 hours as shown in figure 6.9. This indicates that particles with 20 nm radius are not entering the nucleus.

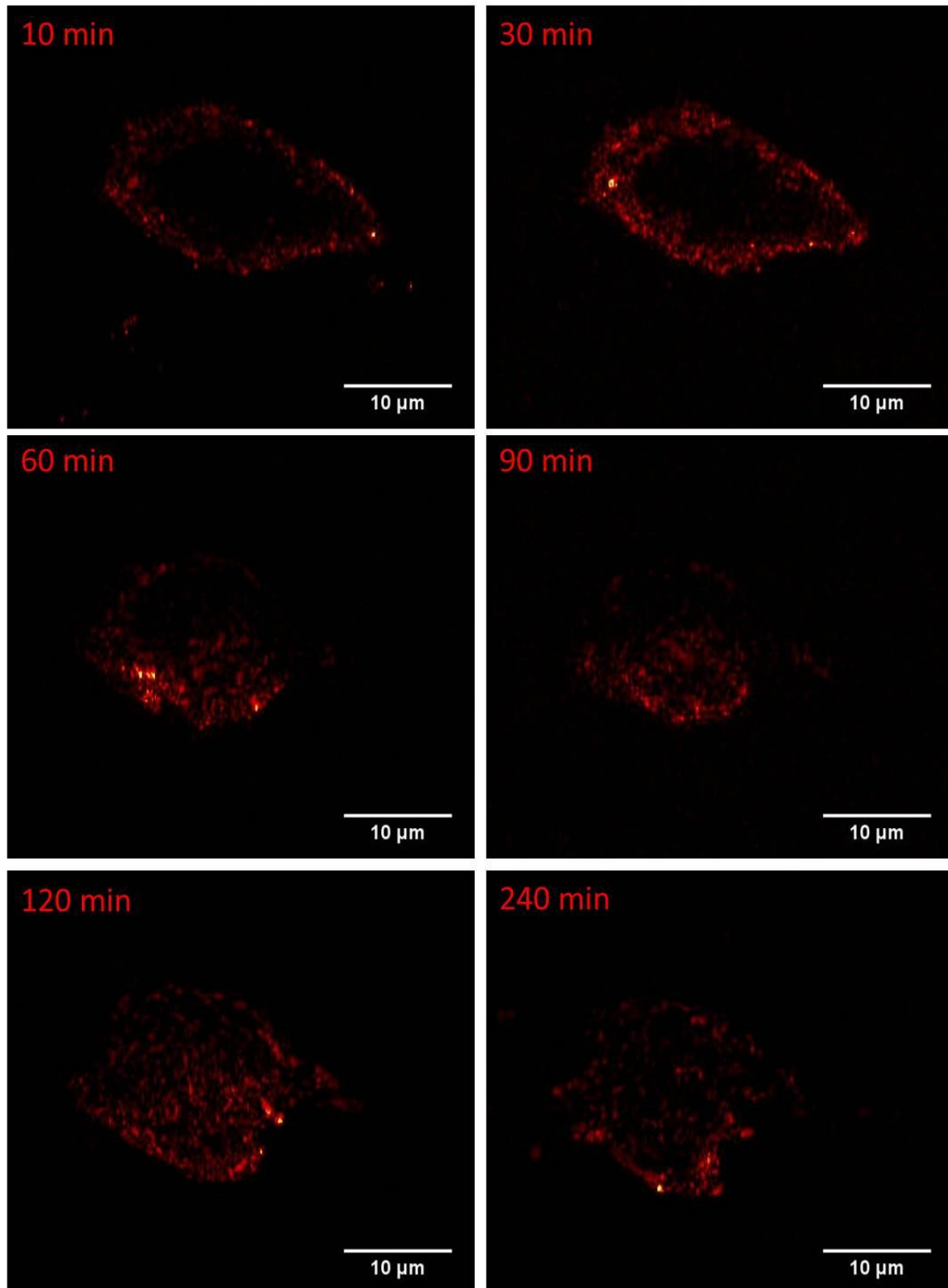


Figure 6.7: Time lapse images of 5 nm gold nanoparticles in live A549 cells. Image shows the diffusion of 5 nm gold nanoparticles to the cell nucleus with time.

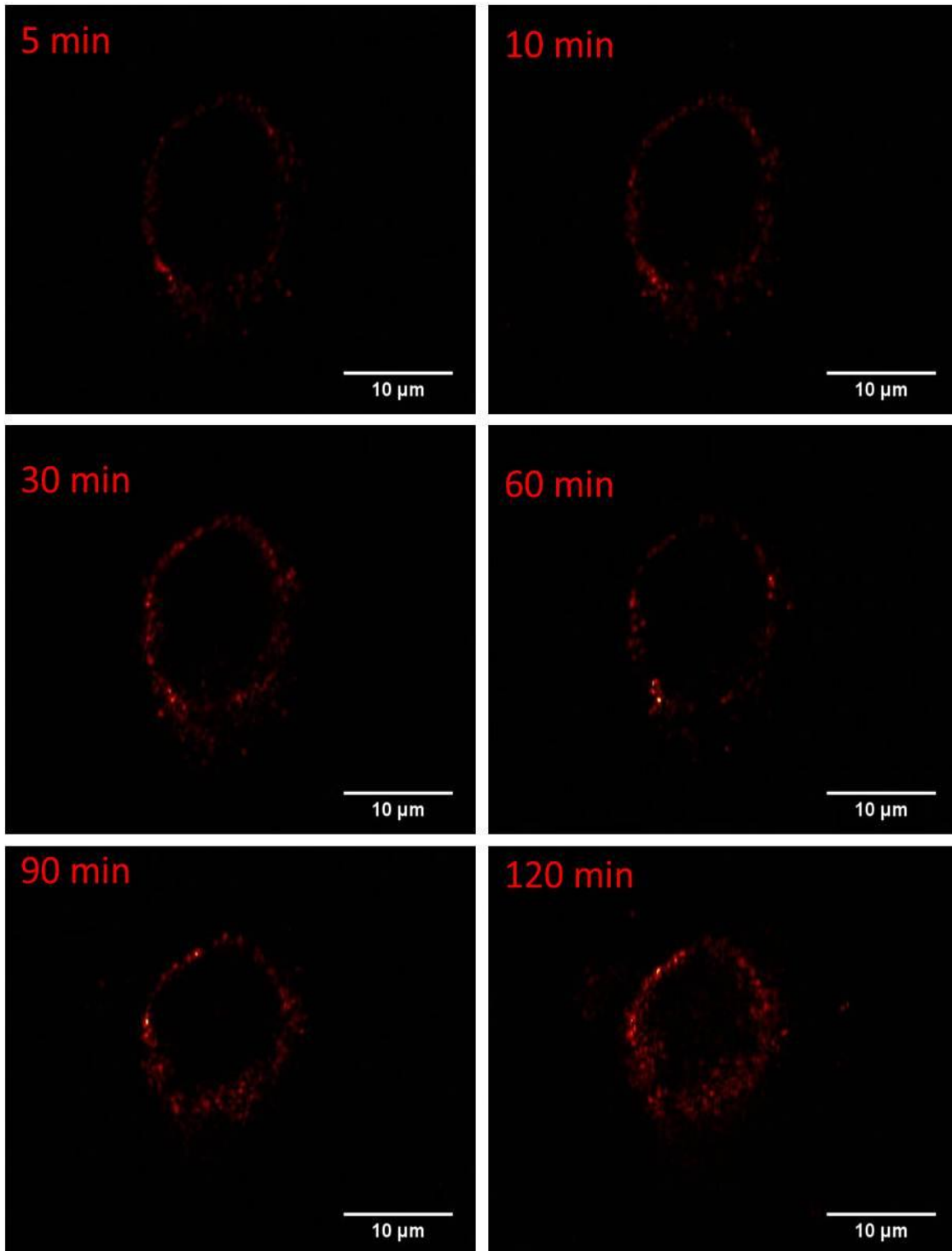


Figure 6.8: Time lapse images of 10 nm gold nanoparticles in live A549 cells. Image shows the diffusion of 10 nm gold nanoparticles to the cell nucleus with time. Gold nanoparticles are deposited more on the nuclear membranes and the number of particles that has entered the nucleus is smaller than that of 5 nm particles.

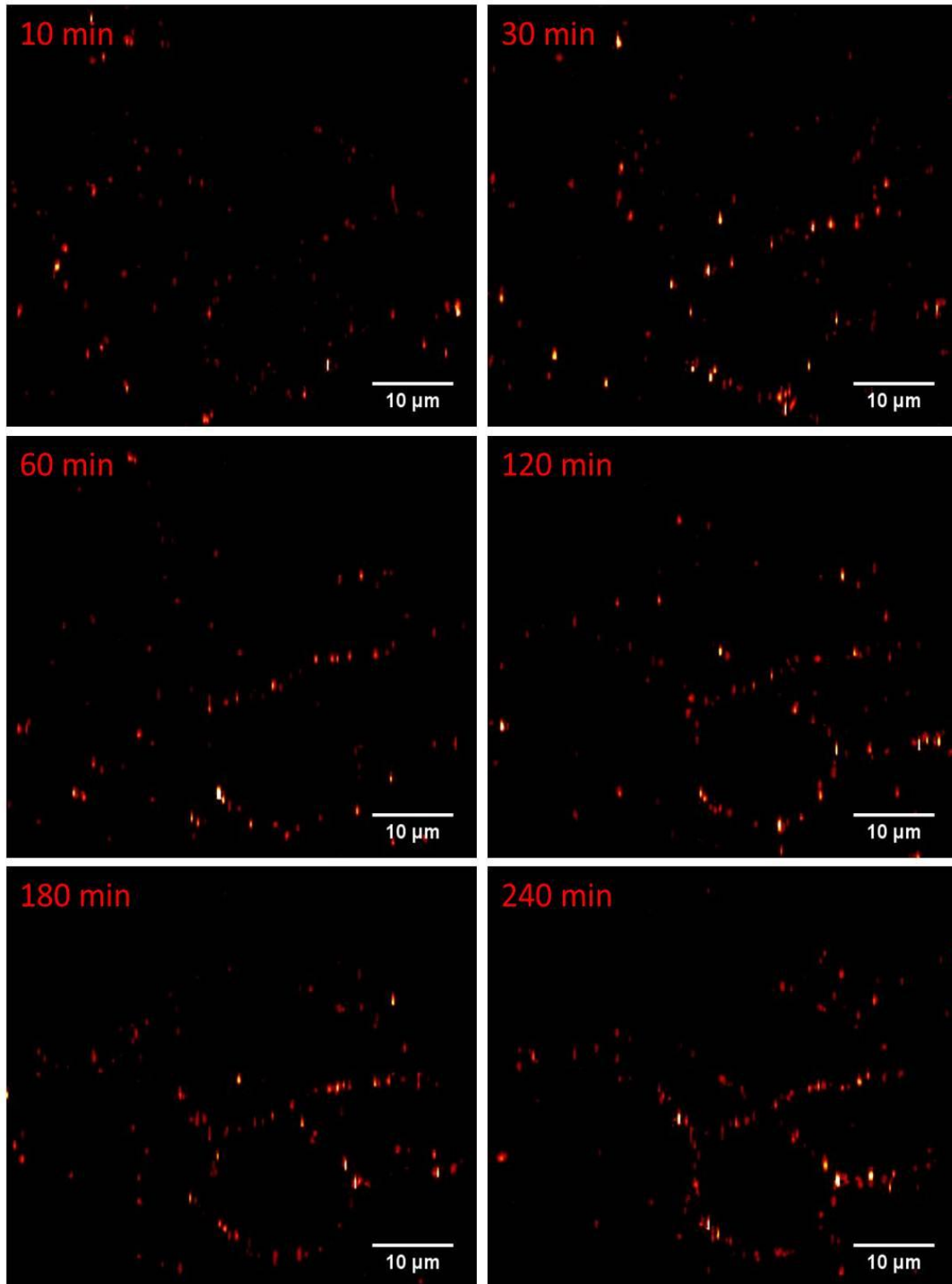


Figure 6.9: Time lapse images of 20 nm gold nanoparticles in live A549 cells. The images show that the gold nanoparticles are adsorbed on the nuclear membrane. No significant amount of gold nanoparticles has entered the nucleus during the time course of the experiment.

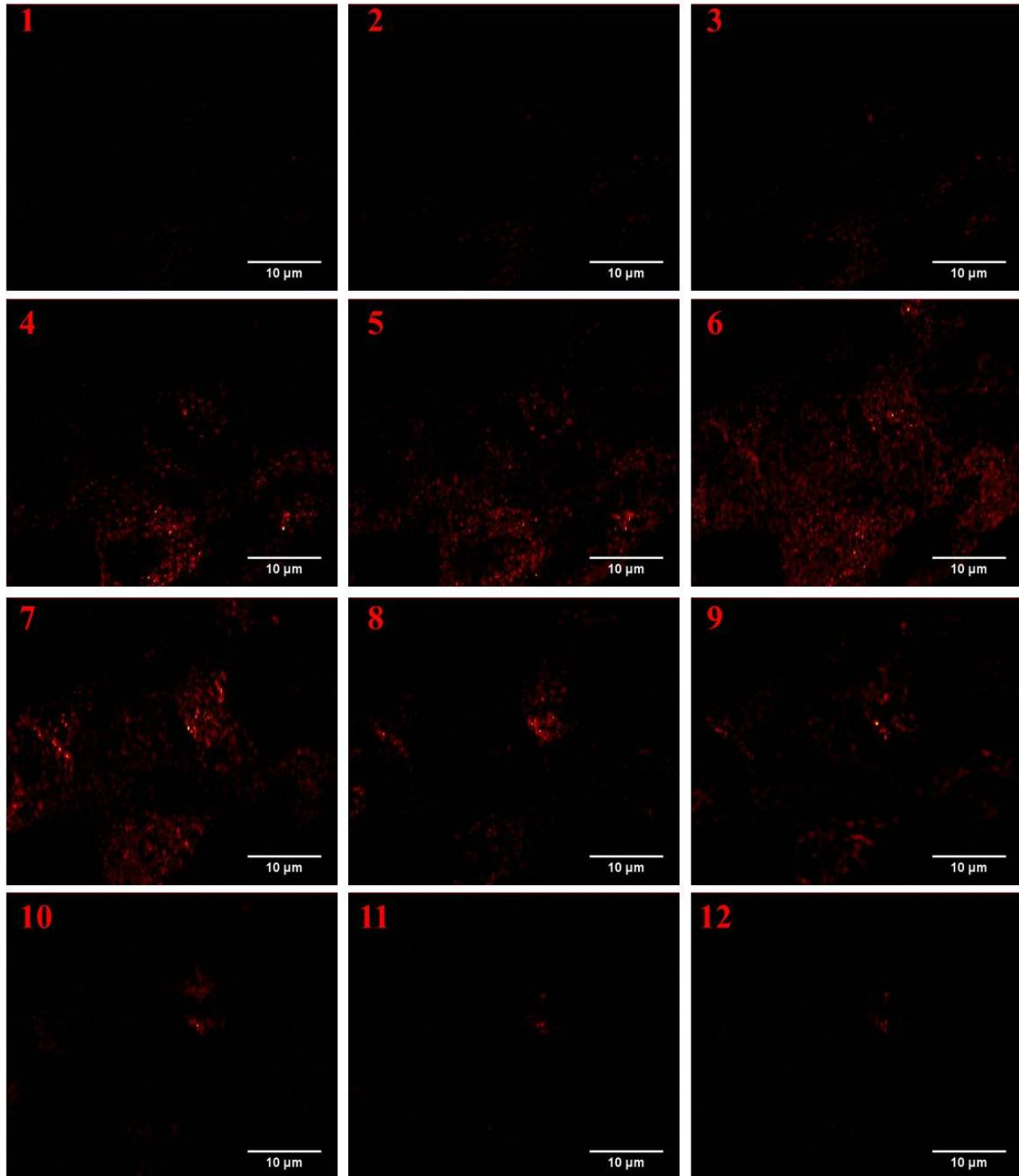


Figure 6.10: Twelve 2-D sections of the nucleus taken approximately 3 hours after the addition of import mixture containing 5 nm gold nanoparticles. The images show the lower (1-3), middle (4-9) and upper (10-12) sections of the cell nucleus. This figure demonstrates the confocal nature of the imaging scheme.

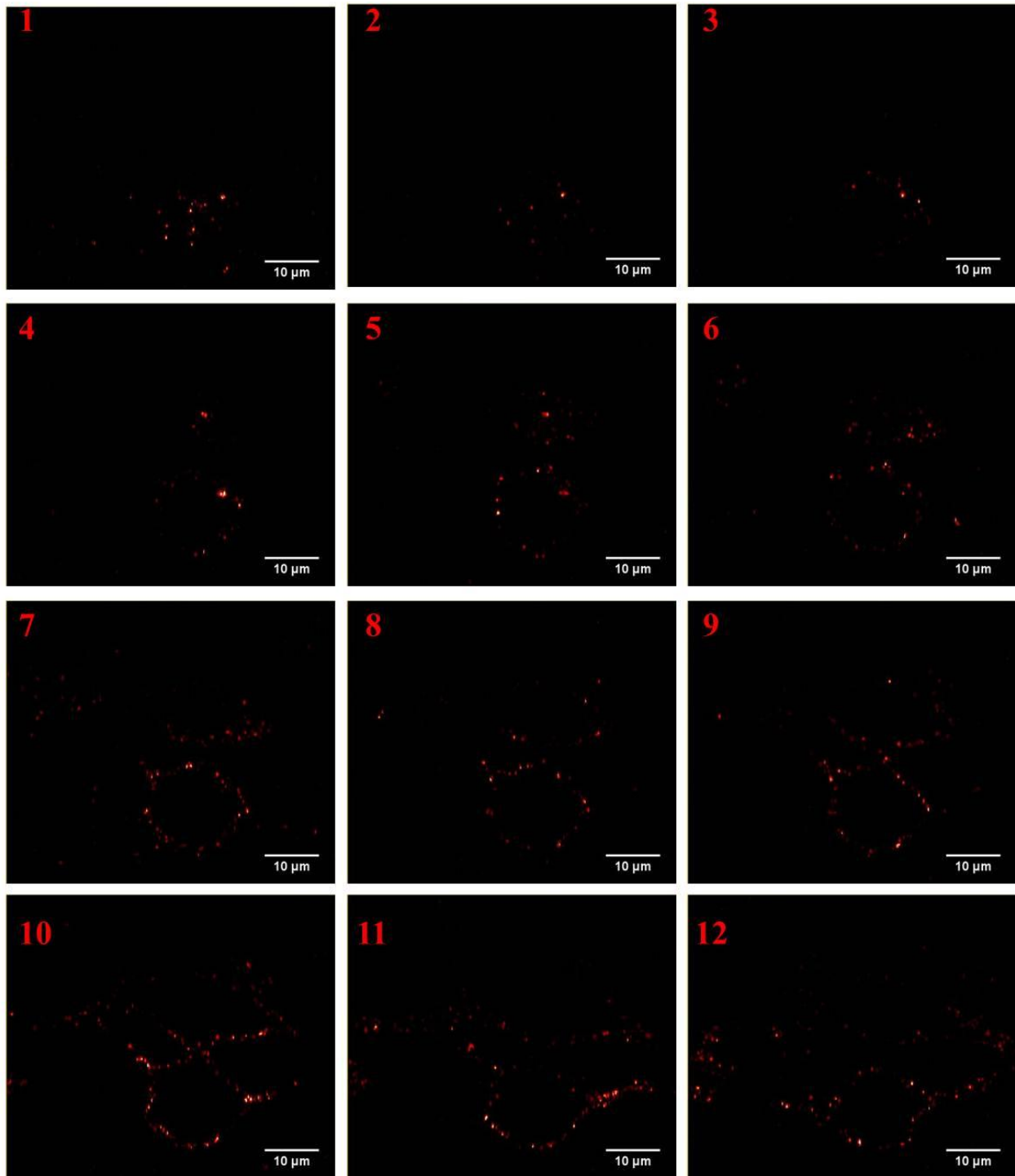


Figure 6.11: Twelve 2-D sections of the nucleus taken approximately 4 hours after the addition of import mixture containing 20 nm gold nanoparticles. The images show the lower (1-3), middle (4-9) and upper (10-12) sections of the cell nucleus. Images show gold nanoparticles adsorbed on the nuclear membranes.

We also took different Z-sections of the nucleus after the addition of 5 nm gold nanoparticles in the imaging chamber using the laser scanning photothermal microscope to check the confocality of the microscope. The images are taken about 3 hours after the addition of gold nanoparticles in approximately 1 μm steps along the Z-axis by moving the objective manually using the axial fine motion knob of the microscope. Figure 6.10 shows twelve axial cross sections of the nucleus. Figure 6.11 shows similar images of nucleus but stained with 20 nm gold nanoparticles.

We would conclude by stating that laser scanning photothermal microscopy has the potential to be a viable alternative imaging technique in biology but more efforts are needed to further improve the signal as well as the speed of acquisition. Data analysis tools have to be developed to have a quantitative analysis of the images such as the diffusion images shown here. We foresee the potential of the technique in bimolecular tracking, for example in tracking of the movement of a gold nanoparticle labeled DNA to the nucleus or vice versa in real time. Efforts are on in this direction, but are not reported in this thesis.

CHAPTER SEVEN

SUMMARY AND CONCLUSIONS

The role played by nuclear pore complexes in regulating the nuclear transport process is remarkable. The NPCs present in the nuclear membrane prevent any foreign DNA from entering the nucleus and at the same time regulate the transport of desired molecules in an organized and orderly fashion. Studies on nuclear transport would give insight into the working of NPCs and is important from the point view of experiments carried out on non-viral gene transfer in gene therapy. In this work we designed and developed the necessary microscopic techniques and investigated the biomolecular transport through nuclear membrane so as to determine the passive permeability of membranes.

A confocal fluorescence microscope is setup using an Olympus IX-71 microscope and an X-Y scan mirror system. The confocal laser scanning microscope is standardized using standard microparticles of known size. The CLSM set up is simple and flexible and is delivering reproducible intensity measurements with good image quality. The total cost of components used in this construction comes to about rupees 12 lakhs. This microscope can be implemented in any standard optics laboratory with minimum amount of additional expenditure. We have assessed the axial resolution and lateral resolution of the microscope with standard 100 nm polystyrene microparticles and the resolution of the microscope is close to that defined by the Rayleigh limit. Z sectioning capability of the microscope is analyzed using pollen grains and Fluocell test slides.

In this work we have used different biomolecules for studying nuclear transport rates and permeability of nuclear membrane. Passive diffusion studies are carried out under transient conditions using time lapse confocal fluorescence microscopy. Cell culture techniques to grow HeLa cells and A549 cells for the experiments have been standardized. Nuclear transport studies are carried out on FITC labeled dextran molecules of different Stokes radius and DNA fragments having different number of base pairs in digitonin permeabilized cells.

Kinetics of transport of dextran molecules of molecular weight 4 kDa, 10 kDa, 20 kDa, 40 kDa and 70 kDa are studied using the time lapse imaging scheme with our home built CLSM. Live A549 cells and HeLa cells are used as a model cell system and the diffusion rate constants of transport into the cell nuclei are determined. Membrane permeability of digitonin permeabilized cells is determined for the sizes 4 kDa, 10 kDa, 20 kDa and 40 kDa. It is found that the 40 kDa molecules are transported across the nucleus with very low rate constant, while 70 kDa molecules are completely blocked indicating the molecular weight limitation of particles. From the analysis of the diffusion rate constants of these molecules, we estimate the effective pore radius of HeLa cell nucleus to be in the range of 4.9 – 5.7 nm (mean 5.3 nm).

In this work we have also analyzed the effect of the size of linear double stranded DNA on its passive diffusion. DNA of size upto 750 bp entered the nuclei of digitonin treated A549 cells in the presence of RRL by passive diffusion. The size limit for passive diffusion of DNA is found to be between 750 and 1000 bp in digitonin permeabilized cell system in presence of RRL. We studied the dependence of RRL on the nuclear transport rates of dextran and DNA molecules. Our data indicate that intensity of DNA nuclear transport could be increased by increasing the concentration of RRL.

To circumvent the limitation of fluorescence microscopy due to photobleaching, we developed a laser scanning photothermal microscope that can detect and image gold nanoparticles at fast time scales. Photothermal imaging of gold nanoparticles of size as small as 5 nm is achieved with high signal to noise ratio and with a low pixel dwell time of 80 μ s. Gold nanoparticles are highly photostable, less toxic, biocompatible and can easily be conjugated with biomolecules of interest. The laser scanning photothermal microscope provides a potential bio-imaging tool that allows fast image acquisition using gold nanoparticles as labels in living cells. The fast scan rates are especially important in studies focusing on live cell imaging and tracking of biomolecular transport.

Thus the major achievements of the present work may be summarized as:

- ❖ A simple and cost effective confocal laser scanning microscope is successfully setup and standardized using standard microparticles and biological test slides.
- ❖ Adherent cell culture techniques and digitonin permeabilization of cell membrane are optimized for nuclear transport measurements.
- ❖ Kinetics of transport of dextran molecules through the nuclear membranes of live HeLa and A549 cells are studied. Rate constants of transport for the model drug molecule are determined for different Stokes radius.
- ❖ Passive permeability limit of nuclear membrane is determined and the functional nuclear pore radius estimated as 4.9 – 5.7 nm (mean 5.3 nm).
- ❖ Effect of RRL on different biomolecular transport through nuclear membrane is studied. RRL play an important role in deciding the rates of biomolecular import to the nucleus. Nuclear transport rates could be increased by increasing the concentration of RRL in import mixture.
- ❖ Confocal imaging of nuclear transport of dye labeled DNA fragments of different sizes is carried out and their rates of nuclear transport determined from kinetic analysis of transport. The size exclusion limit for passive diffusion of DNA is found to be between 750 and 1000 bp in digitonin permeabilized cell.
- ❖ Successfully implemented laser scanning photothermal microscopy for biomolecular imaging using gold nanoparticles as labels. The laser scanning method developed here allows for fast image acquisition with a pixel dwell time of 80 μ s so that a 500 \times 500 pixel image can be acquired in 20 seconds. Photothermal imaging at fast time scales can have potential applications in variety of fields including tracking of biomolecular movement in a live cell.

Biomolecular transport through membranes is a vast area of research. In this work we have examined only certain specific aspects pertaining to the passive permeability of nuclear membranes. Effect of transport receptors such as importins and NLS on the passive nuclear transport could be examined as potential active factors affecting passive nuclear transport. Active nuclear transport and the influence of simultaneous passive and active nuclear transport on rates could reveal the nature of the nuclear pores and verify the multichannel and single channel pictures of the NPCs. The photothermal microscopy of gold nanoparticle labeled biomolecules has the potential to track and study their targeted movement inside the nucleus.

REFERENCES

- Adam, S. A. (2001) The nuclear pore complex. *Genome Biol*, **2**, Reviews0007, 1-6.
- Adam, S. A., Marr, R. S. & Gerace, L. (1990) Nuclear protein import in permeabilized mammalian cells requires soluble cytoplasmic factors. *J Cell Biol*, **111**, 807-816.
- Akey, C. W. (1989) Interactions and structure of the nuclear pore complex revealed by cryo-electron microscopy. *J Cell Biol*, **109**, 955-970.
- Akey, C. W. (1995) Structural plasticity of the nuclear pore complex. *J Mol Biol*, **248**, 273-293.
- Attik, G. N., Pradelle-Plasse, N., Campos, D., Colon, P. & Grosogeat, B. (2013) Toxicity evaluation of two dental composites: three-dimensional confocal laser scanning microscopy time-lapse imaging of cell behavior. *Microsc Microanal*, **19**, 596-607.
- Bagley, S., Goldberg, M. W., Cronshaw, J. M., Rutherford, S. & Allen, T. D. (2000) The nuclear pore complex. *J Cell Sci*, **113** (Pt 22), 3885-3886.
- Bastos, R., Pante, N. & Burke, B. (1995) Nuclear pore complex proteins. *Int Rev Cytol*, **162**, 257-302.
- Berciaud, S., Lasne, D., Blab, G., Cognet, L. & Lounis, B. (2006) Photothermal heterodyne imaging of individual metallic nanoparticles: Theory versus experiment. *Physical Review B*, **73**, 045424, 1-8.
- Berrios, M., Meller, V. H., McConnell, M. & Fisher, P. A. (1995) Drosophila gp210, an invertebrate nuclear pore complex glycoprotein. *Eur J Cell Biol*, **67**, 1-7.
- Bodoor, K., Shaikh, S., Enarson, P., Chowdhury, S., Salina, D., Raharjo, W. H. & Burke, B. (1999) Function and assembly of nuclear pore complex proteins. *Biochem Cell Biol*, **77**, 321-329.

- Bogart, L. K., Taylor, A., Cesbron, Y., Murray, P. & Levy, R. (2012) Photothermal Microscopy of the Core of Dextran-Coated Iron Oxide Nanoparticles During Cell Uptake. *ACS Nano*, **6**, 5961-5971.
- Bohren, C. F. & Huffman, D. R. (1998) *Absorption and Scattering of Light by Small Particles*. John Wiley and Sons, Inc., New York.
- Boyer, D., Tamarat, P., Maali, A., Lounis, B. & Orrit, M. (2002) Photothermal imaging of nanometer-sized metal particles among scatterers. *Science*, **297**, 1160-1163.
- Brownawell, A. M., Holaska, J. M., Macara, I. G. & Paschal, B. M. (2002) The use of permeabilized cell systems to study nuclear transport. *Methods Mol Biol*, **189**, 209-229.
- Carlsson, K., Danielsson, P. E., Lenz, R., Liljeborg, A., Majlof, L. & Aslund, N. (1985) Three-dimensional microscopy using a confocal laser scanning microscope. *Opt Lett*, **10**, 53-55.
- Chatel, G. & Fahrenkrog, B. (2012) Dynamics and diverse functions of nuclear pore complex proteins. *Nucleus*, **3**, 162-171.
- Cole, R. W., Jinadasa, T. & Brown, C. M. (2011) Measuring and interpreting point spread functions to determine confocal microscope resolution and ensure quality control. *Nat Protoc*, **6**, 1929-1941.
- Conti, E. & Izaurralde, E. (2001) Nucleocytoplasmic transport enters the atomic age. *Curr Opin Cell Biol*, **13**, 310-319.
- Conti, E., Uy, M., Leighton, L., Blobel, G. & Kuriyan, J. (1998) Crystallographic analysis of the recognition of a nuclear localization signal by the nuclear import factor karyopherin alpha. *Cell*, **94**, 193-204.
- Coons, A. H., Leduc, E. H. & Kaplan, M. H. (1951) Localization of antigen in tissue cells. VI. The fate of injected foreign proteins in the mouse. *J Exp Med*, **93**, 173-188.

- Dean, D. A. & Kasamatsu, H. (1994) Signal- and energy-dependent nuclear transport of SV40 Vp3 by isolated nuclei. Establishment of a filtration assay for nuclear protein import. *J Biol Chem*, **269**, 4910-4916.
- Deng, Q., Chen, J. L., Zhou, Q., Hu, B., Chen, Q., Huang, J. & Guo, R. Q. (2013) Ultrasound microbubbles combined with the NFkappaB binding motif increase transfection efficiency by enhancing the cytoplasmic and nuclear import of plasmid DNA. *Mol Med Rep*, **8**, 1439-1445.
- Doxiades, T. & Candreviotis, N. (1962) Detection of entamoeba histolytica by fluorescent microscopy. *Br Med J*, **1**, 1810, 1-2.
- Doye, V. & Hurt, E. C. (1995) Genetic approaches to nuclear pore structure and function. *Trends Genet*, **11**, 235-241.
- Egger, M. D. & Petran, M. (1967) New reflected-light microscope for viewing unstained brain and ganglion cells. *Science*, **157**, 305-307.
- Ernst Keller, H. & Watkins, S. (2013) *Contrast enhancement in light microscopy*. Curr Protoc Cytom, Chapter 2, Unit 2.1, 1-11
- Escriou, V., Carriere, M., Scherman, D. & Wils, P. (2003) NLS bioconjugates for targeting therapeutic genes to the nucleus. *Adv Drug Deliv Rev*, **55**, 295-306.
- Escriou, V., Ciolina, C., Helbling-Leclerc, A., Wils, P. & Scherman, D. (1998) Cationic lipid-mediated gene transfer: analysis of cellular uptake and nuclear import of plasmid DNA. *Cell Biol Toxicol*, **14**, 95-104.
- Etheridge, T. J., Boulineau, R. L., Herbert, A., Watson, A. T., Daigaku, Y., Tucker, J., George, S., Jonsson, P., Palayret, M., Lando, D., Laue, E., Osborne, M. A., Klenerman, D., Lee, S. F. & Carr, A. M. (2014) Quantification of DNA-associated proteins inside eukaryotic cells using single-molecule localization microscopy. *Nucleic Acids Res*, **42**, 146, 1-11.
- Faustino, R. S., Czubryt, M. P. & Pierce, G. N. (2002) Determining influence of oxidants on nuclear transport using digitonin-permeabilized cell assay. *Methods Enzymol*, **352**, 123-134.

- Feldherr, C. M. (1962) The nuclear annuli as pathways for nucleocytoplasmic exchanges. *J Cell Biol*, **14**, 65-72.
- Feldherr, C. M. (1965) The Effect of the Electron-Opaque Pore Material on Exchanges through the Nuclear Annuli. *J Cell Biol*, **25**, 43-53.
- Feldherr, C. M. (1966) Nucleocytoplasmic exchanges during cell division. *J Cell Biol*, **31**, 199-203.
- Franke, W. W. (1970) Nuclear pore flow rate. A characteristic for nucleocytoplasmic exchange of macromolecules and particles. *Naturwissenschaften*, **57**, 44-45.
- Fraser, J. E., Rawlinson, S. M., Wang, C., Jans, D. A. & Wagstaff, K. M. (2014) Investigating dengue virus nonstructural protein 5 (NS5) nuclear import. *Methods Mol Biol*, **1138**, 301-328.
- Fried, H. & Kutay, U. (2003) Nucleocytoplasmic transport: taking an inventory. *Cell Mol Life Sci*, **60**, 1659-1688.
- Fu, L. & Sztul, E. (2015) Characterization of intracellular aggresomes by fluorescent microscopy. *Methods Mol Biol*, **1258**, 307-317.
- Gaiduk, A., Ruijgrok, P. V., Yorulmaz, M. & Orrit, M. (2010a) Detection limits in photothermal microscopy. *Chemical Science*, **1**, 343-350.
- Gaiduk, A., Yorulmaz, M., Ruijgrok, P. V. & Orrit, M. (2010b) Room-temperature detection of a single molecule's absorption by photothermal contrast. *Science*, **330**, 353-356.
- Gfrerer, L., Dougherty, M. & Liao, E. C. (2013) Visualization of craniofacial development in the sox10: kaede transgenic zebrafish line using time-lapse confocal microscopy. *J Vis Exp*, e50525.
- Goldberg, M. W. & Allen, T. D. (1993) The nuclear pore complex: three-dimensional surface structure revealed by field emission, in-lens scanning electron microscopy, with underlying structure uncovered by proteolysis. *J Cell Sci*, **106**, 261-274.
- Gorlich, D. & Kutay, U. (1999) Transport between the cell nucleus and the cytoplasm. *Annu Rev Cell Dev Biol*, **15**, 607-660.

- Gotter, B., Faubel, W. & Neubert, R. H. (2010) Photothermal imaging in 3D surface analysis of membrane drug delivery. *Eur J Pharm Biopharm*, **74**, 26-32.
- Hagstrom, J. E., Ludtke, J. J., Bassik, M. C., Sebestyen, M. G., Adam, S. A. & Wolff, J. A. (1997) Nuclear import of DNA in digitonin-permeabilized cells. *J Cell Sci*, **110**, 2323-2331.
- Hardeland, U. & Hurt, E. (2006) Coordinated nuclear import of RNA polymerase III subunits. *Traffic*, **7**, 465-473.
- Hebert, E. (2003) Improvement of exogenous DNA nuclear importation by nuclear localization signal-bearing vectors: a promising way for non-viral gene therapy? *Biol Cell*, **95**, 59-68.
- Hindley, C. E., Lawrence, F. J. & Matthews, D. A. (2007) A role for transportin in the nuclear import of adenovirus core proteins and DNA. *Traffic*, **8**, 1313-1322.
- Holland, J. C. & Ackermann, M. R. (1961) Fluorescent microscopy in the diagnosis of cervical carcinoma. Its application in office practice. *Obstet Gynecol*, **17**, 38-40.
- Holtfreter, J. (1954) Observations on the physico-chemical properties of isolated nuclei. *Exp Cell Res*, **7**, 95-102.
- Huang, N. P., Stubenrauch, M., Koser, J., Taschner, N., Aebi, U. & Stolz, M. (2010) Towards monitoring transport of single cargos across individual nuclear pore complexes by time-lapse atomic force microscopy. *J Struct Biol*, **171**, 154-162.
- Huet, S., Avilov, S. V., Ferbitz, L., Daigle, N., Cusack, S. & Ellenberg, J. (2010) Nuclear import and assembly of influenza A virus RNA polymerase studied in live cells by fluorescence cross-correlation spectroscopy. *J Virol*, **84**, 1254-1264.
- Jaggi, R. D., Franco-Obregon, A., Muhlhauser, P., Thomas, F., Kutay, U. & Ensslin, K. (2003) Modulation of nuclear pore topology by transport modifiers. *Biophys J*, **84**, 665-670.
- Jarrett, A., Bligh, A. & Hardy, J. A. (1956) Fluorescent microscopy of the human skin. *Br J Dermatol*, **68**, 111-119.

- Johnson, M. A., Sharma, M., Mok, M. T. & Henderson, B. R. (2013) Stimulation of in vivo nuclear transport dynamics of actin and its co-factors IQGAP1 and Rac1 in response to DNA replication stress. *Biochim Biophys Acta*, **1833**, 2334-2347.
- Johnson, W. L. & Straight, A. F. (2013) Fluorescent protein applications in microscopy. *Methods Cell Biol*, **114**, 99-123.
- Kapon, R., Naim, B., Zbaida, D., Nevo, R., Tsabari, O. & Reich, Z. (2010) Permeating the nuclear pore complex. *Nucleus*, **1**, 475-480.
- Katta, S. S., Smoyer, C. J. & Jaspersen, S. L. (2013) *Destination: inner nuclear membrane*. Trends Cell Biol. Cell Press, Elsevier, Massachusetts, United States.
- Keller, R. & Pisha, B. V. (1947) Fluorescent microscopy of fluid movements in living tissue. *Clin Med*, **54**, 394.
- Keminer, O. & Peters, R. (1999) Permeability of single nuclear pores. *Biophys J*, **77**, 217-228.
- Keohane, K. W. & Metcalf, W. K. (1958) Some experiments in fluorescent microscopy designed to elucidate the fate of the lymphocyte. *Q J Exp Physiol Cogn Med Sci*, **43**, 408-418.
- Kiseleva, E., Goldberg, M. W., Cronshaw, J. & Allen, T. D. (2000) The nuclear pore complex: structure, function, and dynamics. *Crit Rev Eukaryot Gene Expr*, **10**, 101-112.
- Kiskin, N. I., Siebrasse, J. P. & Peters, R. (2003) Optical microwell assay of membrane transport kinetics. *Biophys J*, **85**, 2311-2322.
- Kleinsmith, L. J. & Kish, V. M. (1995) *Principles of cell and molecular biology*, HarperCollins, New York.
- Koch, P. C., Seebacher, C. & Hess, M. (2010) 3D-topography of cell nuclei in a vertebrate retina--a confocal and two-photon microscopic study. *J Neurosci Methods*, **188**, 127-140.
- Kreft, M., Stenovec, M. & Zorec, R. (2005) Focus-drift correction in time-lapse confocal imaging. *Ann N Y Acad Sci*, **1048**, 321-330.

- Kulzer, F., Laurens, N., Besser, J., Schmidt, T., Orrit, M. & Spaink, H. P. (2008) Photothermal detection of individual gold nanoparticles: perspectives for high-throughput screening. *Chemphysche: a European journal of chemical physics and physical chemistry*, **9**, 1761-1766.
- Lamprecht, A., Schafer, U. & Lehr, C. M. (2000) Structural analysis of microparticles by confocal laser scanning microscopy. *AAPS PharmSciTech*, **1**, E17, 1-10.
- Lasne, D., Blab, G. A., Berciaud, S., Heine, M., Groc, L., Choquet, D., Cognet, L. & Lounis, B. (2006) Single nanoparticle photothermal tracking (SNaPT) of 5-nm gold beads in live cells. *Biophysical journal*, **91**, 4598-4604.
- Lee, M. A., Dunn, R. C., Clapham, D. E. & Stehno-Bittel, L. (1998) Calcium regulation of nuclear pore permeability. *Cell Calcium*, **23**, 91-101.
- Li, S., Luby-Phelps, K., Zhang, B., Wu, X. & Gao, J. (2011) Subcellular particles tracking in time-lapse confocal microscopy images. *Conf Proc IEEE Eng Med Biol Soc*, **2011**, 5973-5976.
- Liang, R., Erwin, J. K. & Mansuripur, M. (2000) Variation on Zernike's phase-contrast microscope. *Appl Opt*, **39**, 2152-2158.
- Ludtke, J. J., Zhang, G., Sebestyen, M. G. & Wolff, J. A. (1999) A nuclear localization signal can enhance both the nuclear transport and expression of 1 kb DNA. *J Cell Sci*, **112**, 2033-2041.
- Lukacs, G. L., Haggie, P., Seksek, O., Lechardeur, D., Freedman, N. & Verkman, A. S. (2000) Size-dependent DNA mobility in cytoplasm and nucleus. *J Biol Chem*, **275**, 1625-1629.
- Macaulay, C., Meier, E. & Forbes, D. J. (1995) Differential mitotic phosphorylation of proteins of the nuclear pore complex. *J Biol Chem*, **270**, 254-262.
- Matsukawa, Y., Lee, V. H. L., Crandall, E. D. & Kim, K. J. (1997) Size dependent dextran transport across rat alveolar epithelial cell monolayers. *Journal of Pharmaceutical Sciences*, **86**, 305-309.
- Mearini, G., Nielsen, P. E. & Fackelmayer, F. O. (2004) Localization and dynamics of small circular DNA in live mammalian nuclei. *Nucleic Acids Res*, **32**, 2642-2651.

- Megason, S. G. (2009) In toto imaging of embryogenesis with confocal time-lapse microscopy. *Methods Mol Biol*, **546**, 317-332.
- Meinema, A. C., Poolman, B. & Veenhoff, L. M. (2012) The transport of integral membrane proteins across the nuclear pore complex. *Nucleus*, **3**, 322-329.
- Miyawaki, A., Sawano, A. & Kogure, T. (2003) Lighting up cells: labelling proteins with fluorophores. *Nat Cell Biol, Suppl*, S1-7.
- Mizuguchi-Hata, C., Ogawa, Y., Oka, M. & Yoneda, Y. (2013) Quantitative regulation of nuclear pore complex proteins by O-GlcNAcylation. *Biochim Biophys Acta*, **1833**, 2682-2689.
- Mohr, D., Frey, S., Fischer, T., Guttler, T. & Gorlich, D. (2009) Characterisation of the passive permeability barrier of nuclear pore complexes. *EMBO J*, **28**, 2541-2553.
- Mooren, O. L., Erickson, E. S., Moore-Nichols, D. & Dunn, R. C. (2004) Nuclear side conformational changes in the nuclear pore complex following calcium release from the nuclear membrane. *Phys Biol*, **1**, 125-134.
- Munkonge, F. M., Dean, D. A., Hillery, E., Griesenbach, U. & Alton, E. W. (2003) Emerging significance of plasmid DNA nuclear import in gene therapy. *Adv Drug Deliv Rev*, **55**, 749-760.
- Naim, B., Brumfeld, V., Kapon, R., Kiss, V., Nevo, R. & Reich, Z. (2007) Passive and facilitated transport in nuclear pore complexes is largely uncoupled. *J Biol Chem*, **282**, 3881-3888.
- Nowotschin, S., Ferrer-Vaquer, A. & Hadjantonakis, A. K. (2010) Imaging mouse development with confocal time-lapse microscopy. *Methods Enzymol*, **476**, 351-377.
- Nwaneshiudu, A., Kuschal, C., Sakamoto, F. H., Anderson, R. R., Schwarzenberger, K. & Young, R. C. (2012) Introduction to confocal microscopy. *J Invest Dermatol*, **132**, e3, 1-5.
- Paddock, S. W. & Eliceiri, K. W. (2014) Laser scanning confocal microscopy: history, applications, and related optical sectioning techniques. *Methods Mol Biol*, **1075**, 9-47.
- Paine, P. L., Moore, L. C. & Horowitz, S. B. (1975) Nuclear envelope permeability. *Nature*, **254**, 109-114.

- Pante, N. & Aebi, U. (1996) Sequential binding of import ligands to distinct nucleopore regions during their nuclear import. *Science*, **273**, 1729-1732.
- Parsons, D. F. & Johnson, H. M. (1972) Possibility of a phase contrast electron microscope. *Appl Opt*, **11**, 2840-2843.
- Pawley, J. B. (2006) *Handbook of biological confocal microscopy*, Springer, New York, NY.
- Peters, R. (1983a) Fluorescence microphotolysis. Diffusion measurements in single cells. *Naturwissenschaften*, **70**, 294-302.
- Peters, R. (1983b) Nuclear envelope permeability measured by fluorescence microphotolysis of single liver cell nuclei. *J Biol Chem*, **258**, 11427-11429.
- Peters, R. (1986) Fluorescence microphotolysis to measure nucleocytoplasmic transport and intracellular mobility. *Biochim Biophys Acta*, **864**, 305-359.
- Peters, R. (2005) Translocation through the nuclear pore complex: selectivity and speed by reduction-of-dimensionality. *Traffic*, **6**, 421-427.
- Peters, R., Coutavas, E. & Siebrasse, J. P. (2002) Nuclear transport kinetics in microarrays of nuclear envelope patches. *J Struct Biol*, **140**, 268-278.
- Pologruto, T. A., Sabatini, B. L. & Svoboda, K. (2003) ScanImage: flexible software for operating laser scanning microscopes. *Biomed Eng Online*, **2**, 13, 1-9.
- Ribbeck, K. & Gorlich, D. (2001) Kinetic analysis of translocation through nuclear pore complexes. *EMBO J*, **20**, 1320-1330.
- Richardson, J. C. & Maddy, A. H. (1980) The polypeptides of rat liver nuclear envelope. I. Examination by nuclear pore complex polypeptides by solid-state lactoperoxidase labelling. *J Cell Sci*, **43**, 253-267.
- Ris, H. (1997) High-resolution field-emission scanning electron microscopy of nuclear pore complex. *Scanning*, **19**, 368-375.

- Riviere, L., Darlix, J. L. & Cimarelli, A. (2010) Analysis of the viral elements required in the nuclear import of HIV-1 DNA. *J Virol*, **84**, 729-739.
- Rout, M. P., Aitchison, J. D., Suprpto, A., Hjertaas, K., Zhao, Y. & Chait, B. T. (2000) The yeast nuclear pore complex: composition, architecture, and transport mechanism. *J Cell Biol*, **148**, 635-651.
- Rout, M. P., Blobel, G. & Aitchison, J. D. (1997) A distinct nuclear import pathway used by ribosomal proteins. *Cell*, **89**, 715-725.
- Schneider, C. A., Rasband, W. S. & Eliceiri, K. W. (2012) NIH Image to ImageJ: 25 years of image analysis. *Nat Methods*, **9**, 671-675.
- Schuldt, A. (2012) Nuclear transport: A new way out. *Nat Rev Mol Cell Biol*, **13**, 407.
- Schutz, S., Fischer, U., Altvater, M., Nerurkar, P., Pena, C., Gerber, M., Chang, Y., Caesar, S., Schubert, O. T., Schlenstedt, G. & Panse, V. G. (2014) A RanGTP-independent mechanism allows ribosomal protein nuclear import for ribosome assembly. *Elife*, **3**, e03473, 1-24.
- Sheppard, C. J. & Wilson, T. (1979) Effect of spherical aberration on the imaging properties of scanning optical microscopes. *Appl Opt*, **18**, 1058-1063.
- Sheppard, C. J. & Wilson, T. (1981) The theory of the direct-view confocal microscope. *J Microsc*, **124**, 107-117.
- Simos, G. & Hurt, E. C. (1995) Nucleocytoplasmic transport: factors and mechanisms. *FEBS Lett*, **369**, 107-112.
- Siniooglou, S., Wimmer, C., Rieger, M., Doye, V., Tekotte, H., Weise, C., Emig, S., Segref, A. & Hurt, E. C. (1996) A novel complex of nucleoporins, which includes Sec13p and a Sec13p homolog, is essential for normal nuclear pores. *Cell*, **84**, 265-275.
- Spector, D. L. (1993) Macromolecular domains within the cell nucleus. *Annu Rev Cell Biol*, **9**, 265-315.

- Spector, D. L., O'Keefe, R. T. & Jimenez-Garcia, L. F. (1993) Dynamics of transcription and pre-mRNA splicing within the mammalian cell nucleus. *Cold Spring Harb Symp Quant Biol*, **58**, 799-805.
- Steer, R. C., Goueli, S. A., Wilson, M. J. & Ahmed, K. (1980) Cobalt-stimulated protein phosphokinase activity of the pore complex-lamina fraction from rat liver nuclear envelope. *Biochem Biophys Res Commun*, **92**, 919-925.
- Stephens, D. J. & Allan, V. J. (2003) Light microscopy techniques for live cell imaging. *Science*, **300**, 82-86.
- Strambio-De-Castillia, C., Niepel, M. & Rout, M. P. (2010) The nuclear pore complex: bridging nuclear transport and gene regulation. *Nat Rev Mol Cell Biol*, **11**, 490-501.
- Tate, S. & Elborn, S. (2005) Progress towards gene therapy for cystic fibrosis. *Expert Opin Drug Deliv*, **2**, 269-280.
- Terry, L. J., Shows, E. B. & Wentz, S. R. (2007) Crossing the nuclear envelope: hierarchical regulation of nucleocytoplasmic transport. *Science*, **318**, 1412-1416.
- Twyffels, L., Gueydan, C. & Kruys, V. (2014) Transportin-1 and Transportin-2: protein nuclear import and beyond. *FEBS Lett*, **588**, 1857-1868.
- Vacik, J., Dean, B. S., Zimmer, W. E. & Dean, D. A. (1999) Cell-specific nuclear import of plasmid DNA. *Gene Ther*, **6**, 1006-1014.
- van der Aa, M. A., Mastrobattista, E., Oosting, R. S., Hennink, W. E., Koning, G. A. & Crommelin, D. J. (2006) The nuclear pore complex: the gateway to successful nonviral gene delivery. *Pharm Res*, **23**, 447-459.
- van Os, C. H., de Jong, M. D. & Slegers, J. F. (1974) Dimensions of polar pathways through rabbit gallbladder epithelium. The effect of phloretin on nonelectrolyte permeability. *J Membr Biol*, **15**, 363-382.

- Vancurova, I., Jochova-Rupes, J., Lou, W. & Paine, P. L. (1995) Distinct phosphorylation sites differentially influence facilitated transport of an NLS-protein and its subsequent intranuclear binding. *Biochem Biophys Res Commun*, **217**, 419-427.
- Villalta, J. I., Galli, S., Iacaruso, M. F., Antico Arciuch, V. G., Poderoso, J. J., Jares-Erijman, E. A. & Pietrasanta, L. I. (2011) New algorithm to determine true colocalization in combination with image restoration and time-lapse confocal microscopy to MAP kinases in mitochondria. *PLoS One*, **6**, e19031, 1-16.
- Watters, K. & Palmenberg, A. C. (2011) Differential processing of nuclear pore complex proteins by rhinovirus 2A proteases from different species and serotypes. *J Virol*, **85**, 10874-10883.
- Wente, S. R. & Rout, M. P. (2010) The nuclear pore complex and nuclear transport. *Cold Spring Harb Perspect Biol*, **2**, a000562.
- Wilson, G. L., Dean, B. S., Wang, G. & Dean, D. A. (1999) Nuclear import of plasmid DNA in digitonin-permeabilized cells requires both cytoplasmic factors and specific DNA sequences. *J Biol Chem*, **274**, 22025-22032.
- Wilson, T. & Sheppard, C. (1984) *Theory and practice of scanning optical microscopy*, Academic Press, London; Orlando.
- Wolff, J. A. & Budker, V. (2005) The mechanism of naked DNA uptake and expression. *Adv Genet*, **54**, 3-20.
- Wooding, F. B. & O'Donnell, J. M. (1971) A detailed ultrastructural study of the head membranes of ejaculated bovine sperm. *J Ultrastruct Res*, **35**, 71-85.
- Xi, P., Rajwa, B., Jones, J. T. & Robinson, J. P. (2007) The design and construction of a cost-efficient confocal laser scanning microscope. *American Journal of Physics*, **75**, 203-207.
- Xylourgidis, N. & Fornerod, M. (2009) Acting out of character: regulatory roles of nuclear pore complex proteins. *Dev Cell*, **17**, 617-625.

Zhang, G., Budker, V. G., Ludtke, J. J. & Wolff, J. A. (2004) Naked DNA gene transfer in mammalian cells. *Methods Mol Biol*, **245**, 251-264.

Zharov, V. & Lapotko, D. (2003) Photothermal sensing of nanoscale targets. *Review of Scientific Instruments*, **74**, 785-788.

Zucker, R. M. & Price, O. T. (1999) Practical confocal microscopy and the evaluation of system performance. *Methods*, **18**, 447-458.

PUBLICATIONS AND PRESENTATIONS

RESEARCH PUBLICATIONS

- ❖ **S. Arunkarthick**, M. M. Bijeesh, Anand Satya Vetcha, Nishith Rastogi, P. Nandakumar and Geetha K. Varier. **Design and construction of a confocal laser scanning microscope for biomolecular imaging.** *Current Science*, 2014, **107 (12)**, 1965-1969. (IF – 0.833).
- ❖ **S. Arunkarthick**, M. M. Bijeesh, Geetha K. Varier, Meenal Kowshik and P. Nandakumar. **Laser Scanning Photothermal Microscopy: Fast Detection and Imaging of Gold Nanoparticles.** *Journal of Microscopy*, 2014, **256 (2)**, 111-116. doi: 10.1111/jmi.12164. (IF – 2.15).
- ❖ M. M. Bijeesh, **S. Arunkarthick**, K. Arvind, R. Nishith, Geetha K. Varier, Meenal Kowshik and P. Nandakumar. **Construction of Simple Confocal Microscope.** *Kiran*, 2011, **22 (1)**, 26-28.
- ❖ **S. Arunkarthick**, M. M. Bijeesh, Geetha K. Varier, Meenal Kowshik & P. Nandakumar. **Studies on Nuclear Transport of FITC Labeled Dextran Using Confocal Laser Scanning Microscopy.** (Accepted for Publication through ICBH13 conference)
- ❖ **S. Arunkarthick**, M. M. Bijeesh, Meenal Kowshik, P. Nandakumar and Geetha K. Varier. **Passive permeability and effective pore size of HeLa cell nuclear membranes.** (Communicated)
- ❖ **S. Arunkarthick**, M. M. Bijeesh, Geetha K. Varier, Meenal Kowshik and P. Nandakumar. **Influence of rabbit reticulocyte lysate on the nuclear transport kinetics of dextran and DNA.** (Manuscript under preparation)

PUBLICATIONS IN CONFERENCES (PAPER / POSTER PRESENTATIONS)

- ❖ **S. Arunkarthick**, M. M. Bijeesh, Geetha K. Varier, Meenal Kowshik and P. Nandakumar. “**Studies on Biomolecular Transport through Nuclear Membranes using a Home Built Confocal Laser Scanning Microscope**”, **18th International Microscopy congress (IMC-2014), Prague, Czech Republic**, September 7-12, 2014.
- ❖ **S. Arunkarthick**, M. M. Bijeesh, Geetha K. Varier, Meenal Kowshik and P. Nandakumar. “**Permeability studies on nuclear membranes using confocal laser**

scanning microscopy”, DAE-BRNS National Laser Symposium (NLS-22), MIT, Manipal University, Manipal, Karnataka, January 8-11, 2014.

- ❖ **S. Arunkarthick**, M. M. Bijeesh, Geetha K. Varier, Meenal Kowshik and P. Nandakumar. “**Optical microscopic studies on biomolecular transport through nuclear membranes**”, **37th All India Cell Biology Conference on “Cell Dynamics and Cell Fate**”, InStem, Bangalore, December 22- 24, 2013.
- ❖ **S. Arunkarthick**, M. M. Bijeesh, Geetha K. Varier, Meenal Kowshik and P. Nandakumar. “**Studies on Nuclear Transport of FITC Labelled Dextran Using Confocal Laser Scanning Microscopy**”, **International Conference on Biotechnology and Human Welfare**, SASTRA University and M S Swaminathan Research Foundation, Tamil Nadu, during December 6-8, 2013.
- ❖ **S. Arunkarthick**, M. M. Bijeesh, Geetha K. Varier, Meenal Kowshik and P. Nandakumar. “**Photothermal Laser Scanning Microscopy**”, **Focus on Microscopy 2013, Maastricht, The Netherlands** during March 24 - March 27, 2013.
- ❖ **S. Arunkarthick**, M. M. Bijeesh, Geetha K. Varier, Meenal Kowshik and P. Nandakumar. “**Nuclear Transport Study Using Home Built Confocal Laser Scanning Microscopy**” **4th Bangalore Microscopy Course**, National Centre for Biological Sciences (NCBS), TIFR, Bangalore, during September 23-30, 2012.
- ❖ **S. Arunkarthick**, M. M. Bijeesh, Geetha K. Varier, Meenal Kowshik and P. Nandakumar. “**Laser scanning photothermal microscopy**”, **Optics Within Life Sciences (OWLS-2012)**, Genoa, 4-6, July 2012.
- ❖ M. M. Bijeesh, **S. Arunkarthick**, Arvind Krishnan, Nishith Rastogi, Geetha K. Varier, Meenal Kowshik and P. Nandakumar. “**Construction of Simple Confocal Microscope**” **DAE-BRNS National Laser Symposium, RRCAT, Indore**, December 1-4, 2010.

WORKSHOPS / SYMPOSIUM PARTICIPATED

- ❖ **4th Bangalore Microscopy Course**, an International course on Optical Microscopy organized at National Centre for Biological Sciences (NCBS), TIFR, Bangalore – 560 065 during September 23-30, 2012.
- ❖ **SERC School on “Introduction to Systems and Synthetic Biology for Scientists and Engineers”** conducted by **IIT Bombay** during April 30 – May 3, 2012.

- ❖ **IWBMST- 2011**, an “**International workshop on Biomedical sciences and Technologies**” organized by **Anna University**, Chennai during March 2-4, 2011.
- ❖ **DAE-BRNS National Laser Symposium (NLS-19)**, organized at Raja Ramanna Centre for Advanced Technology (**RRCAT**), Indore – 452 013 during December 1-4, 2010.
- ❖ **Biophotonics**, a national level short course conducted by Indian Laser Association at Raja Ramanna Centre for Advanced Technology, Indore on November 29-30, 2010.
- ❖ **Imaging at Nanoscale**, an International Workshop organized by **IIT Bombay** at the time of ICONSAT’2010, on 17th February 2010.

AWARDS AND RECOGNITIONS

- ❖ Received a **Scholarship of 800 Euro** and registration fee waiver from the conference organizers to participate in **18th International Microscopy congress (IMC-2014)** held in **Prague, Czech Republic** during 7-12 September 2014.
- ❖ Awarded **Senior Research Fellowship (SRF)** from Council of Scientific and Industrial research (CSIR-Research Grants), Government of India.
- ❖ **Travel Grant Award** from **Department of Biotechnology (DBT-CTEP)**, Government of India for attending International Conference - **Focus on Microscopy - 2013** in **Maastricht, The Netherlands**.
- ❖ Received a **Best Poster Award** for the poster titled “**Construction of simple Confocal Microscope**” presented during the DAE-BRNS National Laser Symposium (NLS-19) held at RRCAT, Indore during December 1-4, 2010.

FELLOWSHIPS

- ❖ Institute **Senior Research Fellowship** received from Birla Institute of Technology and Science (**BITS**) from August 2012 to March 2013 and August 2014 to till date.
- ❖ Recipient of **Senior Research Fellowship** from Council of Scientific and Industrial Research (**CSIR**) from April 2013 to July 2014.
- ❖ **Senior Research Fellowship** received from Department of Biotechnology (**DBT**) funded project from December 2011 to July 2012.
- ❖ **Junior Research Fellowship** received from Department of Biotechnology (**DBT**) funded project from November 2009 to November 2011.

BIODATA OF CANDIDATE

Arunkarthick was born in 03rd July 1986 in Surandai – a small town in Tirunelveli District in Tamil Nadu, India to Samudram and Valliammal and younger brother to Raja and Ramesh. He married Jeyajothi on May 27, 2011. He got his Bachelor's degree in Industrial Biotechnology from Kamaraj College of Engineering and Technology, Virudhunagar, India during 2003 – 2007 and his Master's degree in Biotechnology from Anna University of Technology Tiruchirappalli, India during 2007 – 2009. In November 2009, he came to Goa to work as Junior Research Fellow in DBT funded project “Photothermal imaging of nuclear transport” in Birla Institute of Technology and Science, Pilani – K K Birla Goa Campus. Then he started his graduate study in Birla Institute of Technology and Science, Pilani with the proposed thesis title “Design and Development of Confocal Microscopic Techniques and Studies on Passive Permeability of Nuclear Membranes”.

He received the best poster award during 19th National laser symposium in RRCAT, Indore. He was awarded Senior Research Fellowship from Council of Scientific and Industrial research, Government of India in April 2013. He received a travel grant award from Department of Biotechnology, Government of India, for presenting his work in an international conference Focus on Microscopy, FOM - 2013 in Maastricht, The Netherlands. He also received a scholarship of 800 Euro and registration fee waiver from the conference organizers to participate in 18th International Microscopy congress, IMC – 2014 held in Prague, Czech Republic.

BIODATA OF SUPERVISOR

Prof. P. Nandakumar is currently working as an Associate Professor at the department of Physics, BITS Pilani, K. K. Birla Goa campus. He received his M.Tech. in Opto-Electronics and Laser Technology from Cochin University of Science and Technology, Cochin, Kerala in 1992. He completed his PhD in Physics from Indian Institute of Technology Madras in the year 1999 in the area of ‘semiconductor quantum dots’ under the supervision of Prof. Y.V.G.S. Murthy and Prof. C. Vijayan. After his PhD he worked for one year as a CSIR research associate at Indian Institute of Science, Bangalore with Prof. P. K. Das. Here he developed the necessary techniques and studied the second order nonlinear optical properties of certain organic complexes. There after he worked at the Weizmann Institute of Science, Israel for two years with Prof. Yehiam Prior on ‘coherent control of chemical. Next two years he spent at the University of Stuttgart, Germany with Dr. Andreas Volkmer on ‘Coherent Raman Microspectroscopy’. Here he, along with Dr. Volkmer and Dr. Kovalev developed a Raman scattering Microscope based on stimulated Raman loss detection, for noninvasive point-by-point vibrational mapping of chemical and biological samples with high sensitivity and without the requirement for labeling of the sample. He joined the department of Physics at BITS Pilani, K. K. Birla Goa campus as a faculty member in the year 2005. His current research interests include nonlinear and quantum optics, Biomolecular transport through nuclear membranes and optical microscopy and application in Biophysics.

BIODATA OF CO-SUPERVISOR

Prof. Meenal Kowshik received her M.Sc. in Microbiology from Goa University in 1997. She worked on the biological synthesis of metallic and metal sulfide nanoparticles using yeasts at Agarkar Research Institute, and obtained her Ph.D. degree from Pune University (1999 – 2003). Subsequently, she joined Birla Institute of Technology and Science, Pilani – K K Birla Goa Campus, and is currently working as Associate Professor in the Department of Biological Sciences. Her research interests include studies on biofunctionalization of silver based nanocomposites for antimicrobial applications; synthesis of biocompatible nanomaterials for tissue engineering; application of nanomaterials in molecular biology research; interactions of nanomaterials and microorganisms with respect to nanomaterial synthesis as well as toxicity, with special emphasis on halophilic archaeobacteria. She has received research grants from Department of Science and technology for two projects and from the Ministry of Earth Sciences. She has been a co–investigator on four other projects sanctioned by the agencies; Department of Biotechnology, DRDO and UGC. She has published 29 research papers in International and National journals of repute; has 3 patents to her credit and has delivered several invited talks at International and National conferences.

GLOSSARY

A

A549

A549 cells are adenocarcinomic human alveolar basal epithelial cells.

Argon

An inert gas that is used to generate a laser with wavelengths useful for fluorescence microscopy. Its most useful laser "lines" are at 488 and 457 nm.

B

Band Pass Filter

An optical filter which limits light transmission across a discrete range of wavelengths. For instance, a filter used for green dyes, a 515/30 band pass filter, means that it transmits a band of green light across the range of 500 – 530 nm.

C

Confocal

Confocal microscopy is an optical imaging technique for increasing optical resolution and contrast of a micrograph by means of adding a spatial pinhole placed at the confocal plane of the lens to eliminate out-of-focus light

D

Depth of Field

The range of distance within which all objects are in focus. This is described by the function:

$$Z = 2 \lambda \eta / NA^2$$

where: Z – optical thickness (mm), λ – wavelength (mm), η – refractive index of medium and

NA – numerical aperture. Note that this value is dependent on the NA of an objective, not the magnification.

Dichroic Mirror

A mirror that simultaneously reflects specific light wavelengths while transmitting other wavelengths. Thus the "RGB" dichroic illustrated below reflects the 488, 543 and 633 nm lines of the blue argon, green HeNe and red HeNe lasers, respectively, while transmitting the longer light from green, red and far-red dyes. The spectral properties of several dichroic mirrors are illustrated at Fluorescence Spectra. A long pass dichroic mirror is highly reflective below the cutoff wavelength and highly transmissive above it, while a short pass dichroic mirror is highly transmissive below the cutoff wavelength and highly reflective above it.

Digitonin

Digitonin is a kind of detergents used to permeabilize all cellular membranes; digitonin can permeabilize preferentially the plasma membrane of mammalian culture cells under conditions that leave the nuclear envelope intact. Digitonin is a glycoside used as a detergent; it effectively water-solubilizes lipids in membranes.

DNA

DNA is the short form of deoxyribonucleic acid, a self-replicating material which is present in nearly all living organisms as the main constituent of chromosomes. It is the carrier of genetic information.

E

Emission Filter

An optical filter in the emission light path that limits the range of light frequency that reaches the detector. These can be band pass or long pass filters.

Epifluorescence

The simultaneous process of excitation of a fluorescent specimen and subsequent observation of it using the same view point. "Epi" refers to viewing the same "surface" that is illuminated by the light source. This is to distinguish this type of microscopy from transmitted light microscopy, in which the light is transmitted through the specimen, and viewed from the side opposite the illumination source.

Excitation Filter

An optical filter in the excitation light path that limits the range of light frequency that reaches the specimen.

F

Fiber Optic

Fiber optic is a flexible cable which transmits light. Optical fibers can be used as a pin hole in confocal microscopic set up.

Fluorescence

The property of a molecule that causes it to absorb light energy at one wavelength and emit light at a longer wavelength.

Fluorochrome

Any molecule that is fluorescent. These are the molecules that act as tags to antibodies or gene constructs.

H

HeLa

HeLa cell line is a cell type in an immortal cell line used in scientific research. It is the oldest and most commonly used human cell line. One of the first things a biomedical researcher learns is that it's very hard to grow most human cells in the lab for an extended period. In fact, once

removed from the human body, most cells will either die immediately or reproduce only a limited number of times. That's why it was so significant in 1951 that this barrier was overcome for the first time, using cancer cells taken from a 31 year old African American woman named 'Henrietta Lacks'.

HeNe

A laser using a mix of Helium and Neon to produce light at wavelengths useful for fluorescence microscopy. Useful laser lines include 543 nm (green light for red fluorescence) and 633 nm (red light for far red fluorescence).

I

Increment

The distance the focus changes when moving through the steps of collecting a series of images.

In vitro

In vitro is the process performed or taking place in a test tube, culture dish, or elsewhere outside a living organism.

L

Laser

A laser is a device that emits light through a process of optical amplification based on the stimulated emission of electromagnetic radiation. The term "laser" originated as an acronym for Light Amplification by Stimulated Emission of Radiation

Lens

An optical device that focuses light. Microscope objectives and oculars are types of compound lenses.

Long Pass Filter

An optical filter which limits light transmission across a wide range of wavelengths. For instance, the filter used for GFP, a 510 long pass filter, means that it transmits green light 510 nm and longer.

M

Microscope

Microscope is an optical instrument used for viewing very small objects, such as mineral samples or animal or plant cells, typically magnified several hundred times.

Montage

The recombination of optical slices, usually as a maximum projection, into a single image.

Movie Stacks

The recombination of an image stack, incorporating the distance between optical slices, to reconstruct a 3-dimensional image of the specimen.

N

Neutral Density Filter

Optical filters which block a specific level of light regardless of wavelength. They are usually identified by the percent light they transmit. Thus a 10% ND filter transmits 10% of incident light and blocks 90%.

Noise Reduction

Any of several computational methods to remove random, artifact light from an image. The source of this artifact is often not light at all, but background electronic signals generated by the electrical components in the system, such as the PMT's, computer and imaging board.

O

Objective

The lens that first collects light from the specimen and produces the initial magnification.

Ocular

The eyepieces of the microscope.

Optical Slice

Optical slice is a plane in a translucent object (as a slip of tissue or a cell) brought into view by adjustment of the focus of a microscope.

P

PMT

Photo Multiplier Tube. The light detector in the confocal system. PMTs are used to record signals from fluorescence or any other light intensity.

Photodiode

Photodiode is a semiconductor diode which, when exposed to light, generates a potential difference or changes its electrical resistance.

Pinhole

The device that makes a confocal microscope "confocal". A tiny aperture that is placed in a specific focal plane of both the excitation and emission light path. The pinhole excludes out of focus light and allows only in-focus light to pass. This is why confocal images have such high contrast and so little background light or "haze".

Protein

Protein is any of a class of nitrogenous organic compounds which have large molecules composed of one or more long chains of amino acids and are an essential part of all living organisms, especially as structural components of body tissues such as muscle, hair, etc., and as enzymes and antibodies.

R

Reticulocyte Lysate

A reticulocyte is an immature red blood cell. Lysate is a solution that is formed when a cell's membrane is ruptured *in vitro*. So once a reticulocyte is ruptured what is in the environ as a result.

S

Scan Head

The box mounted on top of the microscope. This is the device that contains the pinhole, filters, dichroic mirrors and scanning mirrors that control how the laser scans the image and which detectors are used.

W

Wavelength

A measurement of the color of visible (and invisible) light energy. The range goes from ultraviolet (< 390 nm) through blue (390 – 490 nm), to green (490 – 545 nm), red (545 – 640 nm) and infrared (far-red, > 640 nm).

Working Distance

The distance between the surface of an objective and the plane of focus. In practical terms, it means how far the objective can be focused into the specimen before it hits the surface. High magnification objectives have very small working distances, for instance, 230 μm . Thus if the

specimen is covered by a coverslip that is 170 μm thick, there are only 50 μm under the coverslip through which the objective can focus. Anything deeper can't be placed in focus.

Z

Z-focus

Z-focus is important in optical microscopes to acquire optical sections in different focal planes. When observing a sample directly the limitations of the shallow depth of field are easy to circumvent by focusing up and down through the sample; to effectively present microscopy data of a complex 3D structure in 2D focus stacking is a very useful technique.